Direct Measurement of Fault Rupture using Seismic Dense Arrays: Method and Application to the Alpine Fault, New Zealand and SMART-1, Taiwan Data

---

A thesis

submitted in partial fulfillment

of the requirements for the Degree

of

Doctor of Philosophy in Civil Engineering

by

Caroline Francois-Holden

Department of Civil Engineering

University of Canterbury

Christchurch, New Zealand

September 2004

Abstract

A dense network of strong motion seismometers is being developed for the central South Island of New Zealand in order to investigate the complexities of the upper crustal rupture process and propagation of major seismogenic sources such as the Alpine Fault and strands of the Marlborough Fault System defining the South Island sector of the Australia-Pacific plate boundary zone. Dense array analysis allows one to measure directly fault rupture parameters such as the rupture direction, velocity, and fault rupture area. This study develops and applies dense array analysis to determine an optimal array for the Alpine Fault region.

The dense array analysis is based on the frequency-analysis MUSIC method (Multiple Signal Characterization) developed by Goldstein and Archuleta (1991a&b). MUSIC was chosen for its ability to resolve seismic signals with low signal-to-noise ratios. Careful programming, thorough data pre-processing and an innovative optimal time window determination were essential in obtaining reliable results.

The proposed network is designed as a dense array comprising approximately 12 accelerographs utilising the University of Canterbury CUSP instrument. It will be deployed immediately to the East of the East-dipping Alpine Fault in the central West Coast region of the South Island, with coverage extending across to the Alpine-Hope Fault junction. The search for an optimal network for the region is dependant not only on finding an optimal array configuration but also and more significantly on optimal site locations, which because of the mountainous terrain provides a severe limitation.

In order to assess the efficiency of dense array analysis, synthetic data were generated for known rupture scenarios. The synthetic strong-motion records were computed using an empirical Green's function synthetic seismogram program EMPSYN (Hutchings, 1987). Comparison of computed rupture parameters with synthetic known inputs has proven that the technique is efficient in reproducing fault rupture scenarios. The analysis provides rupture velocities and directions consistent with input values. These results are an important outcome to validate dense array analysis performed on real data sets. However, dense array analysis could reveal no sign of an asperity in the synthetic scenario.

The method is applied to a real dataset recorded at the dense SMART-1 array in Taiwan. Important rupture parameters such as the direction of propagation, velocity and rupture area were successfully measured. In addition, an interesting feature of the real rupture is also identified. The fault rupture initiates at a super-shear velocity and eventually slows to a "cruising" velocity closer to the shear-wave velocities. This result supports the emerging theory that a fault rupture velocity is not constant.

Acknowledgements

Dr John Berrill, my supervisor, initiated this project 4 years ago. I thank him dearly for his passion and enthusiasm, as well as for supporting me and always believing in me throughout the years. Thank you John for giving me the liberty to direct my research, the opportunities to acquire broad knowledge in Earth Sciences, to visit various laboratories and attend many conferences in New Zealand and overseas. Thank you also for encouraging me to discover and value your beautiful country that is New Zealand. Warm thanks to your lovely wife Jacqueline who always took motherly care of me.

I thank very much also Dr Jarg Pettinga for being always available for discussions and for his encouragement and support. I would like to thank Dr John Taber for his kindness and from whom I learnt a lot on setting up instruments in the field.

Grateful acknowledgement is due to the University of Canterbury and the New Zealand Earthquake commission (EQC) for having awarded me scholarships throughout my Ph.D studies. I also thank the Royal Society of New Zealand-Canterbury Branch for offering me a grant to attend the 2003 EGS-AGU-EUG Joint Assembly, and again the EQC for financially supporting me to attend the workshop in Taiwan on "Seismic Hazard Assessment in the Taipei Basin".

Sincere thanks are due also to Dr Hugh Cowan from GEONET for his interest in the project and for giving me the privilege to attend a unique conference in Taiwan. I also thank the Geosciences researchers from the New Zealand Institute of Geological and Nuclear Sciences (IGNS) and especially Jim Cousin for their help and interest in my work.

I am grateful to the Lawrence Livermore Laboratories (CA, USA) for hosting me on several occasions. I also thank Dr Hutchings for allowing me to use EMPSYN.

I am grateful to the academics and staff of the Civil Engineering Department of the University of Canterbury for their warm welcome, help and availability. I especially thank Louise Barton for helping me kindly with administrative matters, Peter Coursey for his kindness and enthusiasm in the project, Brandon Hutchinson for solving computer troubles, and Melody

Callahan for helping me greatly with poster presentations and also for her infectious enthusiasm.

I thank very much all the friends I have met during these years spent in New Zealand and San Francisco. I am especially grateful to my office mate and dear friend Katherine for her complicity and enthusiasm, for all those laughs and for bringing plants and dinosaurs into my life. Big thanks to my office mate David Plew for always being there to listen and help, and to the ABS team, Adam, Pierre and Katja for their friendship, coffees and haikus. Special thanks also my to my office mates and friends from the Livermore Labs Laura and Rengin for sharing biscuits and for fun bike rides and lunches around the labs.

I dearly thank my flatmates and friends, Dirk, Melanie and Cedric for two very extraordinary years spent together on Wilfrid Street. I thank very much also Jean for his comradeship throughout these years and Guillaume for never attempting to teach me climbing and for the great moments preparing and presenting Francofollies. Big thanks to Martine for trusting us to run her show and for her friendship. Special thanks to "ma copine de Musée" Dr Estelle Schissele for helping me with the MUSIC algorithm. Mucho Gracia to Mauricio, Beatriz, Tatiana and Luis. Grand merci to old friends whose friendship has strengthen with time and distance: Melisa, Sophie(s), Laure, Francois, Claire, Gael, Julie, Alex, Tatiana...

I thank my parents, brother and sister for their love and encouragement...

Thank you so much Tony for your love and friendship, for helping me, believing in me, and giving me confidence and enthusiasm...

Table of Contents

Appendix Files are found in the CD located on the back cover.

List of Figures

List of Tables

Introduction

The Alpine Fault is the major geological feature in New Zealand. It is a dextral transform fault separating the Pacific plate on the east from the Australian plate on the west, crossing the South Island from Northeast to Southwest (Figure I- 1). It has an average slip rate of 40 mm per year and is the longest fault in New Zealand with a length, on land, of 650 km (Yetton, 2000).

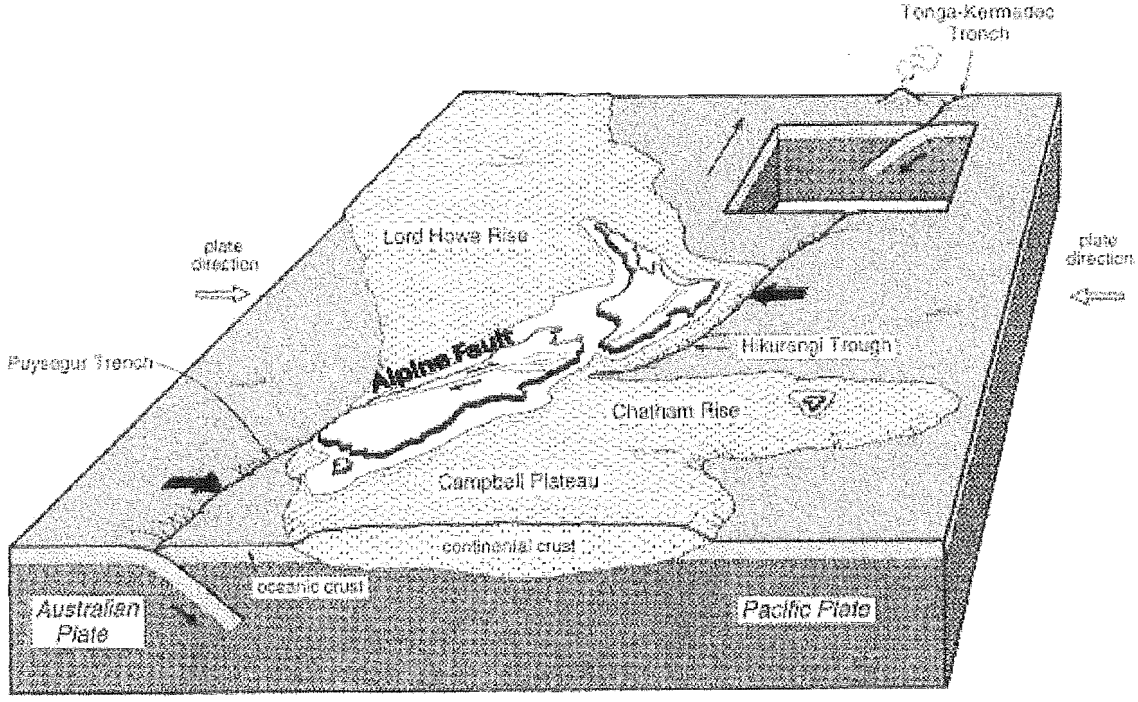

Figure I- 1: New Zealand regional tectonics (from Ansell and Taber, 1996). Heavy black arrows indicate subduction.

The Alpine Fault has been a source of strong earthquakes in the past. A recent field study led by Mark Yetton (2000) shows that the last rupture event occurred in 1717 AD; a minimum rupture length of 375 km extending as far North as the Haupiri River was estimated a moment magnitude of 8.05(+/-0.15). An earlier event, dated between 1480 and 1645, is noticeable throughout a region from the Hokitika River to the Ahaura River. This seems to be the most recent event North of the Haupiri River, with a rupture length of at least 200 km and a moment magnitude estimated to have been as great as 7.8(+-0.1).

The Alpine Fault is a potential source of major earthquakes in the near future. The return period of the fault is approximately 270 years, with no major event occurring over the last 285 years. Yetton applied various probabilistic methods to assess the time of the next major event on the Alpine Fault. Each method converged to give a likelihood of at least 50% of having a

major earthquake in the next 50 years. Using the slip rate and the elapsed time since the last event, Yetton estimates a moment magnitude between 7.5 and 8.4. Using the method of Coppersmith et al. (Wells et al., 1994), relating moment magnitudes to the rupture length of the fault, Yetton estimates the two previous events to be of magnitude 8.05 and 8.0. This allows us to assign the expected next event a moment magnitude of at least 8.0. The high level of probability of a major fault rupture in the region provides an ideal opportunity to study directly the process of fault rupture.

Common methods of studying the fault rupture processes involve the inversion of seismic waveforms to fit a proposed fault rupture model. These methods use various computations such as the genetic algorithm applied to strong motion and GPS observations (Zeng et al., 2001), waveform inversion of broadband teleseismic data (Olivieri et al., 1999), waveform inversion of multiple time window strong motion data (Sekiguchi et al., 2002), or broadband P wave inversion (Zobin et al., 2001). All these inversion processes make assumptions about the fault rupture model, and therefore depend on our current knowledge and assumptions of the fault rupture mechanism.

Using a dense array allows one to study the rupture directly without assuming any model. With a dense array, a frequency-wavenumber spectrum analysis can be computed, the spectra projected back onto their source on the fault plane thus giving an image of the source. With a direct image of the rupture process, one can estimate basic source parameters such as rupture velocity, direction of rupture, and possibly the position and extent of asperities. Because dense array analysis does not make any assumptions about the rupture mechanism, it is a powerful tool in understanding the physics of the source.

The method used in this study to carry out dense array analysis applies the mathematical algorithm MUSIC (Multiple Signal Characterization Method, Schmidt 1981, 1986). MUSIC was chosen for its ability to resolve seismic signals with low signal-to-noise ratios. In seismology, earthquake sources are not repetitive and signals are recorded at a limited number of stations. Previous studies have shown the advantages of using MUSIC for seismic signals over other methods: Goldstein (1988) strong motion array study, and Schissele (2002) who applied MUSIC to a broadband seismic antenna. MUSIC performs a frequency slowness analysis over a collection of seismograms. It uses the covariance matrix of the signals to extract information about the rays that propagate through the array. MUSIC looks for the true signal by searching for signals that have a minimum projection in the noise subspace. Results are presented in the form of a 2D slowness spectrum. Careful programming of the algorithm, thorough preparation of the data and accurate determination of time windows are the keys in

obtaining reliable results. An innovative way to determine optimal time windows containing only one source is introduced in this study. The MUSIC algorithm as well as the other complementary processes was reprogrammed from scratch using Matlab.

In order to assess the efficiency of dense array analysis, synthetic data were generated for two rupture scenarios with and without an asperity. The synthetic strong-motion records were computed using an empirical Green's function synthetic seismogram program EMPSYN (Hutchings, 1987). EMPSYN allows one to create synthetic strong motion earthquakes with complex geology, as well as, allows the user to choose from a variety of rupture scenarios. Dense array analyses of the vertical components for the two proposed rupture models are presented. They are compared to the original rupture models in order to discuss and validate the method.

Finally, dense array analysis is applied to a real dataset recorded at the dense SMART-1 array in Taiwan. The studied event is Event 5, a magnitude 5.9 earthquake that occurred in 1981. Event 5 is reprocessed applying dense array analysis to the three components of the recordings. Important rupture parameters such as the direction of propagation, velocity and rupture area are directly measured. This analysis of a real dataset provides interesting observations in regards to the fault rupture mechanisms.

CHAPTER 1 design of a dense array for the Alpine Fault

A Dense array analysis

1 Introduction and methodology

Dense array analysis when applied to strong motion earthquake signals allows the evolution of a fault rupture to be imaged directly. The method used in this study to carry out dense array analysis applies the mathematical algorithm MUSIC (Multiple Signal Characterization Method, Schmidt 1981, 1986). MUSIC was chosen for its ability to resolve seismic signals with low signal-to-noise ratios. In seismology, earthquake sources are not repetitive and signals are recorded at a limited number of stations. Previous studies have shown the advantages of using MUSIC for seismic signals over other methods: Goldstein (1988) strong motion array study, and Schissele (2002) who applied MUSIC to a broadband seismic antenna.

Dense array analysis requires successive processing steps. Firstly, the seismograms are filtered and aligned. Successive optimal time windows of analysis are then defined along the seismograms. For every time window, the extracted data are processed applying the MUSIC algorithm. Computations are conducted in the frequency-slowness domain, the output from MUSIC being a frequency-slowness spectrum. Finally, this spectrum is projected onto the fault plane to locate the source of the seismic signal. The methodology is summarized in Figure 1A- 8. The following sections describe the equations behind the MUSIC algorithm, the sub-processes applied to improve the performance of MUSIC, and the accuracy and resolution of the method.

2 The MUSIC algorithm

MUSIC performs a frequency slowness analysis over a collection of seismograms. It uses the covariance matrix of the signals to extract the information about the rays that propagate through the array. MUSIC looks for the true signal by searching for signals that have a minimum projection in the noise subspace. Results are presented in the form of a 2D slowness spectrum. Programming of MUSIC as well as the other complementary processes was completed using Matlab.

To apply the MUSIC algorithm to seismic data, two assumptions have to be made. The first being that the signals recorded at the array are plane waves. The plane wave assumption is valid if $\frac{L^2}{R_o} \leq \lambda$ with R_o being the hypocentral distance of the source, L the array aperture and λ the wavelength of interest. The second constraint requires that only a finite number of signals impinge on the array for each time window. The following mathematical expressions describe both the seismic source signals and the MUSIC algorithm equations.

2.1. Mathematical expressions

The development below follows the general analysis of Schmidt (1981, 1986) and Goldstein (1988). The following equations demonstrate how to extract the signal direction vectors of the seismic sources from the covariance matrix. For a dense array of N instruments recording q plane waves of angular frequencies ω, the signal received at station $\vec{x_i}$ is expressed as

$$\psi(\vec{x_i},t) = \sum_{m=1}^{q} A_m e^{i(\vec{k}_m \cdot \vec{x_i} - \omega t + \phi_m(t))} + \eta(\vec{x_i},t) \qquad \textbf{Eq. 1A- 1}$$

where $\eta(\vec{x_i},t)$ is the noise, $\vec{k}_m$ is the wavevector of the mth signal, and $\Phi_m(t)$ is the phase of the mth signal. If $\Phi_m(t)$ is a random function of time, the signal is said to be stationary. This is not the case for fault ruptures where signals are not independent. Nonetheless the following equations will assume that the signals are stationary. The case of non-stationary signals is discussed later.

The covariance matrix of a signal received at station i and j is:

$$R_{ij} = \left\langle \psi(\vec{x_i},t)\psi^H(\vec{x_j},t) \right\rangle_t \qquad \textbf{Eq. 1A- 2}$$

where $\langle\ \rangle_t$ represents the time average and H is the Hermitian conjugate (i.e. transpose conjugate).

For q stationary signals the elements of the covariance matrix can be expressed as:

$$R_{ij} = \sum_{m=1}^{q} |A_m|^2 e^{i\vec{k}_m \cdot (\vec{x_i} - \vec{x_j})} + \sigma^2 \delta_{ij} \qquad \textbf{Eq. 1A- 3}$$

where σ^2 is the noise intensity.

If the observed signal is expressed in its vectorial form:

$$\vec{\psi}(t) = [\psi(\vec{x}_1, t), \psi(\vec{x}_2, t), ..., \psi(\vec{x}_N, t)]^T \quad \textbf{Eq. 1A-4}$$

where T is the transpose operation, then the covariance matrix is written simply as:

$$R = \left\langle \vec{\psi}(t) \otimes \vec{\psi}^H(t) \right\rangle_t \quad \textbf{Eq. 1A-5}$$

where $\otimes$ indicates the outer product of two vectors.

The signal vector can also be written:

$$\vec{\psi}(t) = \sum_{m=1}^{q} A_m \vec{u}(\vec{k}_m) e^{-i(\omega t + \Phi_m(t))} \quad \textbf{Eq. 1A-6}$$

where the directional dependence is contained in the signal direction vectors:

$$\vec{u}(\vec{k}_m) = [e^{i\vec{k}_m \cdot \vec{x}_1}, ..., e^{i\vec{k}_m \cdot \vec{x}_N}]^T \quad \textbf{Eq. 1A-7}$$

The covariance matrix can then be written:

$$R = \sum_{m=1}^{q} |A_m|^2 \vec{u}(\vec{k}_m) \otimes \vec{u}^H(\vec{k}_m) + \sigma^2 I$$

or

$$R = USU^H + \sigma^2 I \quad \textbf{Eq. 1A-8}$$

where $U = \begin{pmatrix} \vec{u}(\vec{k}_1) & \vec{u}(\vec{k}_2) ... & \vec{u}(\vec{k}_q) \\ \downarrow & \downarrow & \downarrow \end{pmatrix}$, $S = \begin{pmatrix} |A_1^2| & 0 & \cdots & \cdots & 0 \\ 0 & \ddots & \vdots & \vdots & \vdots \\ \vdots & \vdots & |A_q^2| & \vdots & \vdots \\ \vdots & \vdots & \vdots & \ddots & \vdots \\ 0 & \cdots & \cdots & \cdots & 0 \end{pmatrix}$, and I the identity matrix.

Now that the mathematical expressions have been defined, the signal directions and intensities are determined applying the following equations.

If q less than N plane waves propagate across the N-station array, the covariance matrix of the signals has rank q and is non-negative definite. The minimum eigenvalue of R is σ^2 with multiplicity N-q. Thus the number of signals can be determined from the number of large eigenvalues, (i.e. greater than σ^2). Also, the N-q eigenvectors $\vec{e}_i$ of R associated with the minimum eigenvalues are orthogonal to the q spatial signal vectors $\vec{u}(\vec{k}_m)$:

$$\vec{e}_i \cdot \vec{u}(\vec{k}_j) = 0; \quad i = q+1, ..., N; \quad j = 1, ...q; \quad \textbf{Eq. 1A-9}$$

The covariance matrix can then be written:

$$R = E_s \Lambda_s E_s^{\ H} + E_n \Lambda_n E_n^{\ H} \qquad \textbf{Eq. 1A-10}$$

where

E_s is the N*q matrix whose columns are the q eigenvectors of R associated with the q large eigenvalues,

Λ_s is the q*q diagonal matrix whose diagonal elements are the large eigenvalues of R,

E_n is the N*N-q matrix whose columns are the eigenvectors of R associated with the N-q small eigenvalues,

Λ_n is the N-q*N-q diagonal matrix whose diagonal elements are the minimum eigenvalues of R, and

$E_s \Lambda_s E_s^{\ H}$ represents the signal contribution to the covariance, and $E_n \Lambda_n E_n^{\ H}$ represents the noise.

With the covariance matrix divided into a signal subspace and a noise subspace, MUSIC searches for the true signals in a unique way. MUSIC does not use the signal part of the covariance matrix but the noise subspace. As a consequence, a finer analysis is achieved than if the signal subspace had been used.

Let $\vec{a}(\vec{k})$ be the set of proposed vectors corresponding to the spatial dependence of plane wave vectors:

$$\vec{a}(\vec{k}) = \left[e^{i\vec{k}.\vec{x}_1}, e^{i\vec{k}.\vec{x}_2}, ..., e^{i\vec{k}.\vec{x}_N} \right] \qquad \textbf{Eq. 1A-11}$$

The real signal direction vectors will be the ones that have minimal projection in the noise subspace. Let $D(\vec{k})$ be the directional function:

$$D(\vec{k}) = \frac{1}{\left| \vec{a}(\vec{k}).E_n \right|^2} \qquad \textbf{Eq. 1A-12}$$

Peaks in the function $D(\vec{k})$ indicate that $\vec{a}(\vec{k})$ has minimal projection in the noise subspace E_n, and therefore represent the solutions for the signal direction vectors.

To find the q signal amplitudes, from equations (1A-8) and (1A-10), we obtain:

$$USU^H = E_s \Lambda_s E_s^H \qquad \textbf{Eq. 1A-13}$$

Isolating S from equation (13) gives:

$$\hat{S} = \left[A^H A \right]^{-1} A^H E_s \Lambda_s E_s^H A \left[A^H A \right]^{-1} \qquad \textbf{Eq. 1A-14}$$

$$\text{where } A = \begin{pmatrix} \vec{a}(\vec{k}_1) & \vec{a}(\vec{k}_2) & \dots & \vec{a}(\vec{k}_q) \\ \downarrow & \downarrow & \dots & \downarrow \end{pmatrix}$$

The diagonal elements of $\hat{S}$ are estimates of the signal intensities. Given that the primary purpose of this study was to find the direction of the signals, the signal intensities have not been analysed.

The output of the search for the signal direction vectors is a 2D slowness (wavenumber) spectrum. Although this gives accurate results for simple point source scenarios, the performance of the covariance matrix can be improved by applying some sub-processes prior to analysing the spectrum. These processes are described in the following paragraph.

2.2. Improving the performance of the covariance matrix

The covariance matrix contains more than the information about the signals of interest. It also records incoherent and non-stationary signals. These can be removed by averaging the matrix in the frequency domain as well as in the spatial domain.

Averaging in the frequency domain

Body waves are not dispersive. They have a constant slowness parameter, also called horizontal phase velocity. For the same body wave, the horizontal phase velocity is identical at all the stations. Therefore, averaging the terms of the covariance matrices over a range of frequencies will increase any coherent peak and attenuate the other signals. The advantage of this operation is that it does not depend on the shape of the array. This operation is also called "slowness stacking".

Averaging in the spatial domain

The covariance computations are applied assuming the signals are stationary (independent). This does not apply when considering sources such as a propagating fault rupture. Sub-array averaging is used to reduce the non-stationary contributions of the signals to the covariances.

When q non-stationary signals propagate through the array, the covariance matrix then becomes:

$$R_{ij} = \sum_{m=1}^{q} \left|A_m\right|^2 e^{i\vec{k}_m.(\vec{x}_i - \vec{x}_j)} + \sigma^2 \delta_{ij} + \left\langle \sum_{\substack{m=1 \\ m\neq n}}^{q} \sum_{n=1}^{q} A_m A_n e^{i(\vec{k}_m.\vec{x}_i - \vec{k}_n.\vec{x}_j)} \right\rangle_t \qquad \textbf{Eq. 1A- 15}$$

Comparison of the above equation to Eq. 1A- 3 shows that the last term of Eq. 1A- 15 represents the contribution of the non-stationary signals to the covariances. By averaging the

covariance matrix terms that correspond to linear and equidistant stations, the first term remains unchanged given that it only depends upon the station separation. On the other hand, the last term has different phases for different matrix terms. The different phases will eventually cancel out through the process of averaging the corresponding matrix terms. In order to apply practically sub-array averaging, the sub-arrays must be composed of linear and equi-spaced stations. For a matrix element R_{pq}, the condition is expressed as:

$$R_{ij,kl} = mean(R_{ij}, R_{kl}) \quad \text{if} \quad \vec{r}_{ij} = \vec{r}_{kl} \qquad \textbf{Eq. 1A- 16}$$

The previous sub-processes are used to optimise the performances of MUSIC. The following sub-processes are used in aligning the seismograms and searching for an optimal time window.

3 Seismogram alignment

Aligning the seismograms requires a shift of the recordings along the time axis in order to align them along a specific phase. The phases of interest are the first P wave arrivals, for the study of the vertical components, and the first S wave arrivals, for the study of the horizontal components. All recordings are aligned with respect to the central station.

The alignment process plays a major role in the array analysis as it corrects for localized site delays beneath each instrument, as well as allowing the time window to be shortened. This is especially important as shorter time windows give shaper results.

In this study, the alignment of the seismograms is done almost automatically by using the correlation of the signals. The correlation is computed for a two-second long window extracted from the unaligned seismogram and the central station seismogram. The peak value of the correlation vector represents the time-shift to apply to the signals. Results are all checked individually and corrected manually when proven unsatisfactory.

By aligning the seismograms, the computed slowness (wavenumber) spectra are shifted by a constant wavenumber vector. This wavenumber or slowness vector has to be removed from the slowness spectra. It is equal to the least square inversion of the measured time delays between the central station and the rest of the array. Figure 1A- 1 shows the geometry of a planar wave front propagating through two array receptors A and B. The apparent slowness is equal to the time the ray takes to travel from the central station A to station B divided by the distance D from the ray to station B when the ray is crossing the central station. The best slowness shift vector direction is selected amongst a range of 400 azimuth angles from 0 to pi

(Angle α on Figure 1A- 1). Aligning the seismograms is also called "beam forming" when it is performed on the first arrivals of the recordings. Therefore it also gives the epicentral direction of the first incoming signal, otherwise known as the azimuth of the source. This value can be compared with other analyses of the event in order to validate the results.

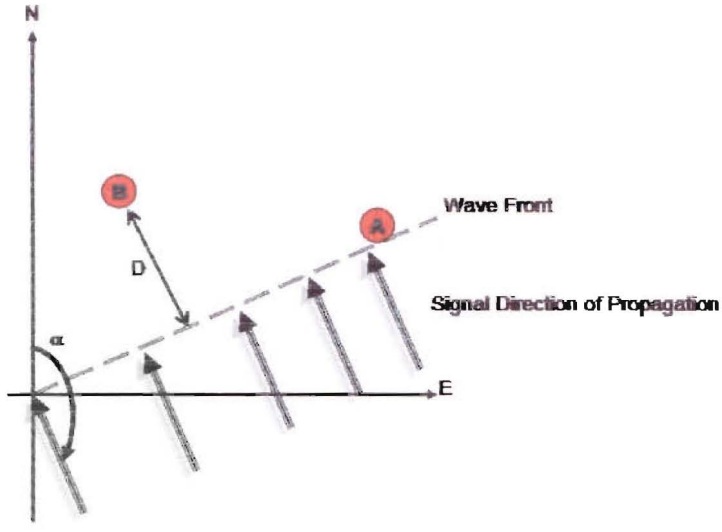

Figure 1A- 1: Geometry of a planar wave front propagating through stations A and B

4 Defining the time windows

Defining the correct time windows is essential in any array analysis. A time window is defined by its centred position along the seismogram as well as by its width. When using a large window, the probability of catching some coherent signal is high, but the resolution will be low. On the other hand, a shorter window will result in a better resolution but increase the probability that a coherent signal may not be found.

The importance of using the right time window is illustrated in the following example. Synthetics are generated using the Bouchon code (Bouchon, 1981) at a 17-station array. The configuration of the array is circular (Figure 1A- 2): two concentric circles of 8 stations each, with respective radii of 300 m and 1 km.

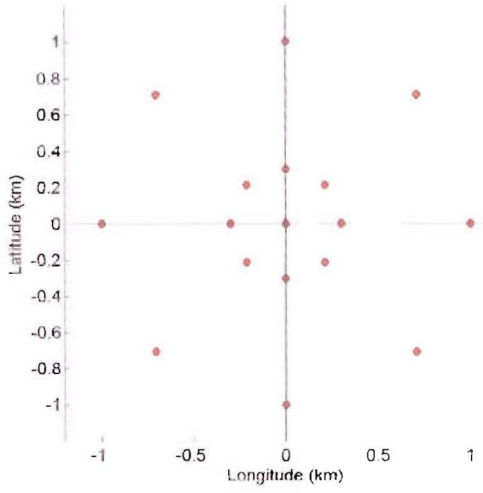

Figure 1A- 2: A 17-station array configuration

The simple geology model consists of a one layer 3-dimensional block with a P wave velocity of 8 km/s and S wave velocity of 5 km/s. The source ruptures along a small fault plane with the following parameters:

- 10 km deep, 3 km long and 1 km wide
- Zero degree strike, 90 degrees dip (vertical fault plane) and zero degree rake (orientation North-South).
- 0.8 meter of slip and a rise time of .5 second.

Figure 1A- 3 shows the displacement records for two stations at the array.

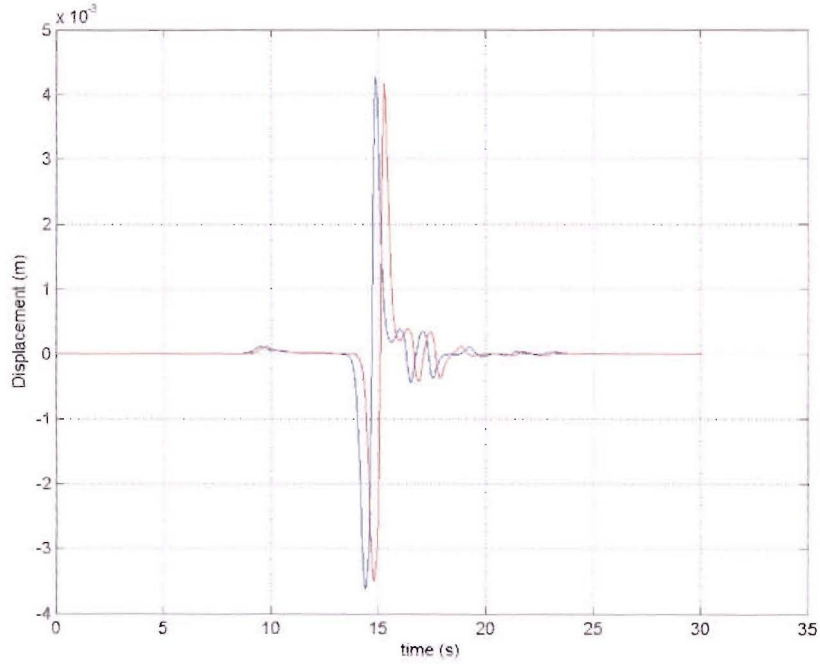

Figure 1A- 3: Synthetic displacement seismograms for a point source rupture

Dense array analysis is performed for two time windows both centred on 15.7 second. The first window is 6.6 second long and the second one 5.1. Results are presented in Figure 1A- 4.

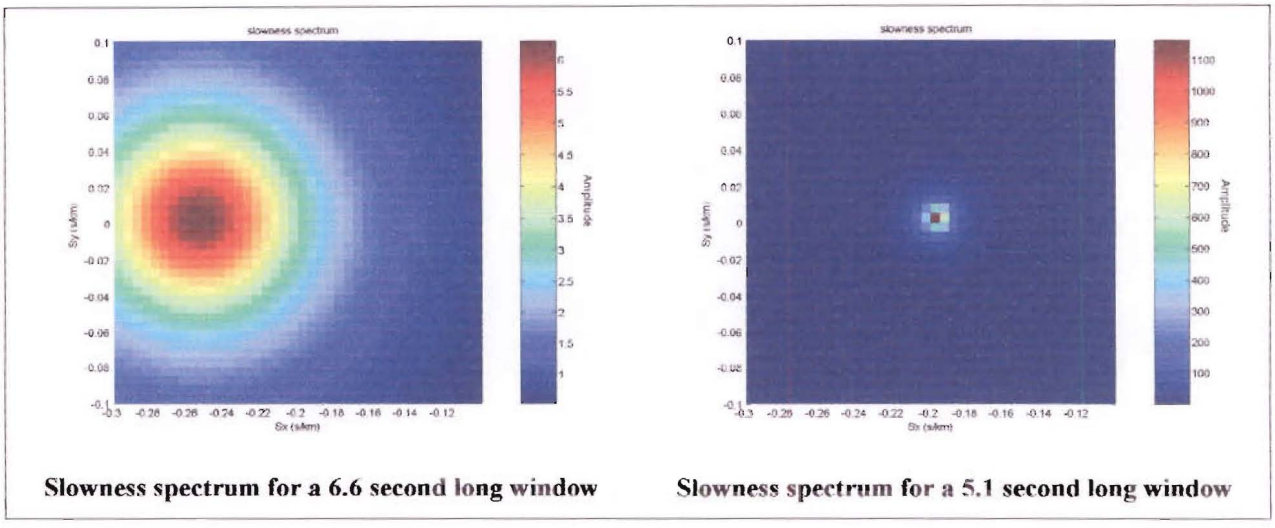

Slowness spectrum for a 6.6 second long window **Slowness spectrum for a 5.1 second long window**

Figure 1A- 4: Slowness spectra computed for two different size windows

Figure 1A- 4 clearly illustrates the importance of using the appropriate time window. For the longer time window of 6.6 seconds, the slowness peak is offset, broader and lower in intensity than the slowness peak for the shorter time window. The choice of the time window strongly influences not only the location of the slowness peak, but also its intensity.

Optimal time windows can be determined by confining similar packets of energy for each station seismogram through studying the frequency content of the seismograms. Commonly used techniques include the spectrogram and scalogram.

The spectrogram is the result of a Fourier transform performed on successive time windows of fixed width. The width of the Fourier analysis determines the results. Using a short time window allows one to detect a strong change in the composition of the signal, but limits the study of lower frequency signals. On the other hand, using a wider time window helps in detecting lower frequency signals, but decreases the temporal resolution. Figure 1A- 5 shows the spectrogram for a recording at the SMART-1 array central station for 3 to 11 seconds.

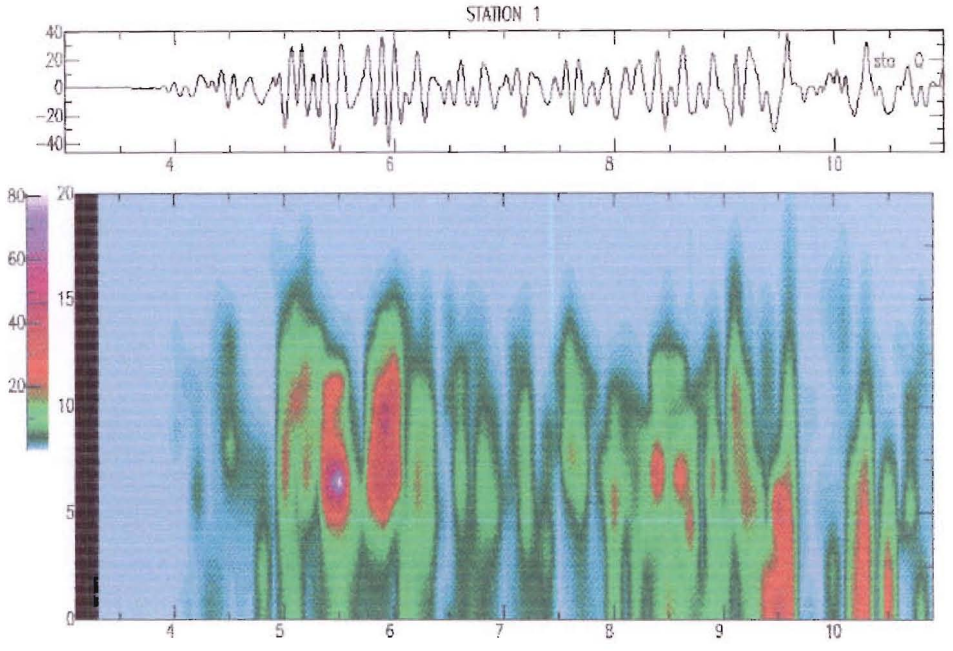

Figure 1A- 5: Spectrogram of the signal recorded at the SMART-1 central station for a .2 second long constant window analysis. Y axis represents the frequency in Hz.

The spectrogram from Figure 1A- 5 shows a good signal analysis from 5 to 10 Hertz. However, at lower frequencies, the resolution becomes increasingly poor. This is expected given the bandwidth chosen of Fourier analysis was relatively short (.2 second long). To better resolve the lower frequencies, a new spectrogram must be computed with a longer bandwidth of analysis.

Unlike the spectrogram, the scalogram is not influenced by the width of the computation window. The scalogram is a wavelet transform that is applied to the whole seismogram. The scalogram analyses the frequency content of the signal by fitting elementary wavelets of various central frequencies to the signal. Figure 1A- 6 shows the scalogram for the same signal as in Figure 1A- 5.

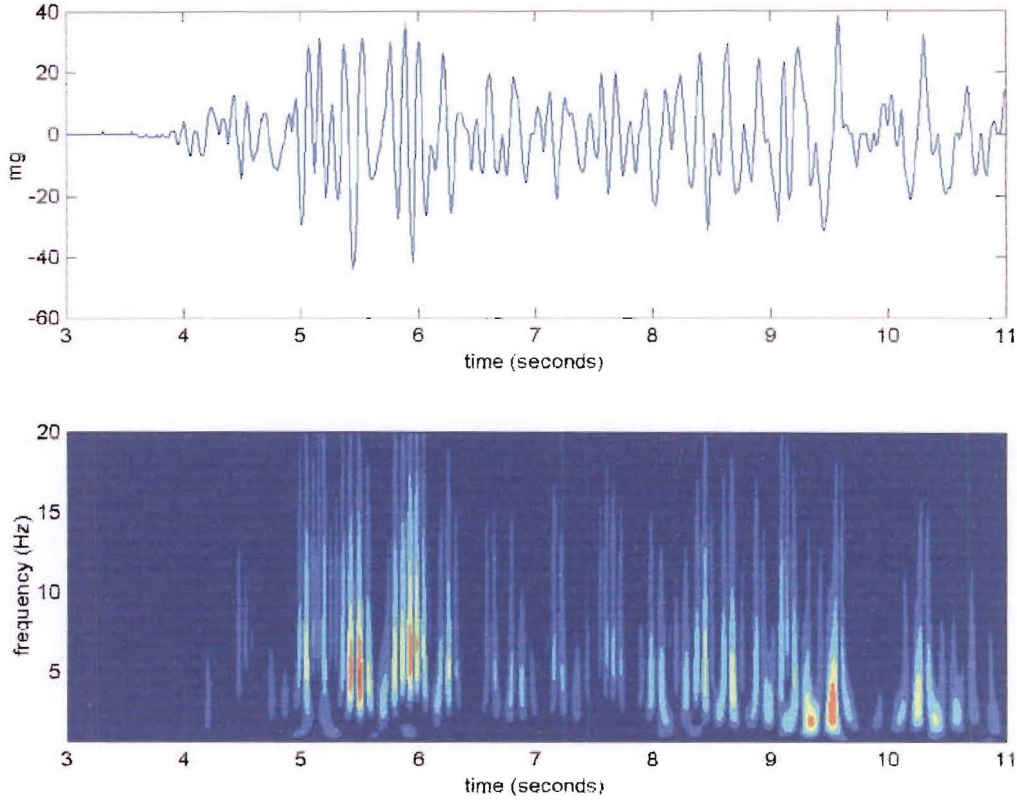

Figure 1A- 6: Scalogram of the signal recorded at the SMART-1 central station for 3 to 11 seconds.

Comparing Figure 1A- 5 to Figure 1A- 6 shows that the scalogram analysis is more efficient than the spectrogram analysis. The resolution of the scalogram time analysis is both finer and provides better results for frequencies below 5 Hertz. At 9.5 seconds the scalogram also shows packets of energy that could not be discerned on the spectrogram.

Using the scalogram or the spectrogram to look for the optimal time windows involves tracking similar packets of energy for each seismogram. For example, Figure 1A- 7 is showing the scalogram analysis for seismograms recorded at three stations 17, 21 and 26 at the SMART-1 array for an event called Event 5 (See chapter 3). The scalogram colour code is the opposite of the one used in Figure 1A- 6. An attempt is made to isolate similar phases looking at these three scalograms. Phases are grouped by comparable energy intensity, similar shapes, or both. The groups lead to confine nine windows labelled from 1 to 9 on Figure 1A- 7.

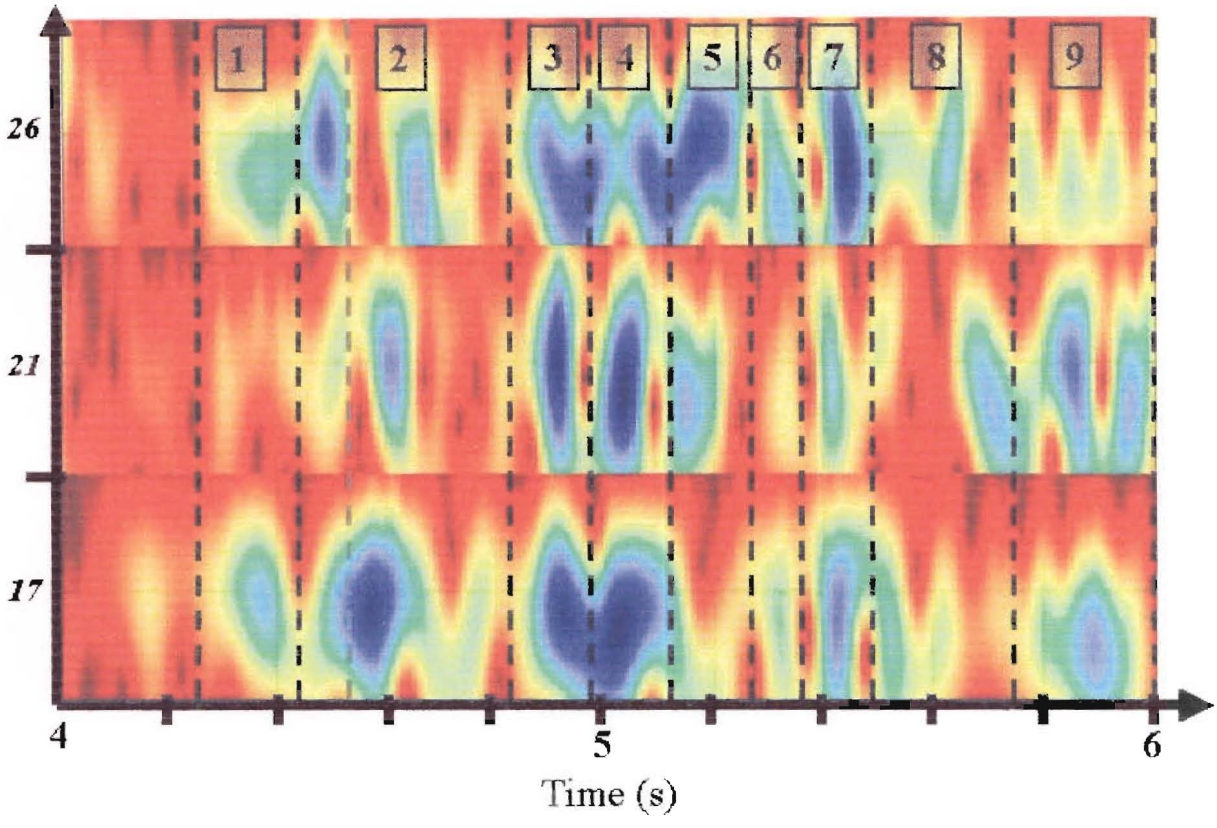

Figure 1A- 7: scalogram analysis of event 5 recorded at three SMART-1 stations

Although some windows such as window 3, 4 and 7 are promising, most of them seem not very efficient. This analysis based on just three scalograms shows how suggestive it is to visually try to separate time windows.

To conclude, neither the scalogram nor the spectrogram can be used efficiently for array analysis. Although both techniques are visually attractive and efficient for single station analysis, they require a significant amount of time to define common time windows for multiple station arrays. Therefore an alternative technique is used in this study.

The chosen method of time analysis is the "QEE" (Schissele, 2002), "Quantitée d'Energie Expliquée" (Quantity of explainable energy). The advantage of this method is that one can search for the optimal time window using all the recordings at once. The method is based on rebuilding the signals using parameters extracted from the MUSIC frequency wavenumber analysis. The energy of the computed output signal is compared to the energy of the real input signal. This quantity determines how close the computed signal is to the real one for various proposed time windows. The QEE method is described in the following equations.

Let $sig(t,\vec{r})$ be the recorded signal for a certain station position $\vec{r}$ at time t. Let $\hat{sig}(t,\vec{r})$ be the estimated signal. For a frequency ν_0, the estimated signal is written:

$$\hat{sig}(t,\vec{r}) = \sum_{i=1}^{q} A_i \sin(\vec{k}.\vec{r} - 2\pi\nu_0 t + \phi_i(t)) \qquad \textbf{Eq. 1A- 17}$$

where A_i and ϕ_i are the unknown amplitude and phase of the impinging signal.

The signal is developed:

$$\hat{sig}(t,\vec{r}) = \sum_{j=1}^{q} [A_j \sin(\vec{k}_j.\vec{r}_k - 2\pi\nu_0 t_i)\cos(\phi_j(t)) + A_j \cos(\vec{k}_j.\vec{r}_k - 2\pi\nu_0 t_i)\sin(\phi_j(t))] \qquad \textbf{Eq. 1A- 18}$$

The unknown parameters A and ϕ are determined by minimising the error function:

$$E = \sum_{i=1}^{N}\sum_{k=1}^{Ntrace} (sig(t_i,\vec{r}_k) - \hat{sig}(t_i,\vec{r}_k))^2 \qquad \textbf{Eq. 1A- 19}$$

where N is the number of time samples and N_{trace} is the number of stations or recordings.

Let T be the following matrix:

$$T_{1j} = A_j \cos(\phi_j) \text{ and } T_{2j} = A_j \sin(\phi_j) \qquad \textbf{Eq. 1A- 20}$$

Therefore to minimise the error function E, equation 1A-18 can be rewritten

$$[sig(t,\vec{r})] \approx [COSIN(\vec{r})][\hat{T}] \qquad \textbf{Eq. 1A- 21}$$

where

$[sig(t,\vec{r})] = [sig(t_1,\vec{r}_1) \quad sig(t_2,\vec{r}_1) \quad \ldots \quad \ldots \quad sig(t_N,\vec{r}_{Ntrace})]^T$ is the $(N * N_{trace},1)$ matrix with "N" being the number of time samples and "Ntrace" the number of instruments, and

$$[COSIN(\vec{r})] = \begin{bmatrix} w(\vec{r}_1).\sin(\vec{k}_1.\vec{r}_1 - 2\pi\nu_0 t_1) & \ldots & w(\vec{r}_{N_{trace}}).\sin(\vec{k}_1.\vec{r}_{N_{trace}} - 2\pi\nu_0 t_N) \\ w(\vec{r}_1).\cos(\vec{k}_1.\vec{r}_1 - 2\pi\nu_0 t_1) & \ldots & w(\vec{r}_{N_{trace}}).\cos(\vec{k}_1.\vec{r}_{N_{trace}} - 2\pi\nu_0 t_N) \\ \ldots & \ldots & \ldots \\ w(\vec{r}_1).\cos(\vec{k}_q.\vec{r}_1 - 2\pi\nu_0 t_1) & \ldots & w(\vec{r}_{N_{trace}}).\cos(\vec{k}_q.\vec{r}_{N_{trace}} - 2\pi\nu_0 t_N) \end{bmatrix}^T$$ is the

$(N * N_{trace}, 2q)$ matrix. COSIN represents the wavelets propagating through the array with a frequency ν_0. The function $w(\vec{r}_i)$ is a weight applied on the sines and cosines functions in order to take into account the true amplitude of the signal extracted within a finite time window. The function is the actual envelope of the real signal; it is therefore different for each station.

The unknown parameters are contained within the (2q*1) matrix $[\hat{T}] = [T_{11} \quad T_{21} \quad \ldots \quad T_{2q}]^T$.

By inverting the systems defined in Eq. 1A- 21, matrix T becomes:

$$\left[\hat{T}\right] = \left[COSIN^T COSIN\right]^{-1} COSIN^T \hat{sig} \qquad \textbf{Eq. 1A- 22}$$

Amplitudes and phases are computed using Eq. 1A- 21 again.

Schissele (2002) defines QEE ("Quantity of Explainable Energy") as the quantity of energy of the estimated signal over the quantity of energy of the real signal. For q signals propagating through the array, this is expressed as:

$$QEE(q_{phases}) = \frac{\sum_{i=1}^{N}\sum_{k=1}^{N_{stat}}\left(\hat{sig}(t_i,\vec{r}_k)\right)^2}{\sum_{i=1}^{N}\sum_{k=1}^{N_{stat}}\left(sig(t_i,\vec{r}_k)\right)^2} \qquad \textbf{Eq. 1A- 23}$$

In Eq. 1A- 23, all the elements of the time window are squared and summed before being compared. However this can lead to wrong interpretations. In some cases the real signal and the estimated signal might be different in amplitude and phase, but their respective sum terms may still be equal. In these cases the QEE term would show a high value although the real and recomposed signals are very different. Therefore, in this study it is proposed to modify Eq. 1A- 23. The proposed change is such that each term of the signal is compared prior to being summed. For q signals propagating through the array the new equation is thus:

$$QEE(q_{phases}) = \sum_{i=1}^{N}\sum_{k=1}^{Nstat}\frac{\left(\hat{sig}(t_i,\vec{r}_k)\right)^2}{\left(sig(t_i,\vec{r}_k)\right)^2} \qquad \textbf{Eq. 1A- 24}$$

Schissele (2002) applies the QEE method to moving time windows of constant width to estimate the number of signals impingeing onto the array for each window. As mentioned in paragraph I-A-2, this study assumes that only one signal is contained within each of the proposed time windows (q=1). The QEE method is then applied to determine the optimal window width for successive overlapping windows. For each central position of the time window on the recordings, the parameter QEE is estimated for various window widths. High values of QEE show the presence of a coherent signal. When plotting the parameter QEE as a function of the "window position" and the "window width", peaks in the 2D spectrum represent the optimal windows of analysis.

5 From slowness spectra to fault spectra

Results of the computations using MUSIC are in the form of a 2D slowness spectrum. The slowness spectrum is then projected back onto the fault plane. This projection is essential in visualizing the evolution of the rupture on the fault, computing the distances between rupture points and computing the actual rupture times. Conversion of slowness values into distances

values requires only the velocity model of the region and the location of the fault plane. There are two ways to project the slowness spectrum.

One method is to project directly the slowness vectors (Sx,Sy) from the slowness spectrum onto the fault plane using Snell's law. This ray-tracing method is fast and straightforward for individual point sources when dealing with simple velocity models and simple fault geometry. It is the method chosen in the application of dense array analysis to synthetic point sources (See chapter 1-B). Nonetheless, realistic velocity models and fault geometries are complex. Slowness projection in the cases of the Alpine fault simulation (refer to chapter 2) and the SMART-1 data analysis (refer to chapter 3) require a more efficient method. This second method consists of producing fault maps of slowness isocontours for a given velocity model and fault geometry. Firstly, the fault is divided into a grid. For every point P on the fault, the slowness components Sx_p and Sy_p corresponding to a specific array location are computed. Eventually two slowness fault maps are produced: one for the X component of slowness and one for its Y component. Finally, to find the fault location of the slowness peak Q of coordinates (Sx_q, Sy_q) one need only to find the intersection of the isolines $Sx=Sx_q$ and $Sy=Sy_q$. Slowness maps with high gradient contour lines are better to resolve source locations. Thus slowness maps are also useful in estimating the efficiency of an array location regarding a fault plane.

To compute slowness fault maps, the chosen program is the "TauP Toolkit" (Crotwell et al., 1999). To apply this software, which works in 2D, the fault defined by an x-y plane had to be "sliced" parallel to the Z axis and at regular intervals.

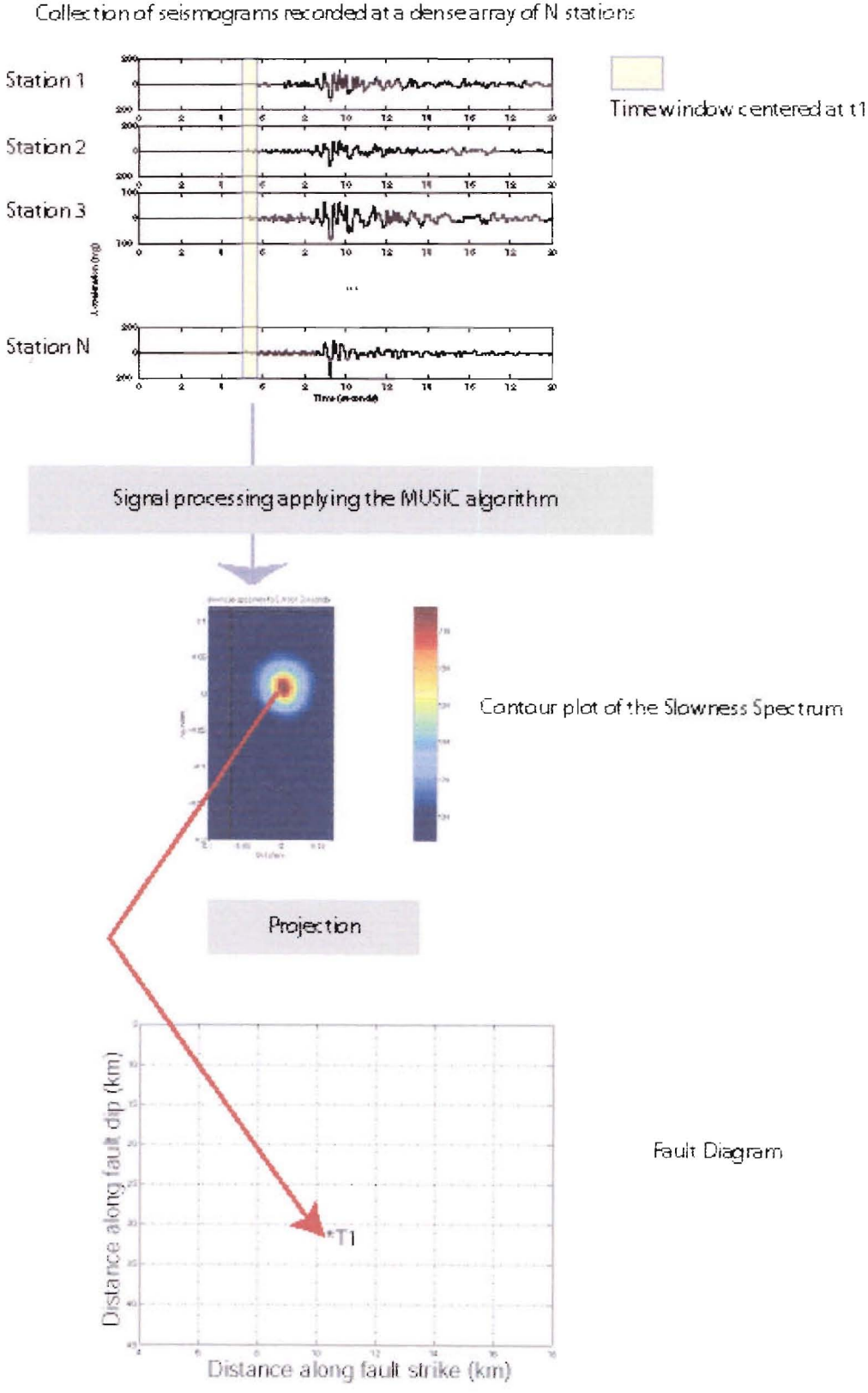

Figure 1A- 8 Dense array analysis methodology

6 Accuracy and resolution of the method

Performance of dense array analysis is firstly measured on how well the propagation parameters of a point source are estimated. This is called the slowness precision. In this study, the propagation parameters of a signal are the horizontal slowness (or apparent velocity), and the source azimuth. The performance is also assessed on the minimum slowness separation at which multiple sources can be resolved. This is called the slowness resolution. Although this study assumes that only one signal propagates through the array at a time, it is interesting to analyse the resolution power of the method.

Various parameters can lead to uncertainties in the results. These parameters are the signal intensities, the noise background, the number of signals propagating through the array, the array geometry and aperture, the number of stations, the timing accuracy and the slowness grid used in the computations. The following sections describe the influence of some parameters on slowness precision, and describes briefly the slowness resolution.

6.1. Precision of the slowness and azimuth of the sources

The precision of the slowness and azimuth of the sources has diverse definitions depending on which uncertainty parameter is considered.

Dependence of the slowness on array parameters

Following Goldstein (1988), the slowness precision of MUSIC is approximated by:

$$\sigma_S = \frac{1}{\sqrt{M}} \frac{\sqrt{1+NSNR}}{NSNR} \frac{1}{2\pi Lf} \qquad \textbf{Eq. 1A- 25}$$

where N is the number of sensors, M the number of samples, SNR is the signal to noise ratio, L the array aperture and f the frequency.

Considering the case of the SMART-1 array (refer to chapter 3), for M=100, L=4km, N=26, and SNR=1, the slowness precision is 8.10^{-4} sec/km. This value is lower than the constant grid spacing used in this analysis of a SMART-1 event which is 5.10^{-3} sec/km. Nonetheless this formula does not take into account the probable errors in timing or station spacing. It also does not take into account the limitation of the slowness grid used for the computations.

Dependence of the slowness on station spacing and timing accuracy

Goldstein (1988) then suggests considering the difference in phase between two stations.

$$\Delta\Phi = \omega\Delta t = \omega S\Delta x \qquad \textbf{Eq. 1A- 26}$$

where S is the horizontal slowness, Δt is the time difference for the same phase at two stations, and Δx is the station separation.

Considering δt and δS be the measurement errors of Δt and S. The mean value of the measurements recorded at N stations is:

$$\delta S = \frac{\delta t}{\sqrt{N}\Delta x} \qquad \textbf{Eq. 1A- 27}$$

In the case of the SMART-1 array, for δt =0.01 seconds, N=26 and Δx =1 km, the slowness precision is about 2.10^{-3} sec/km. This value is 2.5 times higher than if only the array parameter are taken into account. Nonetheless it is still a value smaller than the computation grid spacing (5.10^{-3} sec/km).

Dependence of the slowness on the computation grid

Schissele (2002) considers that the major uncertainty in the signal parameter estimation is due to the size of the computation grid Δs. The uncertainty in the slowness is expressed as $\frac{\Delta s}{s}$. In practice the size of the grid is limited by the computing time.

First, let us consider a regular slowness grid, Δs=constant. With a constant slowness grid step the error will be higher for low slowness parameter signals. For example, in the SMART-1 case study (refer to chapter 3), the range of the slowness grid in both directions is [-0.2 to 0.2] sec/km for a Δs=0.005. The number of samples is 80 samples for each dimension of the grid. For a slowness vector of 0.025 sec/km computed using this grid, the uncertainty is 20 %.

Schissele proposed an irregular geometry of the grid points. She suggested keeping the uncertainty constant throughout the grid by having the grid step such that $\frac{\Delta s}{s}$ is constant. The two different grid systems are illustrated in the figure below.

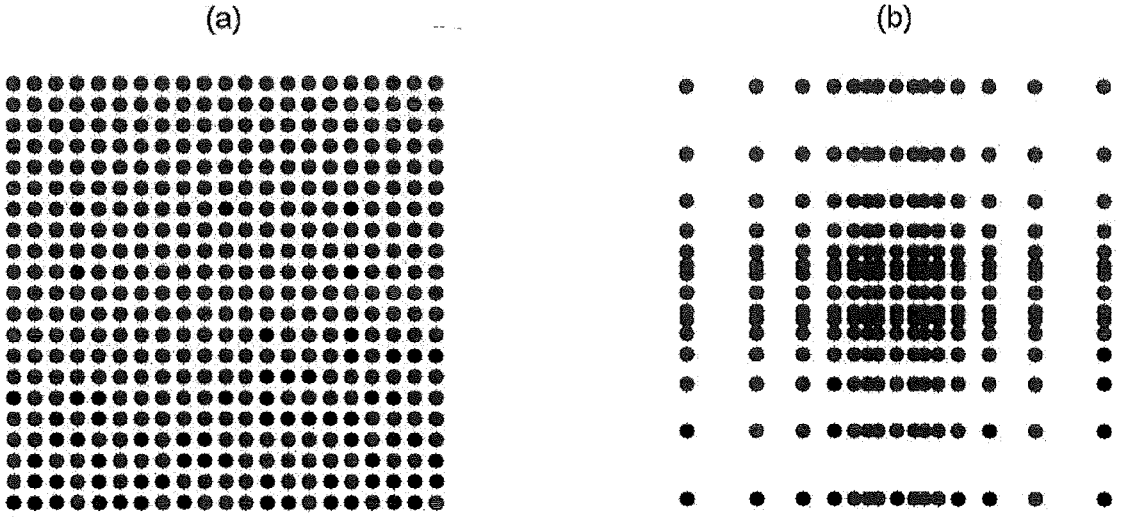

Figure 1A- 9 Comparison of two grid systems: (a) a regular grid and (b) an irregular grid (from Schissele, 2002)

For example, by using an irregular grid of $\frac{\Delta s}{s}$=0.03, the uncertainty is reduced to 3%. For a measured 0.025sec/km slowness point, the slowness grid step becomes 0.00075sec/km. Although the relative uncertainty increases with increasing slowness values, it remains nonetheless of the same order as with a regular grid (Schissele, 2002). This result is illustrated in Figure 1A- 10.

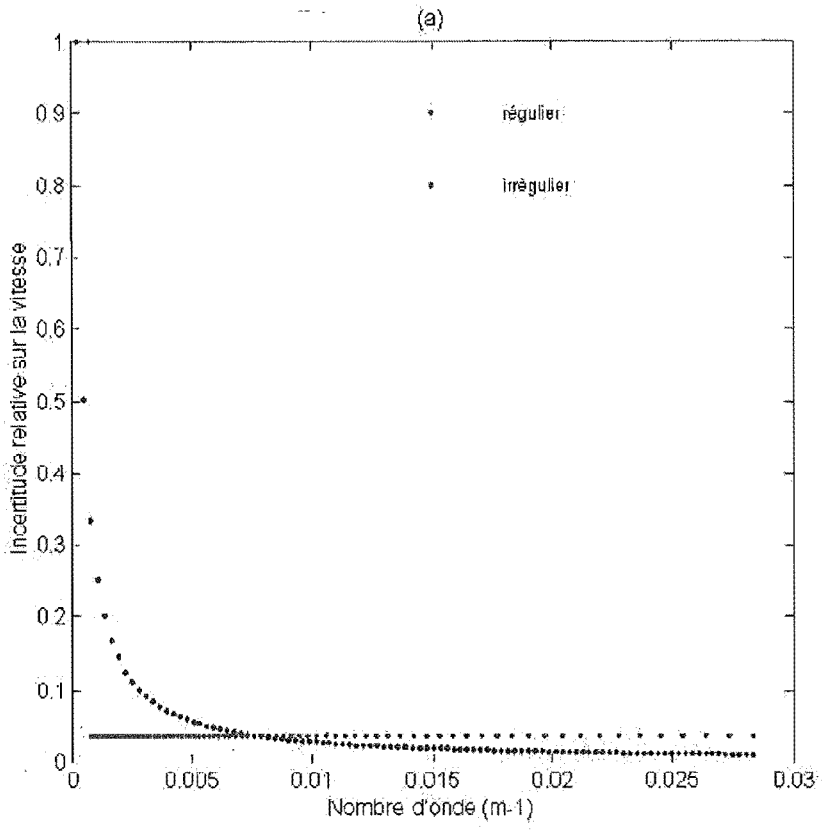

Figure 1A- 10 Relative uncertainty on the apparent velocity for two grid systems (from Schissele, 2002)

Dependence of the source azimuth on the computation grid

Following the equation from Schissele (2002) to estimate the uncertainties on the source azimuth:

$$\Delta\theta = \cos(\theta)\sin(\theta)\left(\frac{\Delta S_N}{S_N} + \frac{\Delta S_E}{S_E}\right) \qquad \textbf{Eq. 1A- 28}$$

where S_N and S_E are the North and East components of the slowness vector.

The uncertainty not only depends on the slowness values but also on the azimuth values. It is a maximum for a source azimuth of $\pi/4$ (mod $\pi/2$) and nul for angles of $\pi/2$ (mod $\pi/2$). Being also a function of the slowness value, the uncertainty depends on the choice of grid system. Here the irregular grid system also gives a better performance. Schissele computed that for a 5Hz wave propagating at 5km/sec, the azimuth uncertainty is 20 degrees using a regular grid, and 3 degrees for an irregular grid system.

6.2. Resolution of the frequency- slowness power spectra

The resolution is the ability to resolve the propagation parameters when more than one ray is propagating through the array. Although this study assumes that only one signal is propagating through the array at one time, it is interesting to assess the resolving power of the method.

Based on previous studies and experience, Goldstein (1988) estimated the resolution to be from half a slowness beamwidth under poor conditions (high SNR, few samples), up to one-sixth of a slowness beamwidth. For the 36-sensor SMART-1 array (refer to chapter 3), he estimated that the minimum slowness separation for a 1 Hz signal is 0.04 sec/km. Empirical results from Schissele (2002) using a linear modulation in frequency for 2 sources show that MUSIC performance is very good above 3 Hz. For two signals with frequencies higher than 3 Hz, MUSIC is able to separate them perfectly.

B Optimal array distance and configuration

Kinematic fault rupture imaging is equivalent to localizing seismic point sources in space and time. The best array to image a fault rupture is therefore one able best to resolve seismic point sources on a fault plane. This is the basis of the proposed methods used in determining the optimal array locations and configurations.

1 Optimal distance

When dealing with a single seismic source, the optimal distance of an array is one closest to the source: energy attenuation is lower, the geologic path is simpler, and geometric spreading is minimised. Nonetheless, it is different for a finite propagating fault rupture. One must consider all the ensemble of sources spread along the fault plane, as well as their time dependence and the directivity of the rupture and the orientation of the fault plane. By comparing a finite fault plane to a movie screen, the ideal location should be a compromise between being close enough to catch details but far enough away to be able to "see" the edges of the screen. In the following paragraphs tests on slowness grids and ray-tracing are performed on various array locations in order to determine the optimal array-fault distance. The optimal distance is determined through optimising both the slowness resolution and the resolution of the source location.

1.1. Optimal distance to optimize slowness resolution

The method proposed to determine the optimal array/fault distance is based on finding the configuration that gives the lowest uncertainty. The slowness uncertainty is expressed as $\frac{\Delta S}{S}$.

For various array/fault distances, the slowness vectors vary and so do the slowness uncertainties. Figure 1B- 1 shows the slowness uncertainties for various array-fault configurations. It is based on results obtained using a conservative velocity value of 8km/s, a regular grid spacing of 0.001s/km and a source depth of 10km. Results have been computed for arrays located 20 to 100 km away from the fault, and for point sources located 5 to 120 km along the fault plane. These values have been chosen to represent the case study developed in chapter 2.

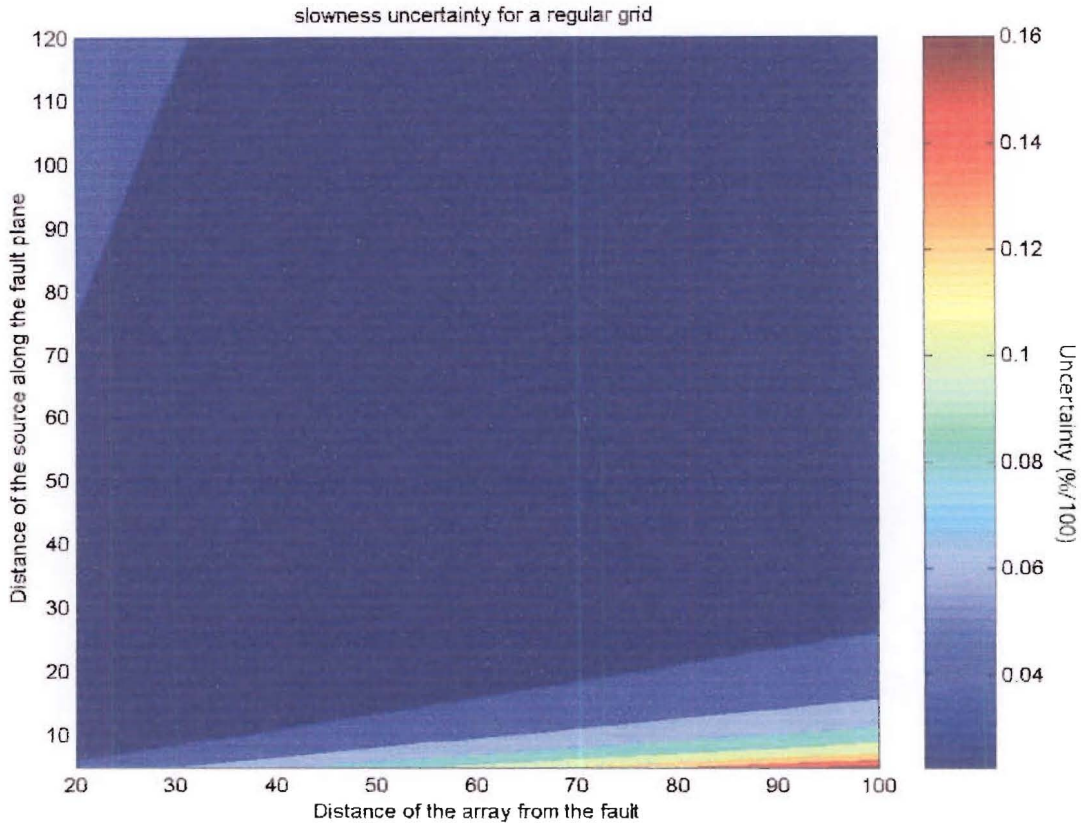

Figure 1B- 1: Slowness uncertainty for various array/fault configurations

As expected, the uncertainty increases when the slowness horizontal components are close to zero. Figure 1B- 1 also shows that arrays located less than 60 km away from the fault have a slowness uncertainty lower than 8%. Also, arrays closer to the fault are better whatever the distance of the source along the fault.

When looking at the uncertainty as related to the azimuth, results are expected to differ from those obtained in the slowness uncertainty analysis. Azimuth uncertainty not only depends on the slowness value but also on the azimuth itself (Equation 1A- 28). Therefore azimuth uncertainty is minimised for angles equal to zero degrees (mod $\pi/2$). Azimuth uncertainties are computed using the same conservative values as above. The results are presented in Figure 1B- 2.

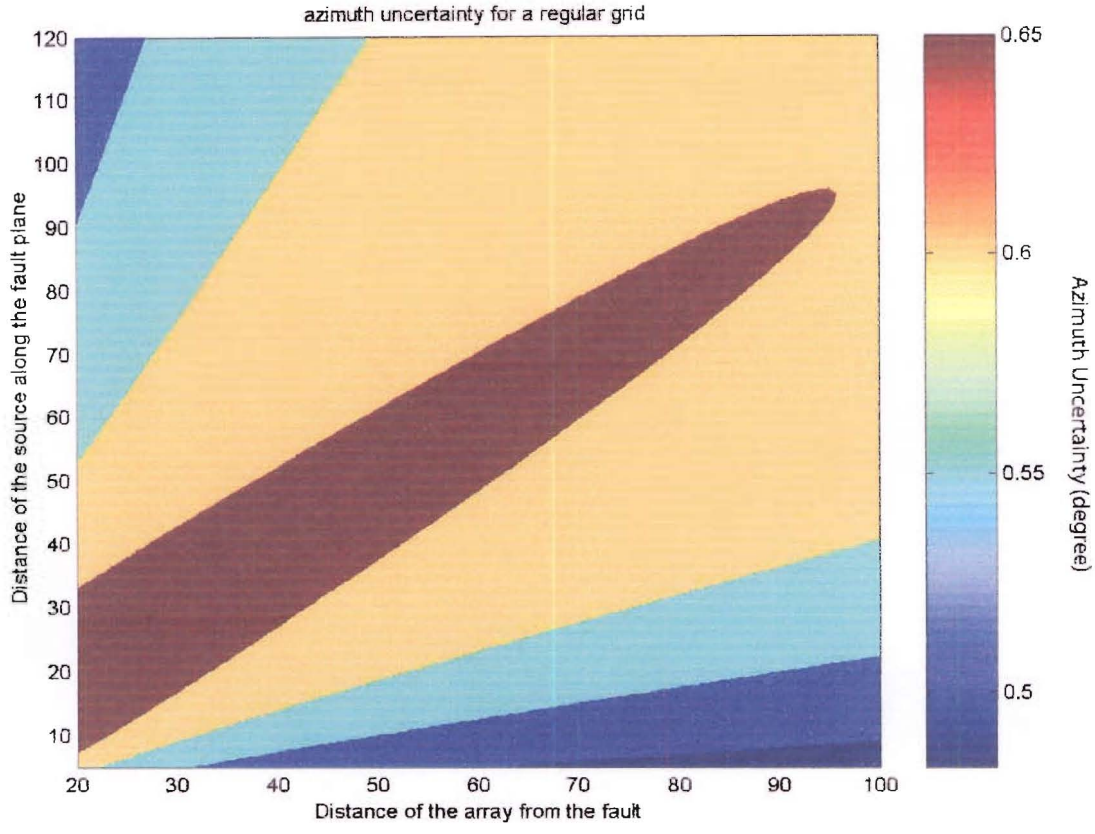

Figure 1B- 2: Azimuth uncertainties for various array/fault configurations (in degrees)

As expected, the azimuth uncertainty is maximised for angles $\pi/4(\mathrm{mod}\pi/2)$. Therefore arrays located away from the fault are better. Nonetheless, the angle differences are very small: 0.2 degrees maximum.

These two tests illustrate that one needs to find a compromise between locating the array close enough to the fault to limit slowness uncertainty, yet far enough from the fault to limit azimuth uncertainty. Nonetheless, both uncertainties are relatively small thus do not really constrain the optimal distances. The ray tracing method described in the following paragraph proves to be more confining.

1.2. Optimal distance to optimize the source projection

The interest in using the ray tracing estimation is that it takes into account both advantages of being close to the fault to catch rupture details and being far enough from the fault to catch sources rupturing away from the hypocenter. The method is based on ray-tracing back a slowness vector with some uncertainty added. For every point source on the fault, and each array location, there is a corresponding slowness vector. This vector is then modified by adding some uncertainty. The uncertainty is either variable in the case of a regular grid, or

constant in the case of the particular irregular grid considered in chapter 1A. The new vector is ray-traced back onto a new fault plane location. The error distance between the original point source and the new point source is computed. These error distances computed for various array/fault distances are an estimation of the efficiency of these various array positions. Figure 1B- 3 and Figure 1B- 4 shows results obtained using a regular grid and an irregular grid respectively for a maximum error contour of 10 km. The ray-tracing method is applied on arrays located 20 to 100 km away from the fault, point sources up to 120 km along the fault plane and using the same values as used in Figure 1B- 1 and Figure 1B- 2.

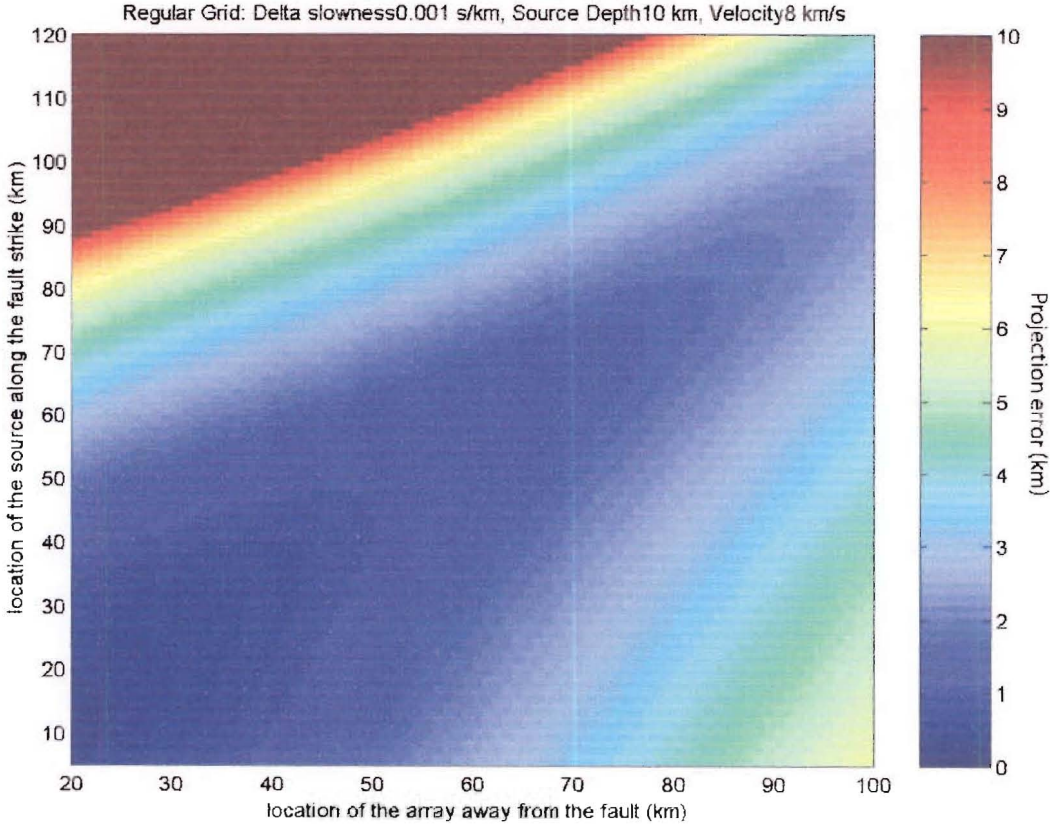

Figure 1B- 3: Projection errors for various array/fault configurations using a regular grid – contour up to 10 km

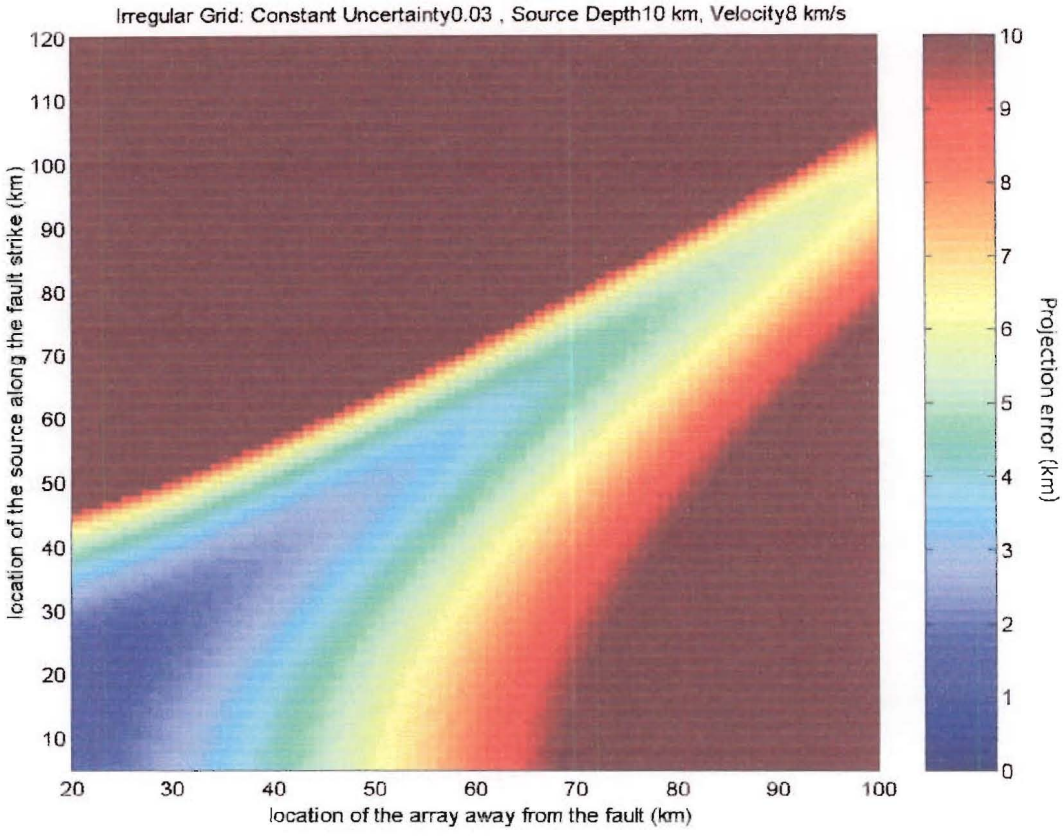

Figure 1B- 4: Projection errors for various array/fault configurations using an irregular grid – contour up to 10 km

Results for the regular grid presented in Figure 1B- 3 have shown errors up to 10 km and higher for sources located further than 90 km along the fault. Results for the irregular grid presented in Figure 1B- 4 show errors of 10 km or more for arrays as close as 40 km. Using an irregular grid therefore decreases the resolution of the results. This is due to slowness values increasing for close array/fault positions, which in turn increases the grid spacing or slowness error.

An upper limit for error distance is chosen to be two kilometres. For this value, Figure 1B- 5 shows that the maximum distance for an array from the fault is about 50 km. It also shows that an array located at 50km is able to visualise sources up to 60km along the fault.

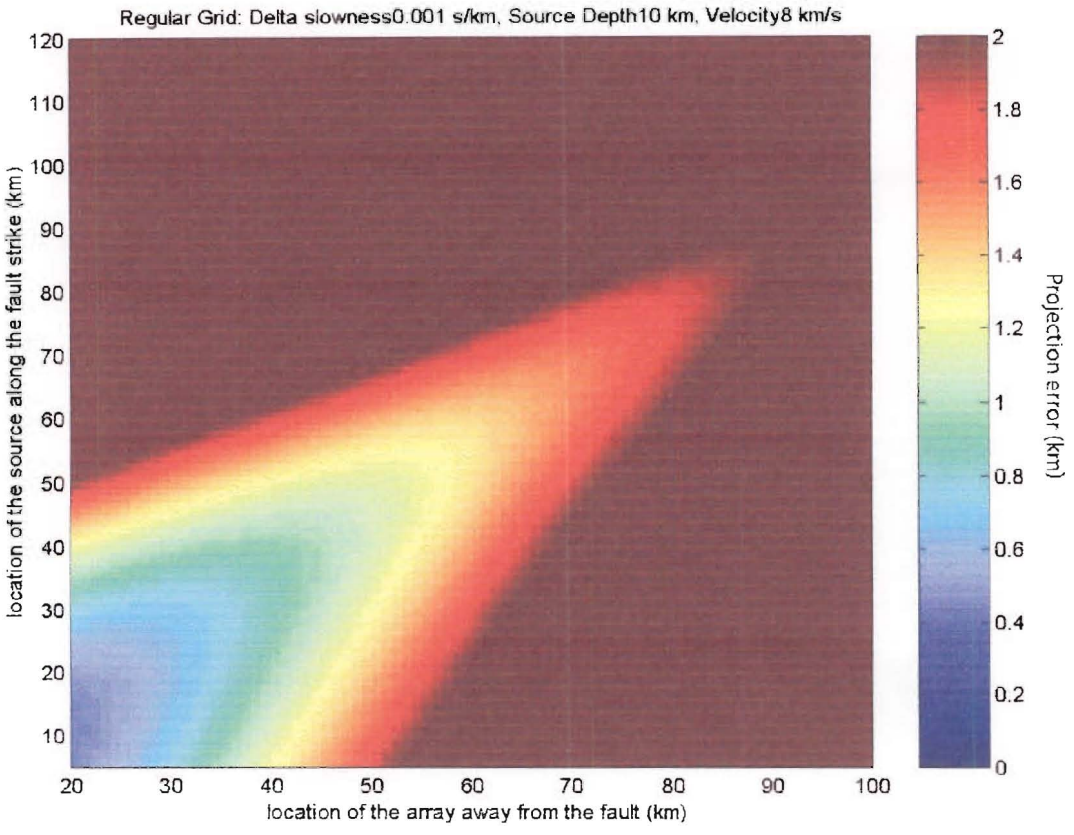

Figure 1B- 5: Projection errors for various array/fault configurations using a regular grid – contour up to 2 km

To conclude, a regular grid is better suited for this fault study; arrays located up to 50 km away from the fault are ideal. Again, these tests were performed using conservative values; therefore better results should be expected from the specific case studies in chapters 2 and 3.

1.3. How many arrays?

The method above concludes that a dense array should ideally be located between 20 and 50 km away from the fault. In case of an array located 50 km away from the fault, the length of fault coverage is close to 60 km. In the case of a fault rupturing bilaterally the distance potentially monitored by such an array is up to 120 km.

The optimal number of arrays is a function of the optimal distance previously determined and of the fault length. An optimal array can study up to a 120 km long fault. The Alpine fault being 400 km long, setting up three arrays would be ideal. Also, having more arrays looking over the same area would help increase the accuracy of the results.

2 Optimal array configuration

An array configuration is defined by the geometry of the array and the spacing between the instruments composing the array. Simple tests have been carried out in order to assess the relative importance of the geometry and instrument spacings on the array efficiency.

2.1. Method

The method is based on comparing the position of a known point source with the location of the projected slowness vector computed using dense array analysis. The measured distance is the mismatch criterion. The criterion is computed for grid points belonging to the fault plane. Simulated signals at a trial array were generated from the point sources using the 3-dimensional wave equation.

2.2. Input Model

The network is located 10 km from the centre point of the fault trace (Figure 1B- 6). To keep the tests financially realistic, the arrays have been restricted to 9 instruments in these tests. The chosen 10-km distance does not reflect the optimal distance defined previously, as the primary interest here is to test various configurations. The velocity model is a 3-dimensional uniform block with velocity of 4km/s.

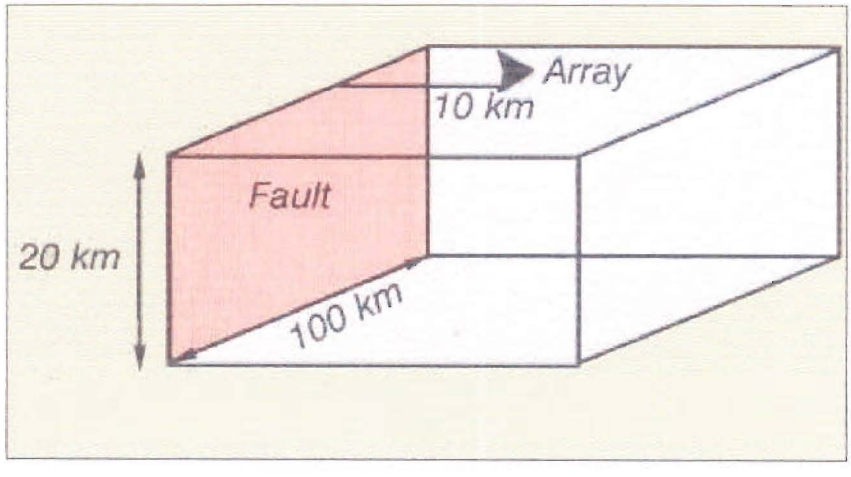

Figure 1B- 6: Array-fault configuration

Three array configurations are tested: circular, L-shape and basket for 200 m and 1 km instrument spacing. The circular configuration has been chosen for its complete angle coverage. Nevertheless, in a mountainous region like Canterbury/West Coast, valleys may be the easiest place to set up instruments and therefore L-shape or basket-shape arrays might be

the most feasible. The circular configuration comprises two concentric circles of 4 instruments each surrounding a central station (Figure 1B- 7a). The L-shaped array is composed of two orthogonal branches of 4 and 6 instruments, with the longer branch being parallel to the fault line (Figure 1B- 7b). The design of the basket array is such that all the instruments are within the angular fault zone, in a radial configuration (Figure 1B- 7c).

The model fault is a vertical fault with the following dimensions: 100 km long, 20 km deep, and 0 degrees of strike. The fault plane is decomposed into a grid of 231 points spaced at 5 km in length and 2 km in depth.

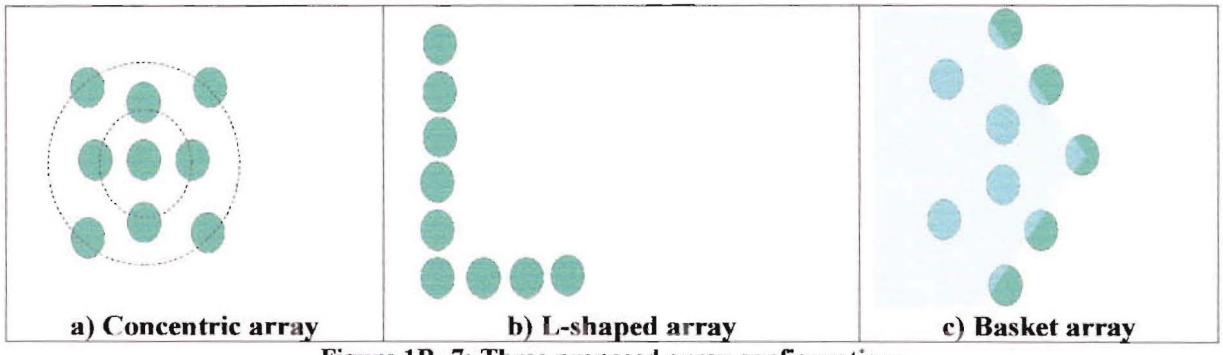

Figure 1B- 7: Three proposed array configurations

2.3. Results and interpretations:

Efficiency of the network for various instrument geometries

In this first series of tests, three arrays are tested. The spacing of the instruments is fixed to 1 km and only the geometry of the arrays is changed. Figure 1B- 8 shows that the spectra all have the same pattern: in the central part of the fault plane the resolution of the sources is optimal, and then becomes lower for more distant parts of the fault. The fault spectra also show different features. Comparing Figure 1B- 8 a, b, and c, it appears that the efficiency of the L-shaped array is much lower than that of the other arrays. Its optimal resolution zone is narrow and the peak distance value (the mismatch criterion) is 80 km, whereas it is only 10 km for the concentric and basket arrays. It also appears that, although the basket array was expected to perform better, its efficiency spectrum is very similar to that of the concentric array.

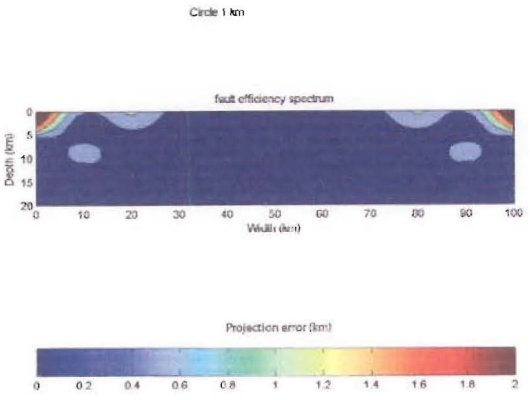

a) Concentric array – 1 km spacing

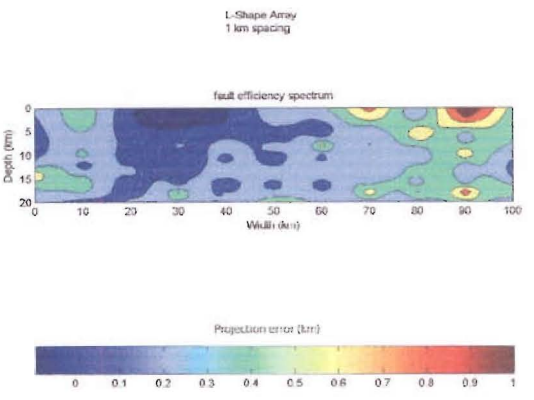

b) L-shaped array – 1 km spacing

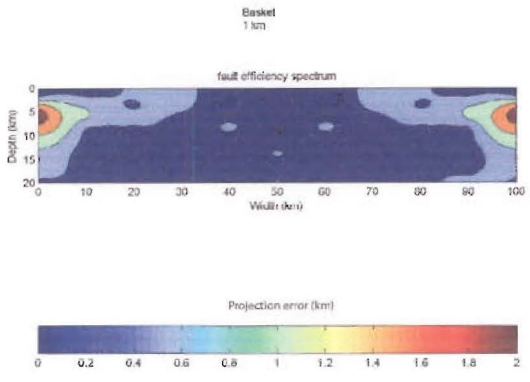

c) Basket array – 1 km spacing

Figure 1B- 8 Efficiency spectra for various array configurations

From these simple tests, we can conclude that there is a major difference in the efficiency of the arrays depending on their geometry. It appears that circular or basket geometry should be adopted. The drawback of a basket array is that it would miss out on the rupture of nearby faults in other directions.

Efficiency of the network for various instrument spacings

Here we compare two array configurations (circular and L-shape) with varying instrument spacing. Figure 1B- 9 shows the array efficiency spectra for the concentric array and the L-shaped array with instrument spacings of 1 km and 200 m. The resolution for the concentric array (Figure 1B- 9a and b) did not improved by reducing the instrument spacing. It does have however a major influence on the L-shaped array efficiency spectrum (Figure 1B- 9 c and d). With 200 m spaced instruments, the L-shaped array efficiency spectrum becomes as good as the efficiency spectrum of the concentric array.

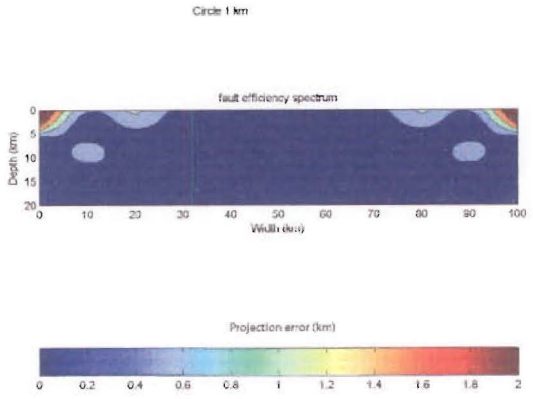

a) Concentric array – 1 km spacing

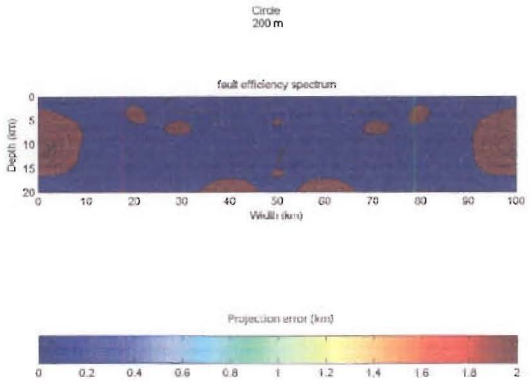

b) Concentric array – 200 m spacing

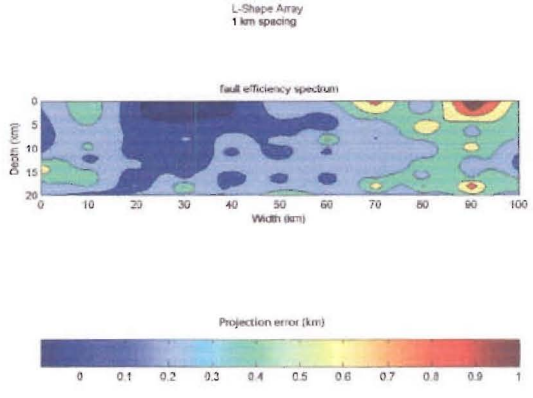

c) L-shaped array – 1 km spacing

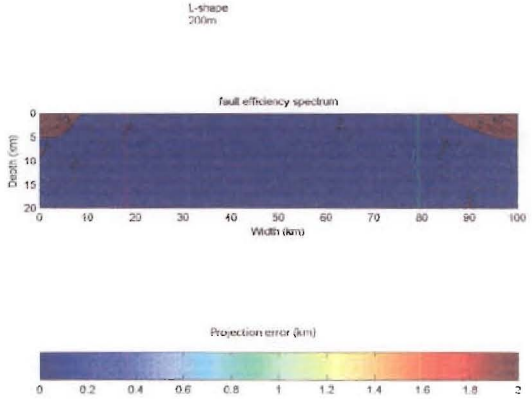

d) L-shaped array – 200 m spacing

Figure 1B- 9 various configurations and instrument spacings

Depending on array configuration, changing the instrument spacing can either have little effect on the efficiency of an array or improve greatly its efficiency spectrum. Because L-Shaped arrays may be the only possible configuration due to the field constraints, it is important to know that their array efficiency spectrum can still be improved.

3 Conclusion on optimal distance and configuration

As shown from the preliminary tests, the array configuration has a major influence on the efficiency of the array to detect seismic sources on a fault. Amongst various proposed configurations, not only did the circular array prove to perform best but also it would allow efficient recording of rupture on other faults in the region – such as the Hope fault, which also has high potential for rupture.

However the final configuration may be influenced by geographic constraints, which make a circular array design impossible but allow for an optimised L-shaped one.

Nevertheless, in the end, the optimal location and configuration are the ones that fit in with the field constraints as detailed in chapter-1C.

C Site selection

1 Requirements and constraints

1.1. Array limitations

Setting up an array of many closely spaced seismic recording instruments in a remote region involves constraints associated with the local geography and geology as well as the size, location and orientation of the fault plane.

Fault constraints

Some of the fault constraints specifically related to the study of the Alpine fault are as follow:

a) Location of the array on the eastern side of the fault plane

The Alpine Fault is dipping to the East at an angle of approximately 45 degree (Long et al., 2003). By locating the array on the eastern-dipping side of the fault, seismic waves will be recorded earlier by the instruments than if they were coming from a fault plane dipping away from the array. By doing so, the signals are recorded with less attenuation and complexity. The source signal is also better resolved when ray-traced back onto the fault plane. This is a major constraint given that the topography is much flatter on the western side of the fault, whereas, the relief of the eastern area is primarily mountainous.

b) Array located within 20 to 50 km of the fault trace

This part is detailed earlier in chapter 1B. The proposed range of distances combines two requirements:

-to be far enough from the fault plane to capture as many sources as possible

-to be close enough to the sources to get a good resolution of the signals

c) Coverage of the northern segment of the fault

Given that an array is ideally able to cover up to 120 km of fault length, studying the entire Alpine Fault would require installing multiple arrays. Due to budget and time constraints, however this study will focus on using just one array. Studies (Yetton, 2000) have shown that the northern segment running from Haast to Spring Junction is the most likely to rupture. Therefore it is a priority that the array be located near the northern segment.

d) Coverage of the Hope Fault

The Hope fault belongs to the North Canterbury fault system, splaying off the Alpine Fault about half way through the northern segment (Figure 1C- 3). Recent studies have shown a

rupture is likely within a short period of time. By placing the priority on a northern Alpine Fault segment array, we are also aiming at covering the southern segment of the Hope fault.

e) "Open" Area of 2x2 km^2

The need for power and communication raises material constraints. Setting up the entire array in an open space eases both the installation and maintenance requirement of the array. The final open space will have a strong influence on the shape of the array, constraining both its geometry and aperture. Depending on the available surface, some configurations are better suited than others. For instance, wide valleys can accommodate all types of array geometry while narrow gorges would confine the geometry to a T or an L shape.

Geologic constraints

To avoid amplification of the recordings due to site effects the instruments preferably should be installed upon bedrock. As a minimum the instruments should all be installed upon the same material. These requirements represent a major constraint given that rock outcrops are usually associated with reliefs that are difficult to access.

For example, the SMART-1 array in Taiwan (refer to chapter 3) had instruments spread over both 4 km^2 of open flat land sediments as well as bedrock of nearby rocky hills. These very different soil conditions lead to amplifications and distortions of the recordings (Figure 1C-1).

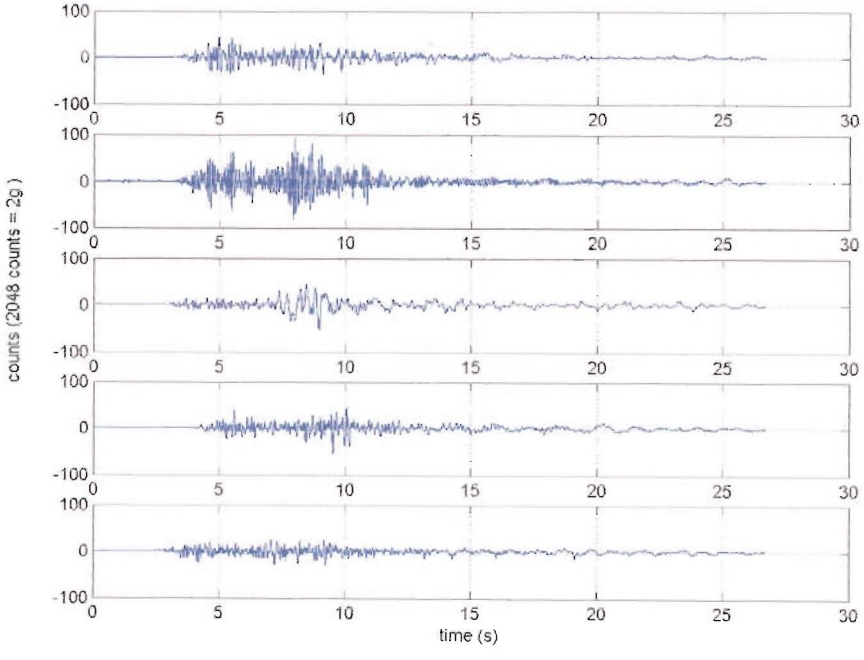

Figure 1C- 1 Seismograms of the same event recorded at five stations from the SMART-1 array

Figure 1C- 1 shows that although the stations all belong to the SMART-1 array, site conditions can lead to dramatically varying recordings. The amplitude of the seismogram at the centre of Figure 1C- 1 is very small when compared to the amplitude of the seismogram directly above it. The frequency content is also very different with the lower most recordings showing more high frequencies than the seismogram at the centre. Nonetheless with SMART-1 being an array of many stations, the effects were not so strongly felt in the dense array analysis (Chapter 3). In our case however the future array will have a limited number of stations; therefore, the sites need to be chosen carefully. As the proposed site is likely to be in a mountainous area, the possible choices are limited to an ideal rocky location in the mountains or an easily accessible valley location. The terrain conditions in the region of study are illustrated in Figure 1C- 2.

Figure 1C- 2 : Search for an array location in the Canterbury region: flat river valley and soft soil, or rocky mountain and bedrock? (Photo taken from Burnt Face looking northwest into the Waimakariri Valley, near Arthur's Pass)

Map summary

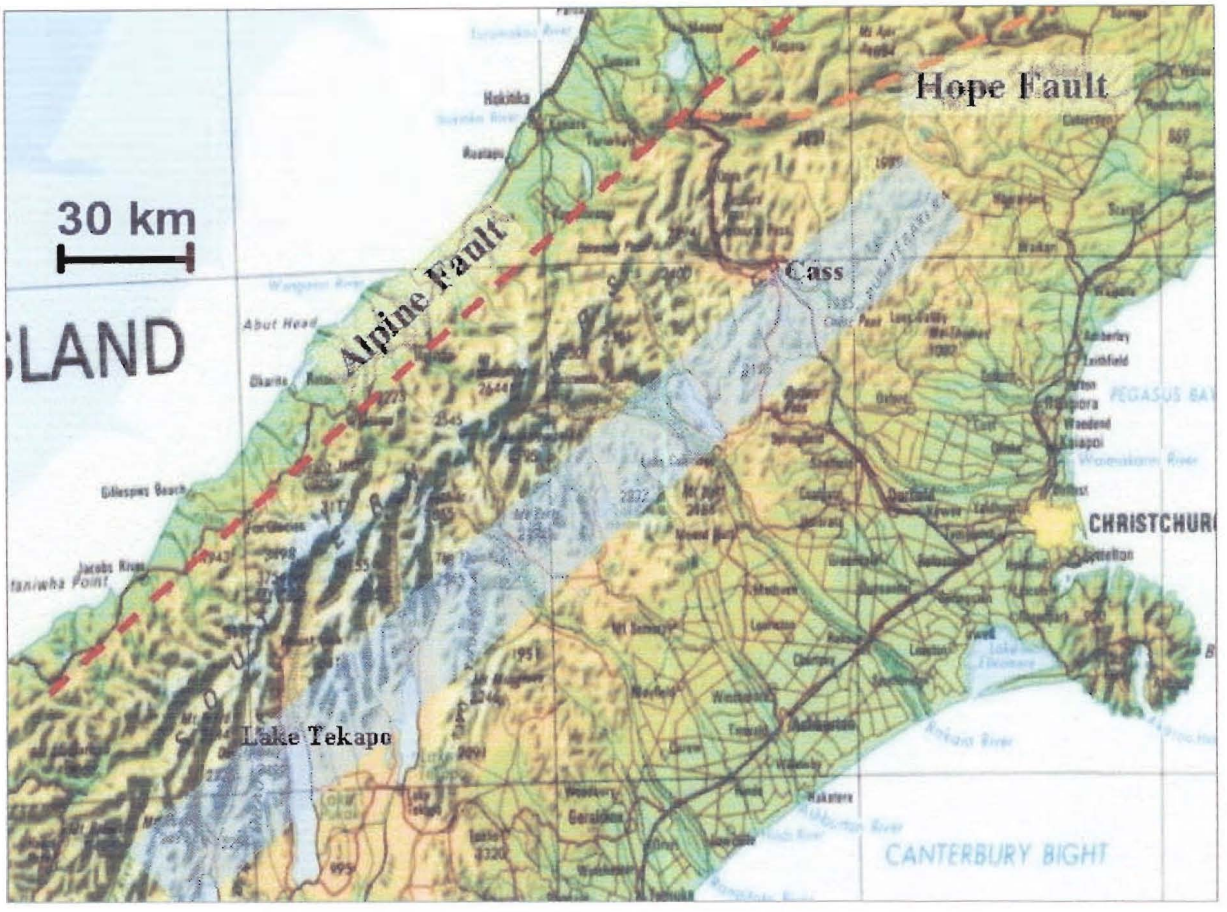

Figure 1C- 3 : Canterbury-West Coast region: selection of a potential region for ideal array locations

Figure 1C- 3 illustrates the regional area that comprises potential sites for an optimal array location. The area in grey shade is a compromise between all the following constraints described previously:

a. Located to the eastern side of the Alpine Fault plane
b. More than 20 km away from the fault plane
c. Away from the highest mountain ranges
d. Less than 60 km away from the fault trace.

1.2. Instrument requirements

Human aspect

It is important to set up the array away from populated areas in order to protect the instruments from cultural and environmental noises, as well as from material degradation. Nonetheless, installing and maintaining instruments requires regular site visits. Therefore a compromise must be made between locations with easy access and those that are quiet and secure.

Technological requirements

Power supply: solar panels

Solar panels are the only practical way to provide power in remote areas. They require at least 4 hours a day of sunlight to be efficient. Therefore the proposed sites have to be located in an area that gets sunlight every day of the year. This constraint eliminates locations such as valleys or slopes facing south.

Communication system: landline phone, cell phone or radio link?

Communication to and from the instruments is an important aspect of the array location. The instruments need to be contacted remotely, to be able to communicate to each other, as well as to exchange data with a central system that will be in charge of collecting recordings. Landline phone communication is the ideal solution, although the availability of which is unlikely. There is then the solution of cell phone communication, although coverage is usually very poor within our region of interest. As a last resort radio linked instrumentation is an option. This is rather costly, however, and would most likely require a relay-antenna.

2 Proposed regions for the South Island

The potential sites that satisfied most of the above constraints are, from North to South: Cass, Lake Coleridge, Heron, Mesopotamia up the Rangitata River and Mount John by Lake Tekapo (Figure 1C- 4).

Figure 1C- 4: Potential sites for a dense array

All these sites are located within the distance range suitable for array studies. The following ranking of the sites has been made first according to the priority of setting up an array towards the north end of the fault and then by analysing the advantages and disadvantages of sites individually.

2.1. Northern Array

The two competing sites for the northern array are Cass and Lake Coleridge. Cass and Lake Coleridge are both located on the dipping side of the Alpine Fault and close to the Hope Fault, which is another potential source of strong earthquakes.

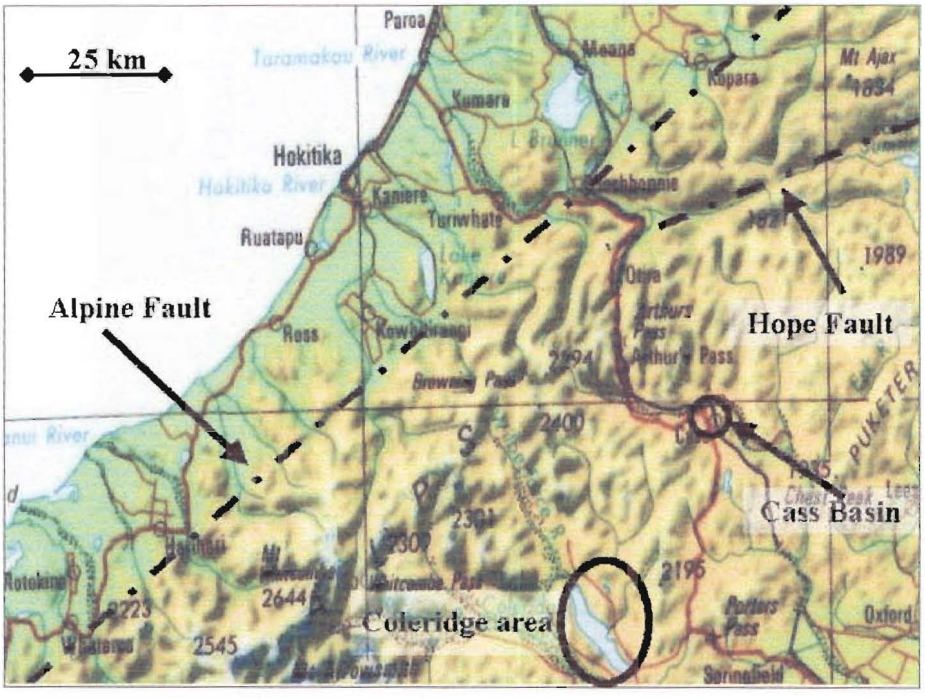

Figure 1C- 5: map showing the Coleridge area and the Cass basin

Lake Coleridge offers an open and remote space with easy access. But the remote aspect makes communications difficult. The lake region is also located further away from the Hope Fault than Cass.

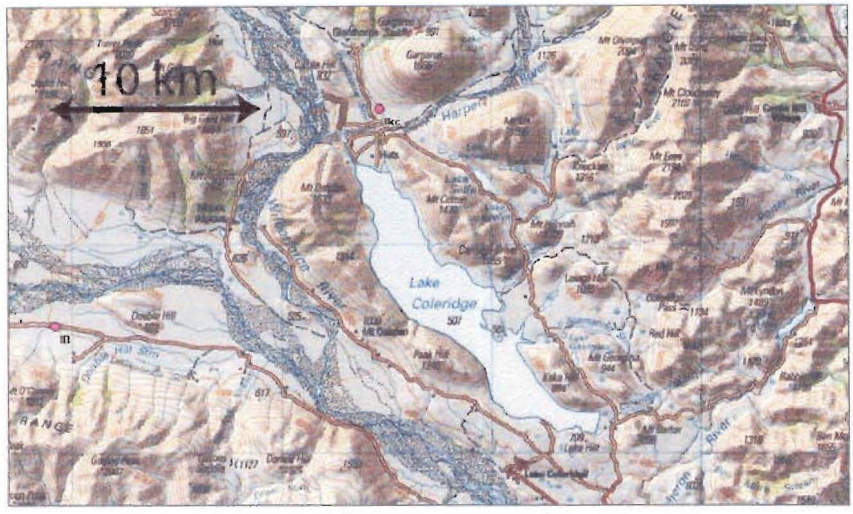

Figure 1C- 6: Map of the Lake Coleridge Area

The Cass Basin area has good communication solutions for the instruments. A number of potential sites facing Arthur's pass valley receive cell phone coverage. Other sites can be talked to by radio using the DOC (Department Of Conservation) radio network, while others could be relayed towards a main radio station based at the Cass chalet. This chalet is owned by the University of Canterbury and would be useful in the future as a base for the installation and maintenance of the array. The area also has a major road access that will ease and speed up the installation and maintenance of the numerous (and heavy) instruments. For the purpose of generating synthetic seismograms, the Cass Basin is an ideal location as it used to be surrounded by three SAPSE stations whose data can potentially be used as a source of empirical Green's functions.

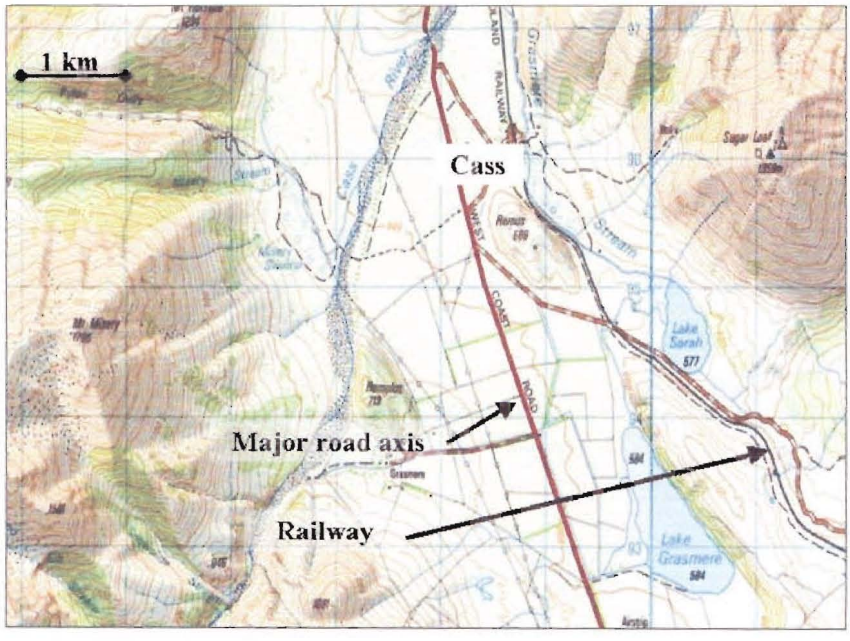

Figure 1C- 7: Detailed map of the Cass area

The major drawbacks of the Cass location are potential site effects due to the sedimentary layers that compose the basin, and environmental noise due to the region's proximity to a major road axis and railway.

Site	Pros	Cons
Cass	- Open space - Chalet owned by university - Easy access - Close to Hope Fault - SAPSE stations nearby - Many telecommunication solutions	- Basin soft soils - Close to major road
Lake Coleridge	- Open space - Easy access	- Further away from Hope Fault - No telecommunication

Table 1C- 1: Summary of Pros and Cons for proposed sites for the northern array

Overall, the Cass area is a more promising region to look for specific array sites than Lake Coleridge.

2.2. Southern array

Of the sites investigated so far for a future southern array, the most promising are Lake Heron, Mesopotamia and Mount John.

Site	Pros	Cons
Lake Heron	- Open space - Accessible	- Popular as an outdoor area (4x4)
Mesopotamia	- Open space	- Swampy
Mount John	- Gentle and wide slope - Owned by University	- A floating rock on soft sediments?

Table 1C- 2: Summary of Pros and Cons for the proposed southern array sites

3 Proposed sites for the Northern Array at Cass

The proposed sites are: Burnt Face, Pylon Gully and Long Hill (Figure 1C- 8). They are all located on rock sites that are remote but close enough to road access. They differ in their topography: Burnt Face is located on a wide slope facing North, Pylon Gully is located in a small gorge and Long Hill is on a long flat outcrop. The advantages and disadvantages of the sites are discussed in the following paragraphs.

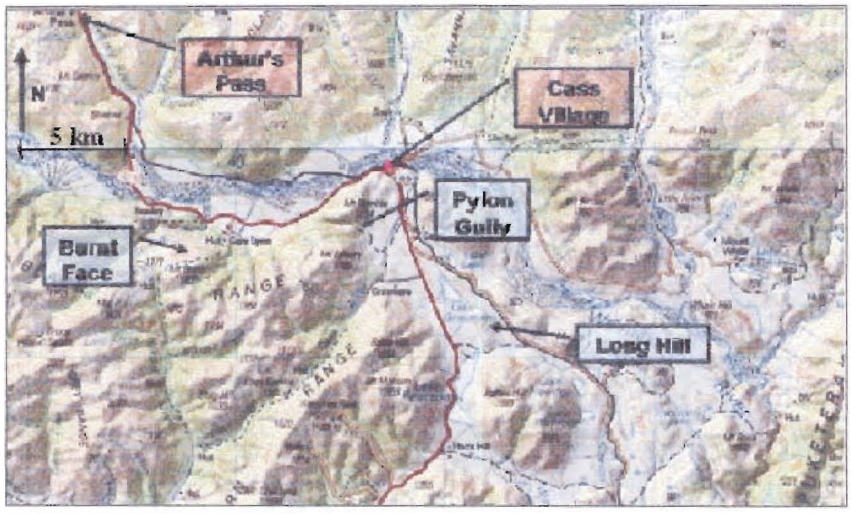

Figure 1C- 8: Location of the three proposed sites for the Northern array in blue.

3.1. On a slope facing North: Burnt Face

Burnt face is located South of Arthur's Pass (Figure 1C- 8). The area is a wide planar surface that is ideal to set up arrays of any geometry. As it is facing Arthur's Pass village along the Bealey river valley, it gets good cell phone coverage directly from the Arthur's Pass area. This cell phone coverage reduces the communication costs significantly. Another advantage of the Burnt Face site is its sunny location: Burnt Face is a flat landmass facing directly north. It receives sunlight for most of the day (Figure 1C- 9), which is a great advantage in running solar panels efficiently.

Figure 1C- 9: Burnt Face as seen from the main road looking south

Access to Burnt Face is not easy. It can be reached only by foot along a long and tortuous path or by helicopter. The cost of installing and maintaining many instruments would not be negligible. The major negative aspect of Burnt face however is the orientation of the slope relative to the location of the Alpine Fault and the Hope Fault. The direction of the expected incoming waves is North-North East. To reach the array, the signals would have to bounce back from a strong geological interface onto the slope. This would increase the attenuation and the complexity of the recorded signals.

3.2. In a Valley: Pylon Gully

Pylon Gully is a narrow valley located West of Cass village (Figure 1C- 8). It is a 2 kilometre long rocky gully separating Mount Horrible and Mount Misery (Figure 1C- 10). Its straight axis would only allow for T-shape arrays with the second branch of the T being along the side of the surrounding hills mentioned above.

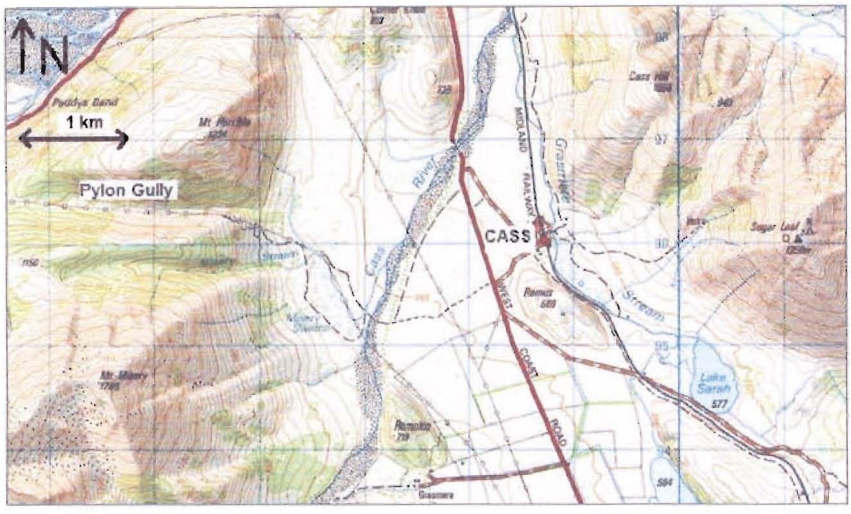

Figure 1C- 10: Location of Pylon Gully relative to Cass Village

The advantage of Pylon Gully is that it is a solid rock site. It is also quiet and isolated but has motorized access thanks to a maintenance road for the high tension electric power line running through the gully. The southern side of the gully is the sunny side as it is facing north and open enough to not have the sun obstructed by the northern side of the gully (Figure 1C-11).

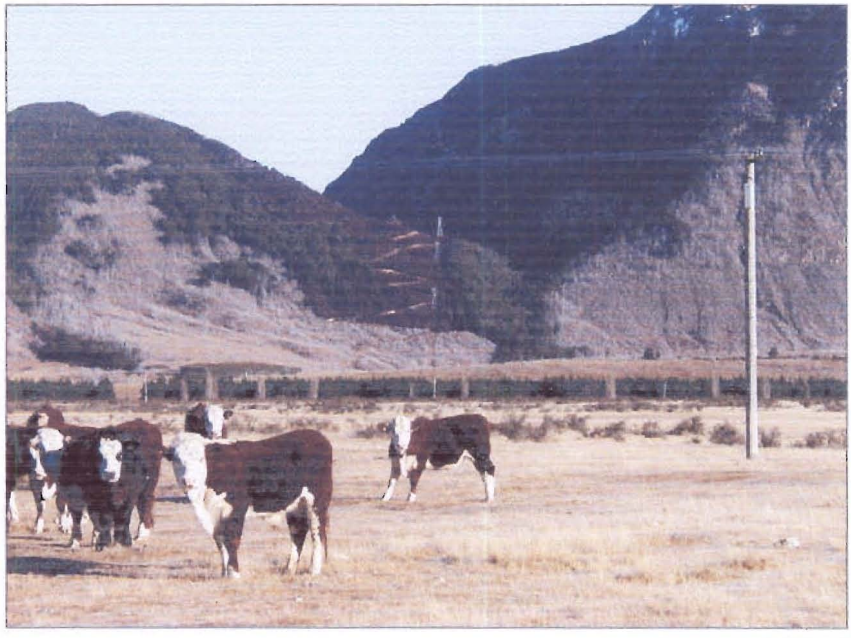

Figure 1C- 11: Pylon Gully looking west as seen from the main road (Cows are looking east).

Not only is the gully very close to the Cass Station, owned by the University of Canterbury, but it is also aligned with the University chalet. This is an ideal position for a potential radio network with a main receptor being located at the chalet (Figure 1C- 10).

Figure 1C- 12: inside Pylon Gully, looking west.

A major concern for this site is the presence of loose small rocks called 'scree'. A geological study of the site is necessary to determine if these rocks pose a threat to the instruments or would generate adverse site effects.

3.3. On a ridge: Long Hill

Long Hill is located south of Cass Village (Figure 1C- 8). It is a two kilometres long open space with a one kilometre long orthogonal branch. Long Hill has been selected as a potential site given its sunny location and easy access. Like Pylon Gully, it looks towards Cass Chalet and would allow radio transmission as a way of communication. Also Long Hill has been identified as a solid rock outcrop rather than just a big rocky block detached from one of the surrounding mountains (Pettinga, 2004, private communications). One could be concerned about the potential amplification of certain frequencies due to the hilly topography. Following Geli et al (1988), ground motion at mountaintops is amplified for wavelengths comparable with mountain widths. The width of Long Hill is on average one kilometre. The frequencies that might be amplified then are in the range of the subsurface velocities and thus are very unlikely to be in the 5-10 Hz range of frequencies we are interested in.

D Proposed dense array for an Alpine Fault earthquake scenario

1 Location

Pylon gully firstly comes out as the ideal array site for the Alpine Fault study. This site is easily accessible as well as away from main axes; it is located on solid bedrock, receives enough sunlight and has good hopes for communication. The Long Hill site seems also very promising. It is a bedrock site, has good sunlight and communication solutions. Also the instruments are safer than on the Pylon gully location (no risk of rocks falling down).

Nonetheless, Pylon Gully was the site finally chosen to run the synthetics. The major reason was that there had been an opportunity to visit it. Choosing one site or the other did not matter so much for the synthetics as the array aperture and configuration would not be very different. In the event of a permanent array being installed in the future, a serious site investigation is necessary to make the best choice.

2 Number of instruments

Twenty was the initial number of instruments proposed for this project. Nonetheless, to be realistic budget wise but still efficient, a minimum of about 10 stations sounded reasonable. A T shape configuration fitted the topography best. Various instrument spacings and aperture were tested; a number of 11 stations was best to optimize sub-array processing and wave sampling. Later on, looking at the first results obtained with the synthetic, it appeared that the resolution of the slowness spectra along the North-South direction was poor. Thus a twelfth station was added to complete the N-S branch of the array. Finally the proposed array is composed of 12 stations, with the hope of adding more in the future.

3 Configuration

3.1. Geometry

The geometry is constrained by the topography. The appropriate geometry for Pylon Gully is a T-shape. The long branch of the T is set along the gully and the short branch along the Eastern side of the gully which is more accessible than the Western one. This configuration could still be improved later on by adding more instruments to the short branch to bring more balance to the array. This geometry could also be applied to the other potential site Long Hill, which offers the same principal axes as Pylon Gully.

3.2. Aperture and instrument spacing

Instrument spacing is determined by optimizing the range of waves than can be sampled through the array as well as optimizing the sub-array technique. The spacing should range from the hundreds of meters to kilometres. After testing various spacings for 10 stations first, then 11 stations, and finally 12, the ideal array that came out is the following (Figure 1D- 1):

- Seven stations along the East-West branch:
  - 100 m spacing between stations 1 to 4
  - 300 m spacing between stations 1, 4 and 5
  - 1 km spacing between stations 1, 6 and 7
- Six stations along the South-North branch:
  - 100 m spacing between stations 1 and 8
  - 300 m spacing between stations 1 and 9
  - 200 m spacing between stations 1 and 10
  - 500 m spacing between stations 1 and 11
  - 1 km spacing between stations 1 and 12

This gives the following 8 sub-array combinations:

- East-West branch:
  - 100 m for stations 1, 2, 3 and 4
  - 1 km for stations 1, 6 and 7
  - 300 m spacing for stations 1, 4 and 5
  - 400 m spacing for stations 3, 5 and 6
- South-North branch:
  - 300 m for stations 1, 8, 9, 10 and 11
  - 500 m for stations 1, 9, 10, 11 and 12
  - 200 m for stations 1, 8, 9 and 10
  - 800 m for stations 9, 10, 11 and 12

4 Conclusion and Discussion

The final array is the following:

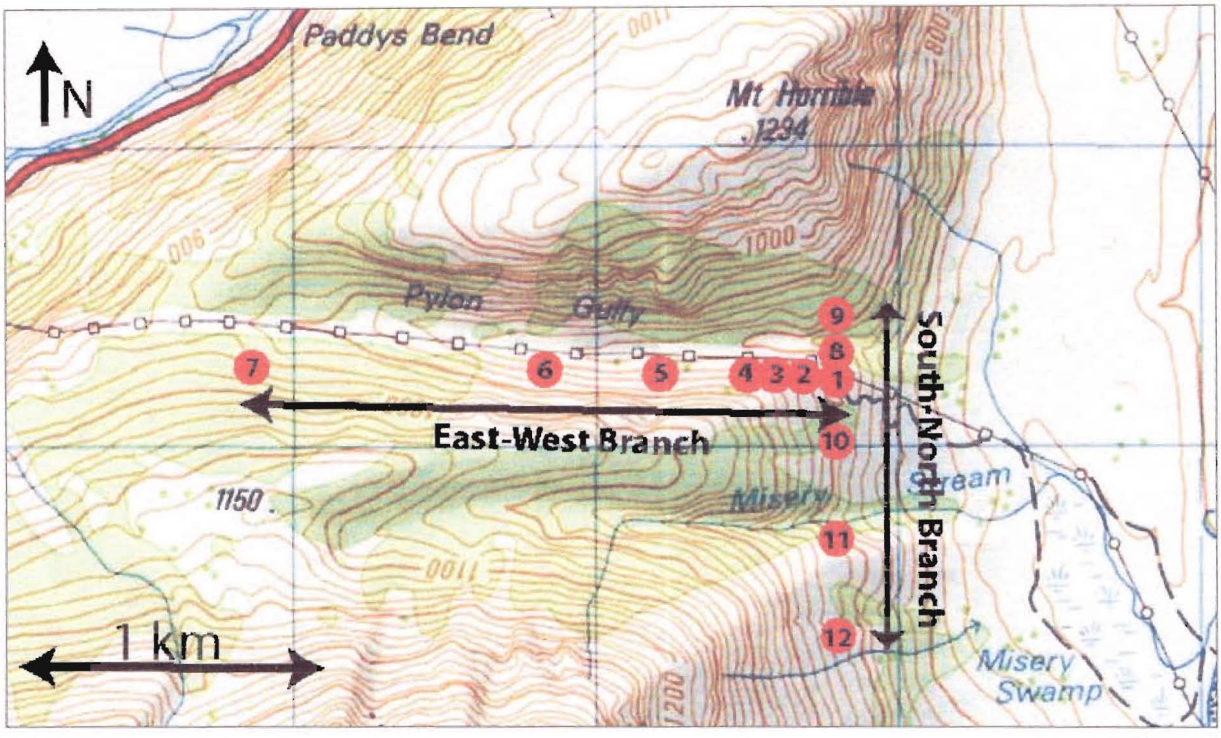

Figure 1D- 1: Proposed array for an Alpine Fault scenario

For this proposed configuration a 2-d spatial frequency transfer function of the array is computed. A 2-d spatial frequency transfer function illustrates the range of wavenumbers that are analysed optimally by an array. Ideally the transfer function should present only a single peak centred on zero. If secondary peaks appear, than the analysis should be restricted to the range of wavenumbers up to that secondary peak. For example, the transfer function from the study of the 9 station Annot array in France (Schissele, 2002) shows a clear secondary peak at 0.06 m^{-1}(Figure 1D- 2).

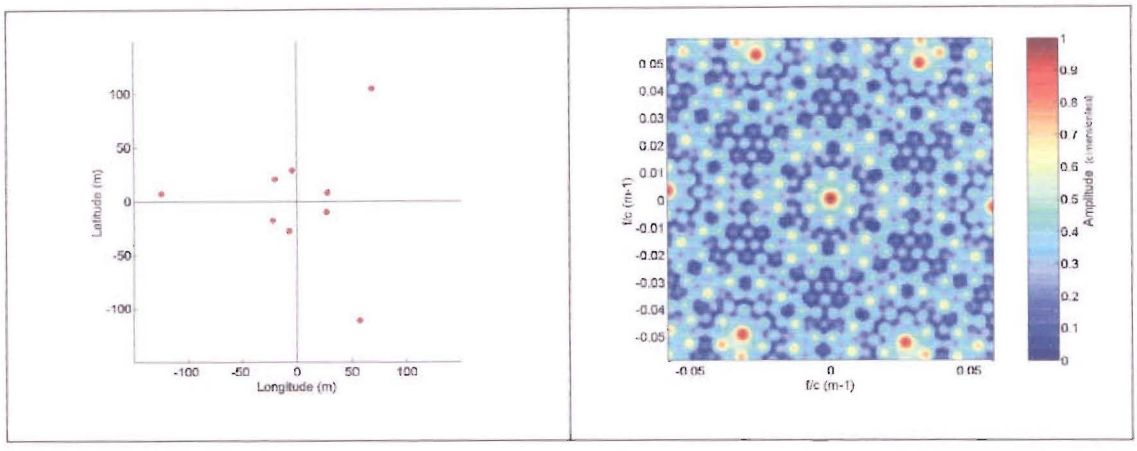

Figure 1D- 2: Annot Array: configuration and 2-d spatial frequency transfer function (from Schissele, 2002)

Given that the minimum velocity that will be used in the regional models is 4.75 km/sec and that the maximum frequency of study is 15 hertz (chapter 2), the maximum wavenumber to be studied is 19.84 km^{-1}.When looking at the transfer function of the proposed Pylon Gully array (Figure 1D- 3), there are no secondary peak appearing within the range of wavenumbers of interest. This demonstrates that Pylon Gully array is perfectly covering the whole range of wavenumbers of interest.

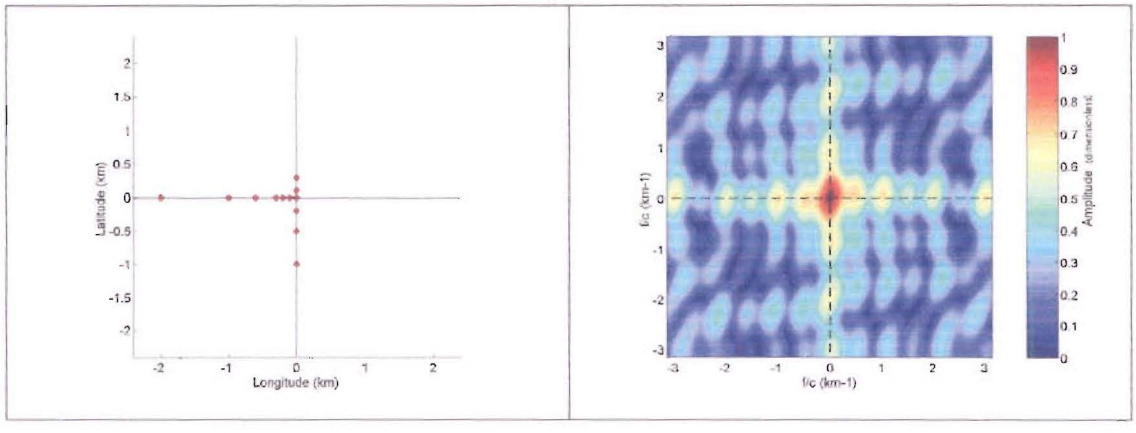

Figure 1D- 3: Pylon Gully array: configuration and 2-d spatial frequency transfer function

The proposed instrument locations shown above raise a few concerns. Station 8 and 9 are not located on the sunny side of the gully. Thus there will be a power issue for these two. This could be solved using bigger batteries, or running cables to a power source for instance. Also the elevation of the stations varies within the array. Given that all the stations are likely to be installed on the same substratum, the elevation difference can be corrected by adding or removing the computed travel time.

This array is the one proposed for testing by running synthetic seismograms. It possesses most qualities needed to make it a suitable dense array site for the region. Nonetheless, other

sites such as Long Hill also present many advantages; therefore installing the final array should require further investigations.

Chapter 2 – Measurements of simulated earthquake ruptures

A Introduction

Synthetic data are processed and analyzed applying dense array analysis. The objectives of which include:

- To validate the method by comparing quantitatively the rupture direction and velocity for the computed output rupture scenario and the known input scenario.
- To estimate the capability of dense array analysis to detect an eventual asperity.
- To understand the influence on the results of certain parameters such as the sampling rate and velocity model.

Given that no dense array data has been recorded within the region of interest synthetic data are required. An added benefit of synthetics over recorded data is to know the input parameters, and thus be able to model different rupture scenarios. The program chosen to create the synthetic data is EMPSYN (Hutchings, 1987). EMPSYN allows one to model realistic strong motion accelerograms by using empirical Green's functions. Empirical Green's functions make the modeled data more realistic as the geology and complexity of the media is taken into account. The empirical Green's functions used in this study are broadband data recorded during the SAPSE experiment conducted in the South Island, New Zealand.

This chapter introduces the program EMPSYN, the notion of empirical Green's functions and the model used in this case study. It presents the dense array analysis for two fault rupture scenarios, one with and one without a major asperity

B Strong motion synthetics for an Alpine Fault earthquake

This part introduces the program EMPSYN (Hutchings, 1987), which was chosen to create the synthetic seismograms. It also introduces the notion of empirical Green's functions, and describes the source and fault model for the region of study, as well as, the set of data used as empirical Green's functions.

1 EMPSYN and empirical Green's functions

The EMPSYN program uses empirical Green's functions to create synthetic seismograms (Hutchings, 1987). It has the advantage of creating an accurate synthesis of strong motion earthquakes, of dealing with a complex geology as well as allowing the user to choose from a variety of rupture scenarios.

EMPSYN uses empirical Green's functions (later called "EGF") to describe the geology corresponding to each ray path. In this approach, a recorded earthquake signal is the result of the original source signal and its subsequent modification on its path from the fault source to the instrument and through the instrument itself. Mathematically this may be expressed as the convolution of the source signal function with a function representing the effect of the geology and the instrument, the Green's function.

The EGF approach is an attractive method in the case of a complex geology that would be difficult to model, such as the geology of the Alpine Fault region. Also, given that the Alpine Fault generates over 100 earthquakes of magnitudes 2 to 4 per month, it is a good source of Green's functions for this study.

Nonetheless, the EGF method presents some constraints. The moment of the EGF is critical to the synthesized large earthquake, given that the large event moment is equal to the sum of the elemental source moments. The value for the corner frequency of the small events is also critical. In order to assume that the small events are point sources, their corner frequency must be higher than that of the synthesized large earthquake. Typically, a small event has a corner frequency higher than 10 Hertz. In the case where small events have corner frequencies smaller than the synthesized frequencies of interest, EMPSYN can deconvolve a Brune Source from the EGF to get a sharper impulsive point source.

In EMPSYN, the free parameters are the rupture geometry, hypocentre, rupture roughness, rupture velocity, healing velocity, slip distribution, slip vector and asperities (size, nature and location). The fixed parameters are the moment and magnitude of the earthquake.

EMPSYN is based on the representation relation developed by Aki and Richards (1980). Considering the moment density tensor

$$m_{pq}(X',t') = \mu.(\hat{s}_p\hat{n}_q + \hat{s}_q\hat{n}_p)K(X',t') \qquad \textbf{Eq. 2A- 1}$$

With:

- μ, the rigidity

- $(\hat{s}_p\hat{n}_q + \hat{s}_q\hat{n}_p)_i$, the focal mechanism with $\hat{s}$ being the slip component and $\hat{n}$ the fault normal.
- K(X',t'), the source time function
- Primed terms refer to the source
- Unprimed terms refer to the receiver
- $\otimes$ is the convolution operator

the displacement time history at station X can be represented by the following equation:

$$u_n(X,t) = \int_{\Sigma} m_{pq}(X',t') \otimes G_{np,q}(X',t';X,t)d\Sigma \qquad \textbf{Eq. 2A- 2}$$

Hutchings and Wu (1990) defined an EGF as an impulsive point source:

$$e_n(X'_0;X,t) = M_0(\hat{s}_p\hat{n}_q + \hat{s}_q\hat{n}_p)H(t'-t'_0) \otimes G_{np,q}(X'_0,t'_0;X,t) \qquad \textbf{Eq. 2A- 3}$$

Where:

- M_0 is the seismic moment of the EGF
- $H(t'-t'_0)$ is the unit step source-time function
- t'_0 is the origin time
- $G_{np,q}$ is the elastodynamic Green's function from unidirectional unit impulse in direction p at X'_0.

Given that the time-independent scalar seismic moment for the point source conditions is defined as:

$$M_{pq} = M_0(\hat{s}_p\hat{n}_q + \hat{s}_q\hat{n}_p) = \mu\bar{s}A(\hat{s}_p\hat{n}_q + \hat{s}_q\hat{n}_p) \qquad \textbf{Eq. 2A- 4}$$

The discretized representation relation can be written as:

$$u_n(X,t) = \sum_{i=1}^{N} \frac{\mu_i A_i S(t_i')_i}{M_{0i}^e} \otimes e_n\left(X, t_i' - \frac{\overline{\chi}_i}{\nu}\right)_i \qquad \textbf{Eq. 2A- 5}$$

Where:

- A_i is an elemental area such that $\sum A_i$ equals the total fault rupture area.
- M_{0i}^e is the scalar seismic moment of the source event.
- $\overline{\chi}_i$ is the radial distance from the hypocenter to the elemental source.
- ν is the rupture velocity.
- $e_n(X,t_i')_i$ is the empirical Green's function displacement for the i^{th} element.
- $S(t_i')_i$ is the desired slip function.

EMPSYN discretizes a fault rupture plane into elementary sources. It convolves EGF with a slip function for each elemental source. The slip distribution on the fault for all the elementary sources is such that the sum of all the moments of the elementary sources has to equal the moment of the synthesized large earthquake. Empirical Green's functions for sources where no EGF has been recorded are interpolated from the recorded measurements.

2 Source and Fault model for an Alpine Fault event

The input parameters for EMPSYN are the geophysical parameters of the medium, the fault and source models as well as the rupture parameters. In order to test the dense array method two models were run for strong motion events of the same magnitude with different rupture processes. Model 1 assumes a unilateral fault rupture with no asperity. Model 2 is identical to model 1 except for the addition of one asperity on the fault.

2.1 Geophysical parameters for the Canterbury/West Coast region:

The attenuation coefficient for the region is 400 (Eberhart-Phillips, private communication). The velocity equation used for the regional model is v_p=0.06z+4.75, which gives v_p=8.2km/s@40km. The velocity equation is a linear interpolation of the layered velocity model from Eberhart-Phillips (1995).

2.2 Fault and source model

Given that previous studies (Yetton, 2000) have shown that a magnitude 8 earthquake is expected to occur on the Alpine Fault, the modeled events are assigned a magnitude 8 for a moment of 1.2×10^{28} dyne-cm. The fault model is a simplified model of the Alpine Fault with a 55 degree strike, a 45 degree dip (Long et al., 2003) and a 180 degree slip (right-lateral strike-slip).

Also, given that the northern segment of the fault is the most likely to rupture, and that the hypocenter location should be located at least one kilometer away from the fault edges, the hypocenter in both models is located close to the northern edge of the fault plane. Although the hypocenter should ideally be located in the lower part of the fault it is located in the upper part. This is in order to equally catch details of the fault rupturing upwards and downwards. The hypocenter is located at a depth of 9.93 km; in the fault plane it is located 14 km away from the surface trace of the fault, 20 km away for the northern edge, 20 km away from the bottom edge and 400 km away from the southern fault edge. This gives a fault length of 420

km, and a width of 34 km. The final hypocenter location for the two models is (–42.9033Lat, 171.4833Long) for a depth of 9.93 km.

2.3 Slowness maps

Slowness maps represent the values of the North-South and East-West components of the apparent slowness vectors for a specific array location and various source locations on the fault plane. These maps are used later on to project the slowness spectra back onto the fault plane. They have been obtained using the TauP Toolkit (Crotwell et al., 1999) using the following velocity model:

61 layers of 500 m

Velocities increasing linearly from 4.75 km/s for the P waves (2.74 km/s for the S waves) to 6.58 km/s for the P waves (3.79 km/s for the S waves)

The X component of slowness corresponding to the East-West direction is shown in Figure 2A- 1. The Y component corresponding to the North-South direction is shown in Figure 2A-2. The slowness maps are satisfying as they both present a good range of slowness values. However, given that they represent the apparent slowness components for direct waves, the maps present some discontinuities for sources located more than 5 km away from the hypocenter. For these sources, the chosen velocity model does not allow the generation of direct waves. As expected, the X and Y components are orthogonal. West of the fault plane, the slowness vectors have high X values and low Y values. East of the fault plane, the slowness vectors have high Y values and decreasing X values. Also, given that slowness vectors are the projection of the ray parameters, deeper source locations present lower slowness values for both X and Y components.

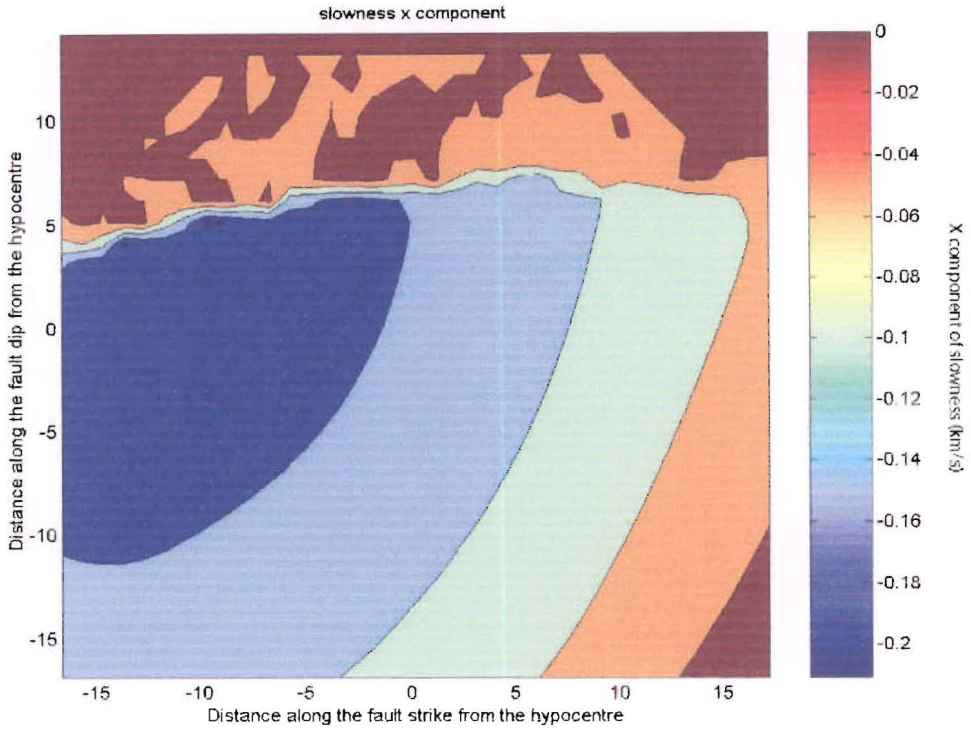

Figure 2A- 1: Slowness map for the East-West component of slowness. The noisy region above 5 km is due to a lack of point sources at shallow depths.

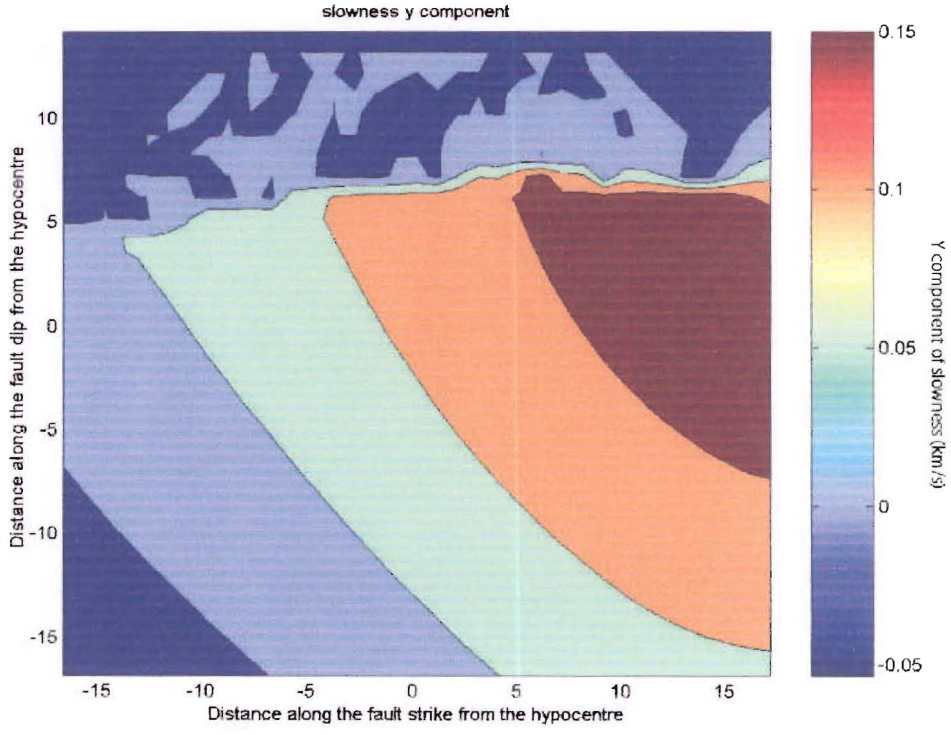

Figure 2A- 2: Slowness map for the East-West component of slowness. The noisy region above 5 km is due to a lack of point sources at shallow depths.

2.4 Proposed rupture scenarios

Rupture parameters for Model 1 with no asperity:

The model is a simple unilateral strike-slip fault rupture with a 180° slip. The rupture propagates in a circular shape. The rupture area is longer than the width of the fault so that the program can model the effect of a surface rupture. The fault diagram of model 1 is shown in Figure 2A- 3.

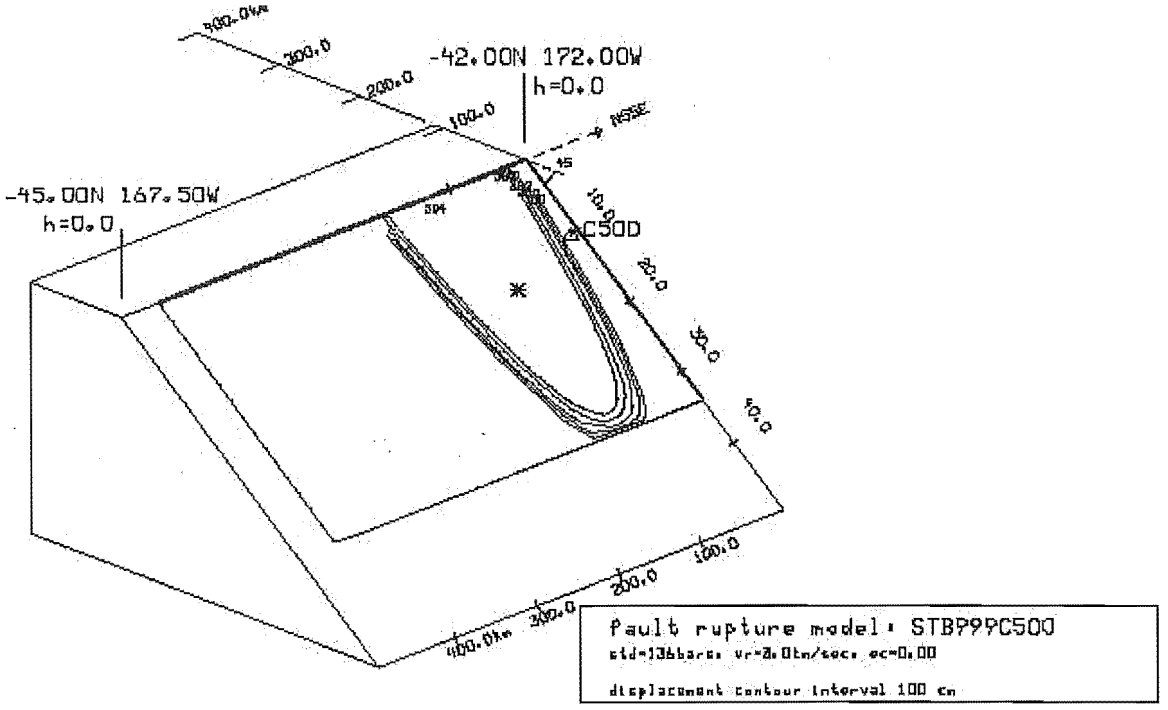

Figure 2A- 3: Fault diagram for Model 1 without asperity

Rupture parameters for Model 2 with one asperity:

The model here is identical to Model 1 described previously except for the addition of an asperity. In EMPSYN, asperities have a circular shape of diameter as determined by the user; the asperity chosen for Model 2 has a radius of five kilometers. The fault diagram for Model 2 is shown in Figure 2A- 4.

The user can choose between two asperity models. In the Hartzell asperity model, the asperity starts rupturing as the main rupture front reaches it. In the Kanamori asperity model, the asperity elements rupture independently from the main rupture front. Given that the array analysis is focused on the propagation of the tip of the rupture front, Model 2 was run with a Hartzell asperity model. Nonetheless, in the future, it would be interesting to assess the response of the array analysis to a Kanamori asperity model.

The position of the asperity on the fault is: (-2.9664 Lat 171.3608Long) for a depth of 9.93km. The asperity moment value is 0.12×10^{27} dyne-cm.

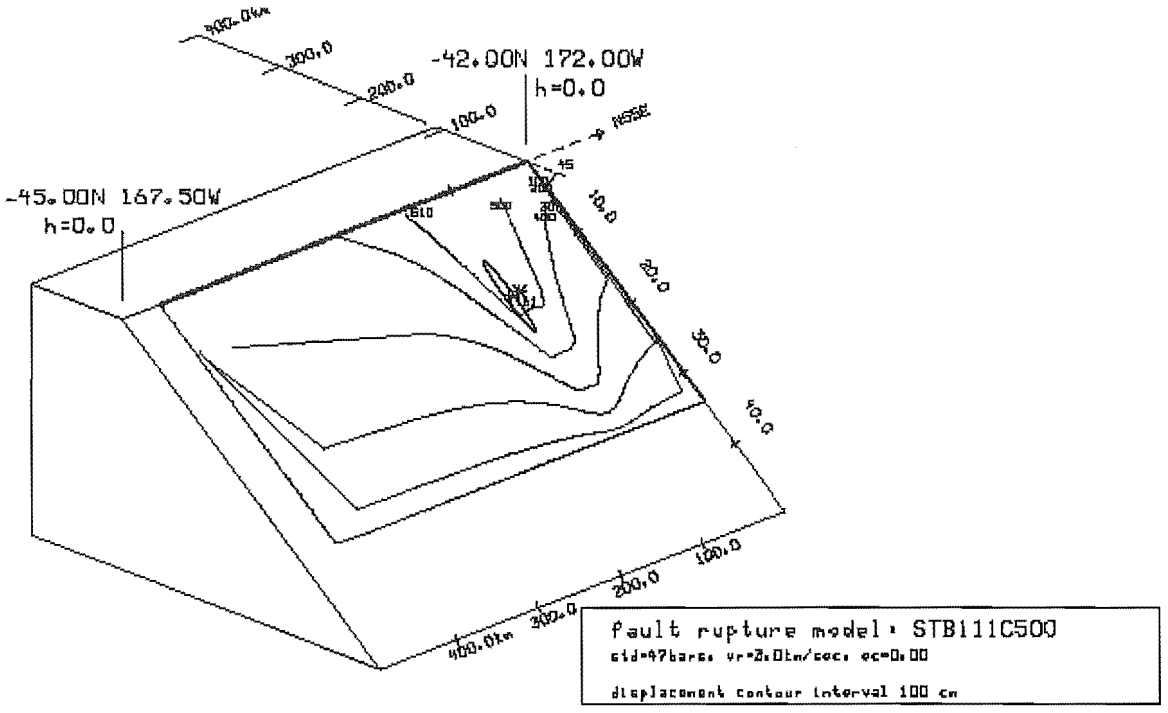

Figure 2A- 4: Fault diagram for Model 2 with one asperity

3 The SAPSE dataset

The purpose of generating synthetic strong motion seismograms is to, through array analysis, predict ground motion realistically at sites instrumented with strong motion accelerographs. Thus, the search for empirical Green's functions is limited to events with sources spread across the Alpine Fault, and recorded at sites instrumented with both broadband and strong motion instruments.

3.1. Presentation of the data

The New Zealand SAPSE (South Island Passive Experiment) dataset provides an ideal collection of small magnitude events. The SAPSE experiment consisted of 40 broadband instruments distributed over the South Island during the years 1995 and 1996 (Figure 2A- 5). It provides a very good catalogue of recordings spread all over the South Island. The program involved collaboration between the Institute of Geological and Nuclear Sciences of New Zealand, the University of Otago (New Zealand), the University of California, Berkeley (UCB), and State University of New York, Binghamton (SUNY).

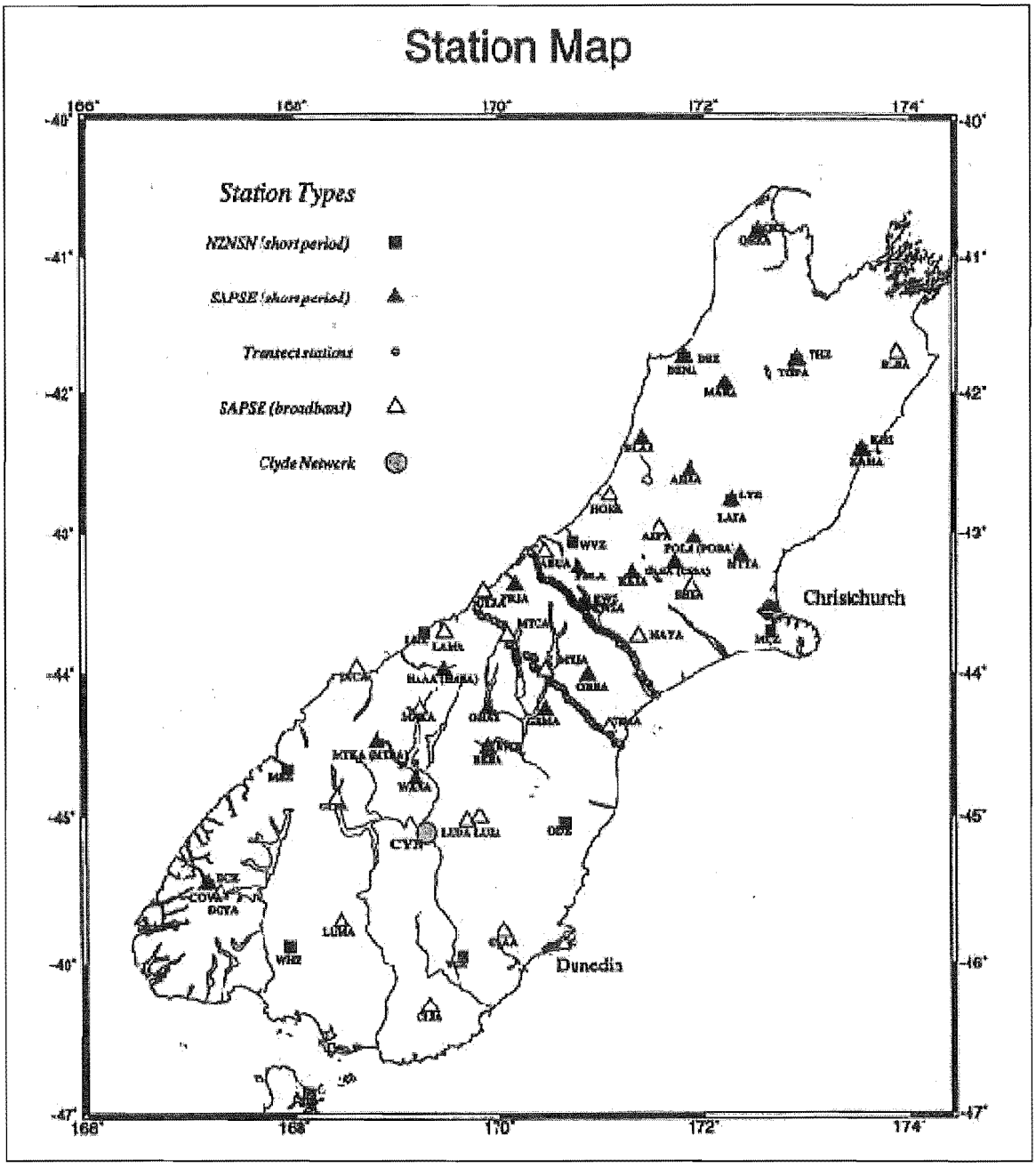

Figure 2A- 5: Location of the SAPSE stations

The following paragraphs detail the selection of SAPSE sites and data, as well as, results obtained after reprocessing.

3.2. Selection of events and stations

Nine SAPSE stations out of 40 were selected. All sites contained both broadband and strong motion instruments and recorded data over the same time period. The 9 selected stations are ARPA, HOKA, KAHA, LAMA, LUMA, MAKA, ABUA, MTCA and TIMA. These are shown in Figure 2A- 6. Surprisingly although the experiment lasted for more than a year, the

overlapping time of recordings was less than a month: from March 7th to March 31st 1996. A number of events occurred during March 1996, 35 of them satisfied the following conditions:

- Latitude between -42.5 and -44 degrees,
- Longitude between 167 55' and 171 42',
- Number of observations higher than 10,
- And magnitudes ranging from 2.3 to 4.2.

Figure 2A- 6: Selected SAPSE stations

The data, provided by IRIS (Incorporated Research Institutions for Seismology), were in a raw format and had to go through a series of corrections:

- Changing header values: starting time of the recording equals starting time of the recorded event
- Picking S arrivals
- Filtering using a Butterworth filter from 0.5 to 20 Hertz
- Averaging to get the mean values at zero
- Tapering the extremities of the recordings
- Removing the instrument response using the transfer functions provided with the data
- Changing the units from $m.s^{-2}$ to $cm.s^{-2}$ as required by EMPSYN

3.3. Computation of corrections and event parameters

Not all the source event parameters had been computed in the SAPSE data. One of them was the corner frequency of the events, which is an essential parameter to run EMPSYN. Also, one of the stations, ARPA (Arthur's Pass), had very low amplitude recordings for each event. This is illustrated in Figure 2A- 7a) which compares recordings of the same event at stations HOKA, ARPA, ABUA and LAMA with respectively increasing epicentral distances.

Given that the data were either incomplete or with some uncertainties, there was a need to check the event magnitudes and to compute their corner frequency. Netmoment (Hutchings, 2002) was the program chosen to perform these tasks.

Netmoment is a computer program developed by Hutchings (2002) to perform simultaneous calculations of moment and source corner frequency from network recordings. It uses fundamental knowledge of earthquake sources, propagation attenuation, and site response in a simultaneous inversion of network data. This is especially useful in this study as source parameters are difficult to determine for small earthquakes. The output is in the form of a displacement spectrum. The program fits the spectra for all the stations where an event has been recorded. The intersection of the curve with the vertical axis determines the moment of the event. The frequency for which the flat curve starts to drop determines the corner frequency of that event. Figure 2A- 7 b) shows the results for event 96069090255 recorded at stations ARPA, HOKA and LAMA.

The displacement spectra for event 96069090255 do not present the ideal characteristic of a theoretical displacement spectrum. Nonetheless, they show a plateau zone for the lower frequencies and a fall-off at about 3 Hertz. The main fall-off at 20 Hertz is due to the filtering applied previously on the raw data.

At this point, the main concern for the data is the very low amplitude of the spectrum for the ARPA station. This is confirmed by looking at the time histories of one event, for stations located at increasing epicentral distances: the ARPA station recordings appear to have very low waveform amplitudes by a factor of 5 to 10 (See Figure 2A- 7 a and b).

It was concluded that the defective amplitude must be due to a change of gain factor when acquiring the data. The report for the SAPSE experiment (Anderson et al., 1997) mentioned that the experiment used a Reftek data logger with STS-2 sensors. Referring to the original manual for the Reftek 72A data acquisition system, options for gains are: 0, 18, 30, 54, 66, and 78 dB. Given that 18 dB corresponds to an increase in gain by a factor of 8, it seemed reasonable to apply this factor back to all the ARPA recordings. This operation does not affect directly the array analysis results as amplitudes do not matter, but it was taken into account when analyzing the strong motion predictions.

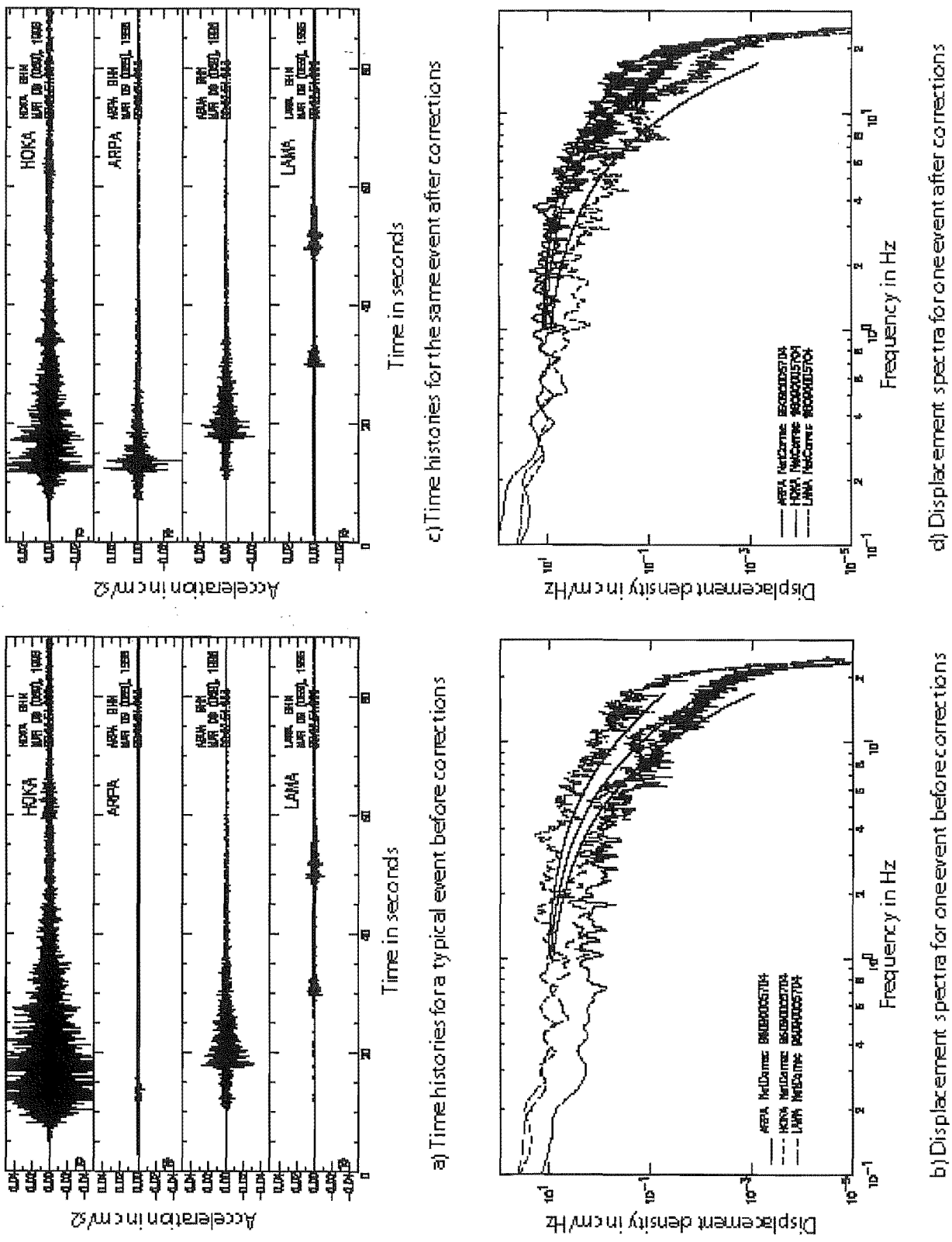

Figure 2A- 7: Comparison of time histories and displacement spectra for ARPA station before and after amplitude corrections

Figure 2A- 7c and d show the time histories and displacement spectra for one event after corrections applied to ARPA station. The waveform amplitudes of the signals are now coherent, and the ARPA spectrum has been shifted to the level of the other station spectra.

The spectrum for station LAMA shows a decrease in amplitude at approximately 2 Hertz. This observation has been made for all the LAMA recordings. Site effects would amplify the recordings, so it is thought that this pattern might be due to a travel path effect.

Table 2A- 1 shows the new magnitude and corner frequencies computed for the 35 events. Overall, the new magnitudes are smaller than the original magnitudes provided with the data. Also the corner frequencies are very small for events of small magnitude. Thus the sources must be deconvolved with a Brune function when running EMPSYN.

Event Name	lat	lat_min	long	long_min	depth	C mag	Net mag	Fc (Hz)
1996.067.03.15.34	43	6.08	171	3.2	12.37	2.9	2.5	3.2
1996.068.13.32.32	42	59.59	171	25.73	0.03	3	2.3	5.7
1996.068.23.20.27	43	0.91	171	27.27	17.15	2.6	2.4	7.7
1996.069.00.03.04	42	57.78	171	7.9	17.17	2.9	2.5	8.7
1996.069.09.02.55	43	3.41	171	4.94	3.15	3.2	2.7	3.1
1996.069.23.10.14	43	3.73	171	4.76	6.53	3	2.5	3.8
1996.072.00.31.54	43	14.68	171	4.66	8.29	2.8	2.4	3.3
1996.072.04.30.14	43	3.15	171	25.43	10.94	3.1	2.6	5
1996.072.10.34.29	42	54.18	171	38.99	10.2	2.7	2.3	5.1
1996.073.02.37.22	43	3.03	171	28.01	5.55	2.8	2.3	5.5
1996.073.11.54.27	43	1.2	171	25.78	10.66	2.5	2.3	2.16
1996.073.14.43.33	42	56.43	171	27.65	7.42	3.1	2.3	4.8
1996.073.23.57.36	42	57.07	171	30.69	7.44	2.9	2.5	11.7
1996.074.03.02.31	42	59.38	171	21.71	6.43	3.3	2.5	6.4
1996.074.08.14.40	43	4.34	171	1.69	11.5	2.3	2.4	7.7
1996.075.16.33.58	42	56.47	171	21.2	4.01	3.3	3.1	5.7
1996.075.16.41.13	42	55.84	171	22.14	0.03	3.2	3	4.9
1996.075.17.05.34	42	58.98	171	23.53	3.28	3.3	3.1	8
1996.077.19.26.11	43	0.88	171	23.74	3.89	2.9	2.6	3.3
1996.078.12.10.50	43	15.56	171	31.45	4.4	3.8	2.8	2.9
1996.081.07.54.16	42	58.34	171	22.07	11.42	3.1	2.5	5
1996.081.12.53.25	42	54.7	171	38.04	8.38	2.9	2.5	12.8
1996.082.06.27.52	42	57.65	171	32.08	3.47	3.2	2.5	16.6
1996.083.05.11.43	43	3.03	171	27.92	3.42	2.9	2.4	3.8
1996.085.23.16.18	42	57.46	171	29.2	3.6	3	2.6	6.5
1996.086.03.58.10	43	4.85	171	18.56	3.03	3.9	2.9	7.2
1996.088.05.06.30	42	57.25	171	21.54	7.99	3.1	2.6	7.9
1996.088.16.40.47	43	35.09	170	40.35	5.35	3.4	3.2	5.9
1996.088.18.58.37	42	58.47	171	25.6	11.75	2.3	2.7	7.2
1996.090.00.57.04	43	24.75	171	37.48	14.12	3.7	3.5	7.1

Table 2A- 1: List and parameters of selected events recorded by the SAPSE network. Depths are in km; C mag is the magnitude given by the catalog; net mag is the magnitude inferred from Netmoment; Fc is the corner frequency.

C Strong motion synthetics for an Alpine Fault earthquake

Synthetic accelerograms generated using the program EMPSYN are analyzed for two rupture scenarios: a rupture scenario without asperity and a rupture scenario with a major asperity located close to the hypocenter. The objective is to determine the efficiency of dense array analysis in capturing fault rupture parameters such as velocity and direction. Unfortunately, the horizontal data were not good enough to analyze. The alignment of the horizontal accelerograms, which is an essential part of the process, was inconsistent. This failure of the horizontal components may be due to the records used as Green's functions. Nonetheless, the analysis of the vertical data is very promising. In both studies, the East-West direction corresponds to the X axis, and the South-North direction to the Y axis.

1 Scenario without asperity

The first scenario is a simple unilateral fault rupture. Characteristics of the rupture are summarized in Chapter 2A. First the accelerograms are presented. They are followed by the slowness spectrum and the fault diagram analysis. Finally the results are compared to the input rupture parameters.

1.1. Results

The synthetic accelerograms

Synthetic accelerogram are generated at the 12 stations of the potential Pylon Gully array. Figure 2B- 1 shows the raw synthetic accelerograms obtained at three stations of the array: ordered from top to bottom, central station, A2000 and C1000. Peak amplitudes for each accelerogram are close to 400 mg, which is lower than expected for a magnitude 8 earthquake recorded at a close location.

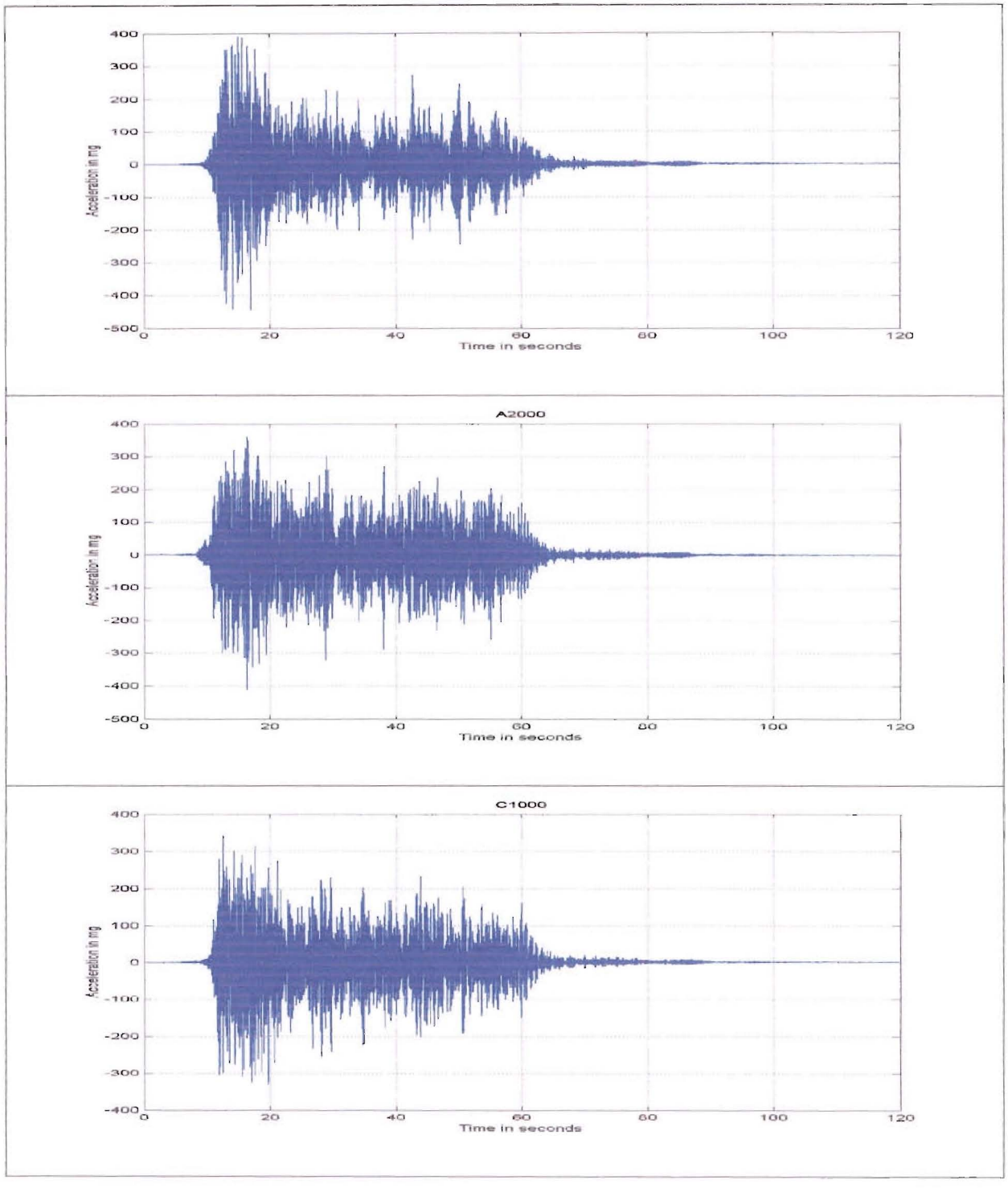

Figure 2B- 1: Raw accelerograms synthesized at the central station of the Pylon Gully array

The accelerograms present strong high frequencies. Figure 2B- 2 shows the Fourier acceleration spectrum of the central station accelerogram. The strong characteristics of the spectra are a zero flat response up to 5 hertz and a major peak around 19 Hertz. The occurrence of the 19 Hertz peak is explained by the Green's Functions used to generate the

accelerograms. A characteristic noise appears clearly on the acceleration spectra of the empirical Green's functions shown in Figure 2A- 7 d) in the way of a raise of the spectra amplitude after 15 Hertz.

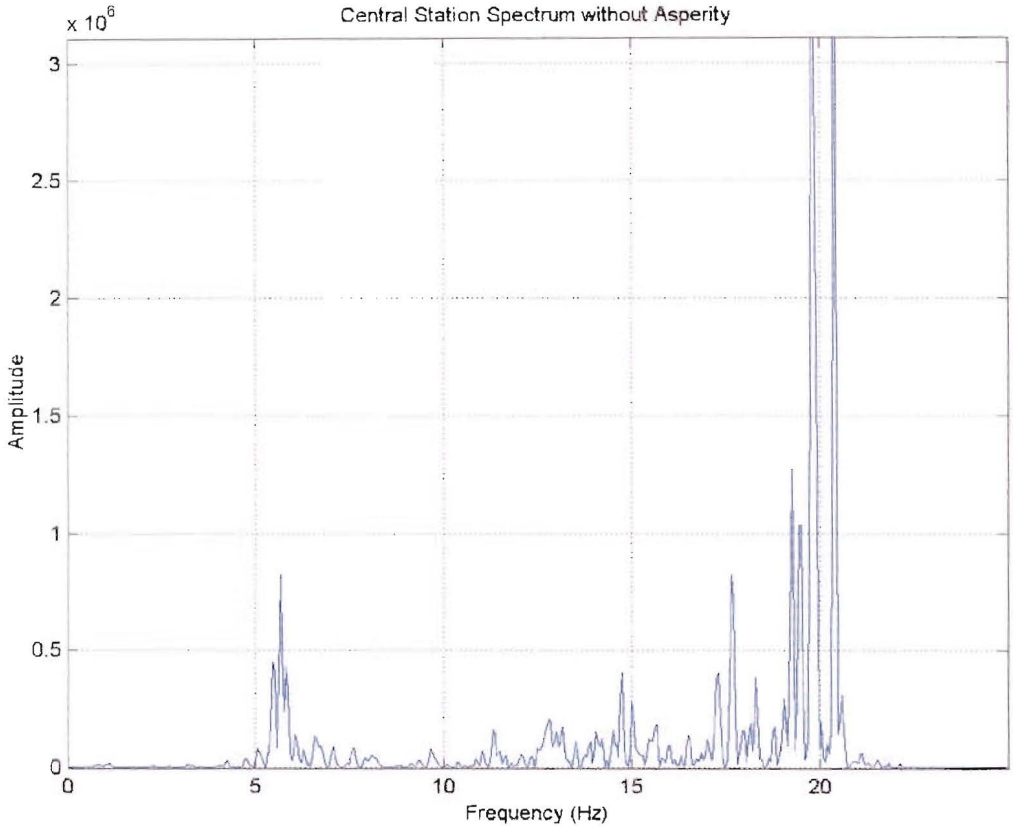

Figure 2B- 2: Fourier Acceleration Spectrum of the central station (scenario without asperity)

To remove the noise, the raw synthetic accelerograms are filtered applying a Butterworth filter from 0.5 hertz to 15 Hertz. Figure 2B- 3 shows the synthesized accelerogram at the central station of the Pylon Gully array after filtering. The maximum amplitude is now approximately 300 mg.

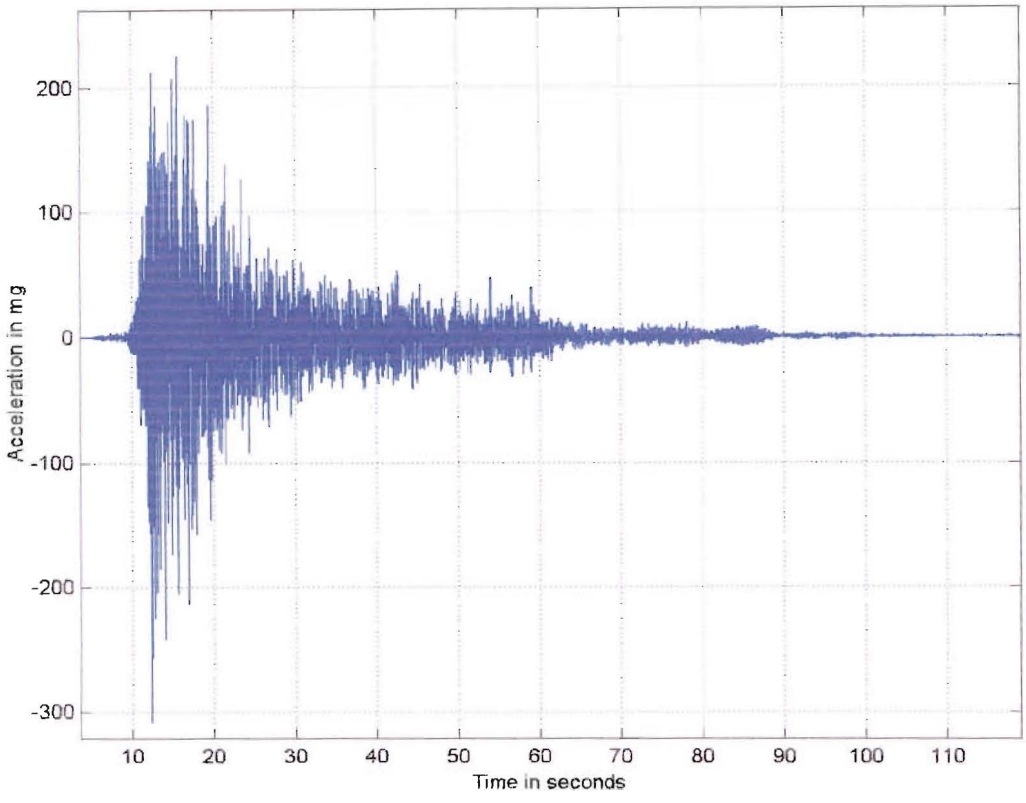

Figure 2B- 3: Accelerogram synthesized at the central station of the Pylon Gully array after filtering (scenario with no asperity)

Alignment of the accelerograms is an important part of the analysis. Preliminary tests on the original data sampled at 50 Hertz were proven to be significantly influenced by the accuracy of the alignment, as well as, by the velocity model. The initial velocity model used to generate the slowness maps, though only slightly too fast, had to be modified to better fit the data. In order to get a better resolution in the alignment process, the data had to be re-sampled at a higher rate. The sampling rate was originally 50 Hertz or one sample every 0.02 second. For a maximum station separation of 2 km, this sampling gave a slowness error of 0.01 s/km which was within the range of slowness values used in this case study. To avoid under-sampling, sampling rate was multiplied by 10. Re-sampling was done through a polynomial interpolation of data points as close as possible to the fixed original data points. A finer time sampling improves the precision of the alignment process. The alignment of the accelerograms for the vertical data was set at 9.08 seconds where the first P arrivals are detected (Figure 2B- 4).

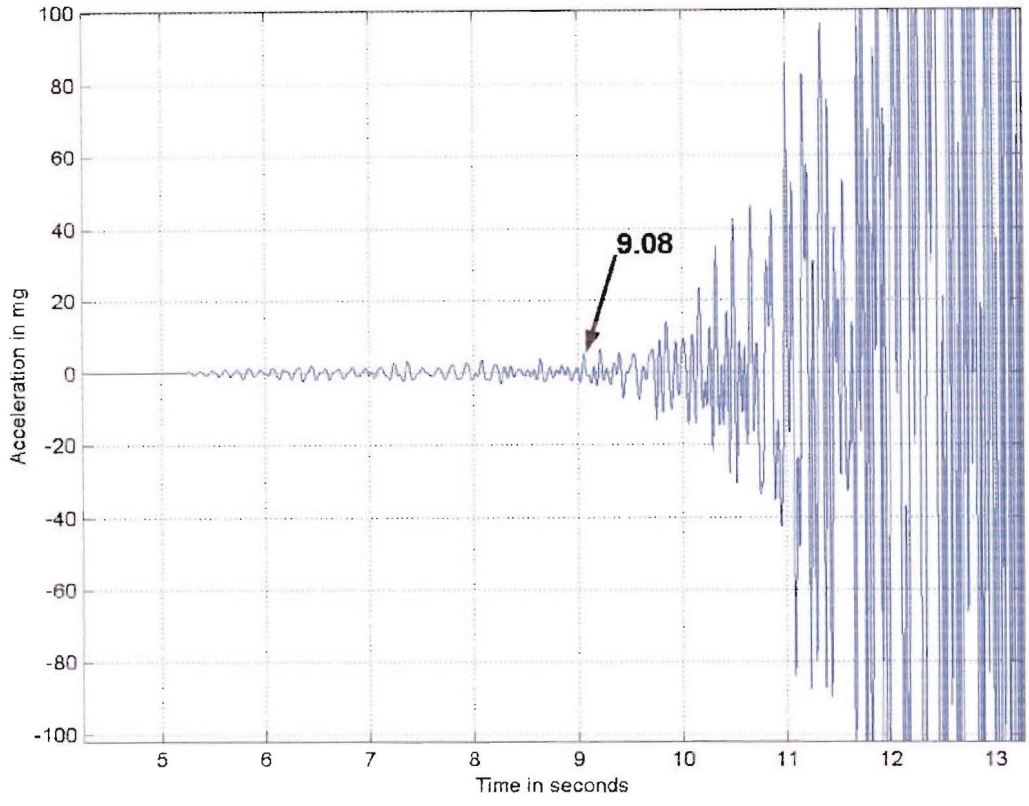

Figure 2B- 4: Phase chosen to perform the alignment for the vertical data (scenario with no asperity)

Alignment was performed applying a correlation method as well as manually. Shift times obtained from aligning the seismograms are presented in the following table. They range from 0 seconds up to 0.312 seconds for the station A2000 which is the furthest away from the central station.

Station	Shift times
A0	0
A100	0.018
A200	0.034
A300	0.038
A600	0.068
A1000	0.24
A2000	0.312
B100	0.032
B300	0.034
C200	-0.014
C500	-0.03
C1000	-0.098

Table 2B- 1: Shift times for the alignment of the vertical seismograms (scenario with no asperity)

By shifting the seismograms, the slowness spectra are translated by a constant vector. The slowness shift vector is computed in order to correct the slowness spectra. The vector is

determined applying the least mean square method to the shift times shown in Table 2B- 1. This vector also determines the direction of the first incoming source called the source azimuth. The shift components and azimuth of the slowness vector are:

- slowness shift along the X axis: 0.1300 s/km
- slowness shift along the Y axis: -0.094 s/km
- Azimuth: 54 degrees

The real components of the slowness shift vector are the slowness components of the hypocenter. The location of which is well known. They are determined using the slowness maps detailed in Chapter 2A. The hypocenter slowness parameters are:

- slowness shift along the X axis: 0.1438 s/km
- slowness shift along the Y axis: -0.1082 s/km
- Azimuth: 53 degrees

The computed results are very close to the expected values with the azimuths differing by only one degree. The computed slowness components are slightly lower than the real ones, which is likely due to an underestimated P-wave shifting time.

Having aligned the seismograms, one must determine the optimal time windows. In this case study, the QEE method is not employed to define the optimal time windows. The reason for which is in the program EMPSYN used to run the synthetics. EMPSYN generates the seismograms by creating evenly spaced point sources. In this application, the point sources are square areas of 0.2 km^2. Therefore there are no dominant patches of energy but regular incoming bursts of energy. The QEE method would not be relevant here. Instead it is assumed that each window, every 0.1 seconds, contains a signal. The 0.1 second value is defined considering a constant rupture velocity of 3 km/s and a source spacing of .45 km (the elemental areas are 0.2 km^2 which gives a side length of .45 km). Therefore sources occur every 0.15 seconds. Thus analysis of the seismograms every 0.1 seconds is conservative. The best time window widths are those which yield the highest resolution of the spectral matrix. Given that the array is located approximately 25 km away from the hypocenter, S waves are expected to arrive about 3 seconds later than the P waves. Once the S waves arrive, the signals become very noisy. Therefore the array analysis has been limited to up to the 12 second window. This constraint gives 3 seconds of study for the vertical data. Time windows and their respective widths computed applying the method of the optimum spectral matrix noted above are summarized up in Table 2B- 3.

The slowness spectra

Slowness spectra have been stacked for frequencies from 1 to 15 Hertz sampled every 0.1 Hertz. Times are given here with respect to the origin of the seismograms. Resulting slowness spectra for windows 9.1, 11 and 12 seconds are shown in Figure 2B- 5. Axes have been shifted according to the slowness shift values computed. The ellipses denoted by stars represent slowness vectors of known input sources rupturing at times labeled near the ellipses. Nonetheless, the ellipses are only indicative as the labeled rupture times do not take into account the travel time difference between sources (the differences are generally small however being less than half a second (Table 2B- 3)).

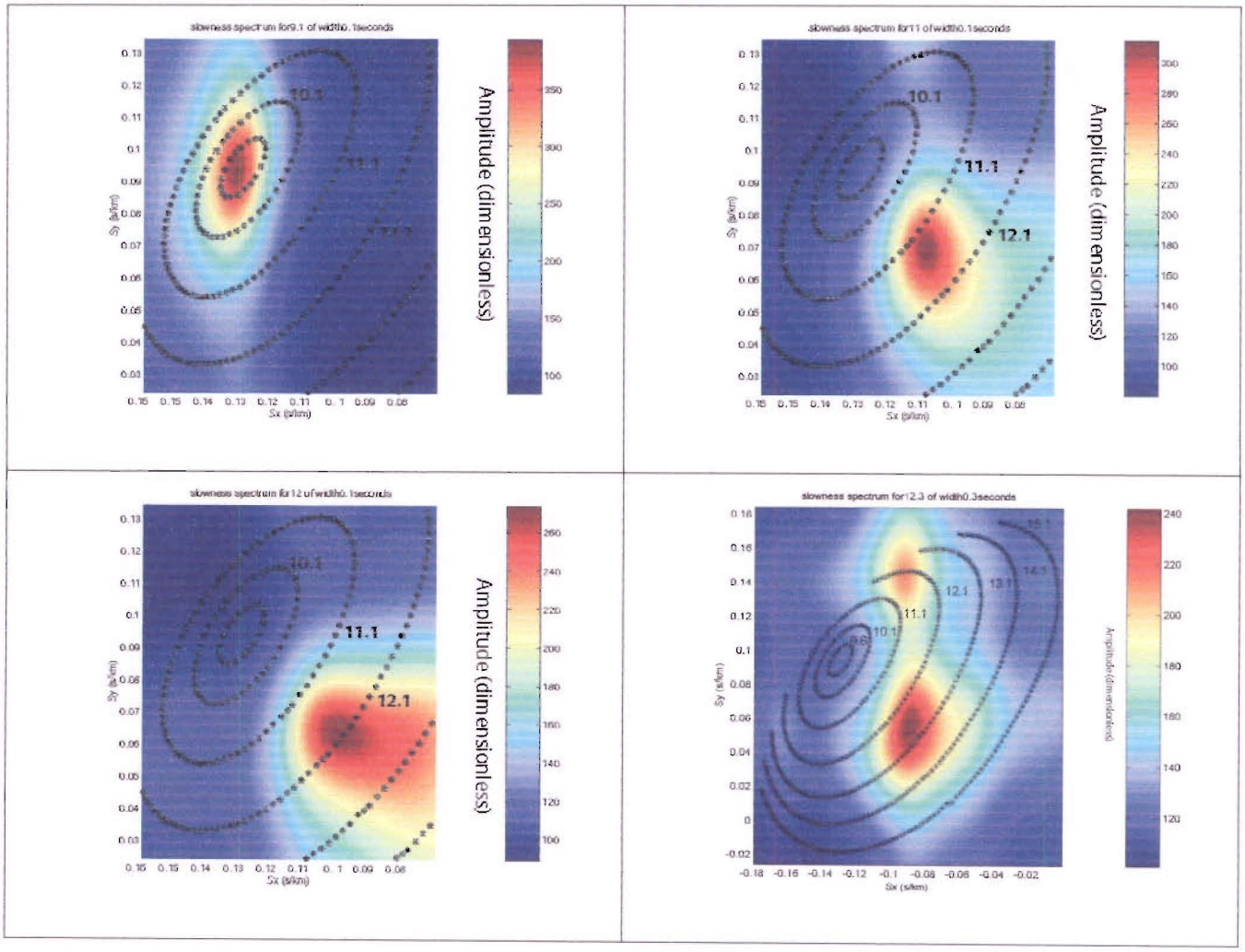

Figure 2B- 5: Slowness spectra computed at windows 9.1, 11, 12 and 12.3 seconds (scenario with no asperity)

The spectra are a good representation of the actual evolution of the rupture front. They present one sharp peak, with peak amplitudes then decreasing as time increases. In this array analysis it is assumed that only one source propagates at a time through the array. The peaks

represent a tip of the rupture front. As shown by the spectra, they propagate downwards in the south-east direction. The peak times are very close to the expected rupture times. When looking at spectra computed later than 12 seconds, a second spurious peak appears although only a single source was assumed for the analysis. This is a sign of the degradation and complexity of the signal most likely due to the arrivals of various other waves. All the spectra computed at every time window are provided in Appendix A.

1.2. Analysis and interpretation

From the slowness maps computed in Chapter 2A, each peak of the slowness spectra is assigned a location on the fault plane. For each location, a travel time is computed and subtracted from the time at which the slowness spectra have been computed. This new time is the computed rupture time. Figure 2B- 6 shows the fault diagram resulting from the projection of all the spectra from 9.1 to 12 seconds.

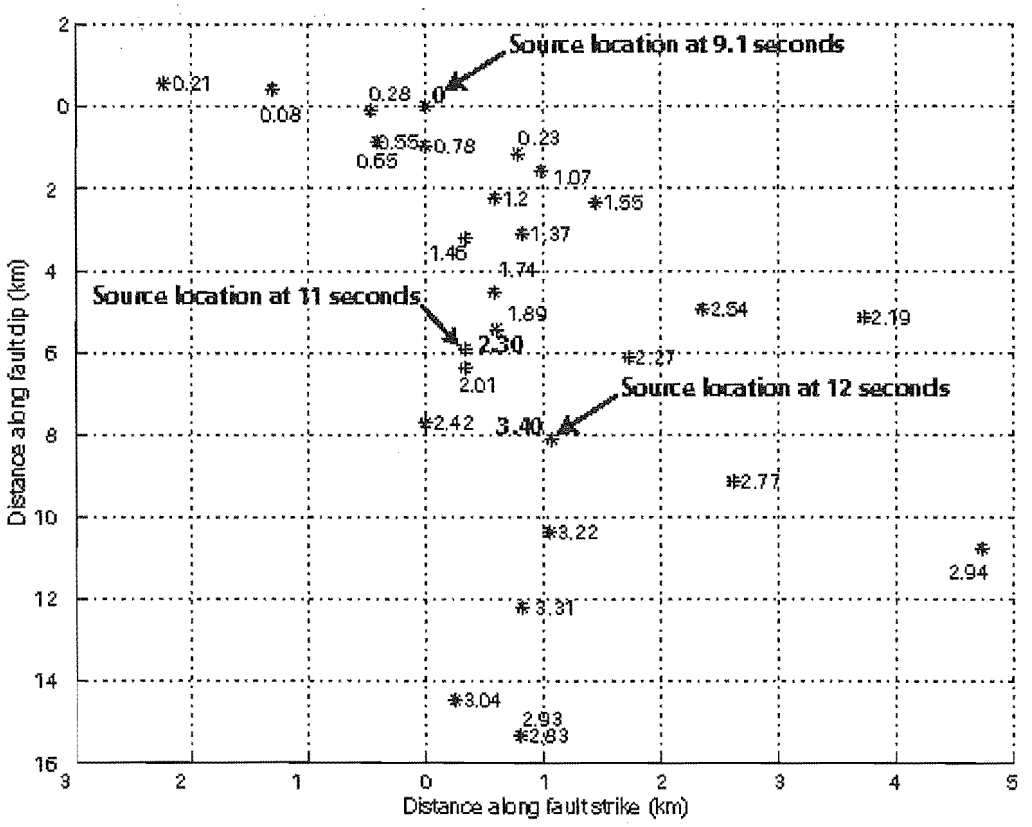

Figure 2B- 6: Fault diagram for the scenario with no asperity showing point locations and their respective computed rupture time

The overall direction trend of the rupture front is satisfying as the point sources gradually propagate away from the hypocenter. The prominent pattern is the tendency of the computed

rupture front to travel downwards at a 90 degree angle. A possible explanation to this downward direction trend could be the way the seismograms are synthesized. Given that the rigidity of the material increases with depth, and that deeper point sources get closer to the array, sources at depth are more energetic than superficial sources. The fault diagram shows that the extent of the rupture area is up to 15 km. This value is not the final rupture front location as computations are only performed on the first 3 seconds of the seismograms. Therefore one can not define the total rupture area from this case study. Rupture velocities computed at the times 9.1, 11 and 12 seconds are represented in Table 2B- 2.

	Distance (km)	**Time difference (seconds)**	**Rupture Velocity(km/s)**
9.1 to 11 seconds	5.92	2.30	2.5739
9.1 to 12 seconds	8.16	3.40	2.4
11 to 12 seconds	2.30	1.10	2.09

Table 2B- 2: Rupture parameters at 9.1, 11 and 12 seconds (scenario without asperity)

The rupture velocities computed above are satisfying, given that they are very close to the constant input rupture velocity of 3 km/second. However, the values are decreasing for increasing times, which is a sign of degradation of array analysis as the recordings become more complex. A visually attractive way to compare the results is to plot the computed rupture times against the expected rupture times (Figure 2B- 7). The graph shows that up to 11.1 seconds the difference in rupture times is small (approximately 0.5 seconds); past this, the difference grows disproportionably reaching a 2-second error.

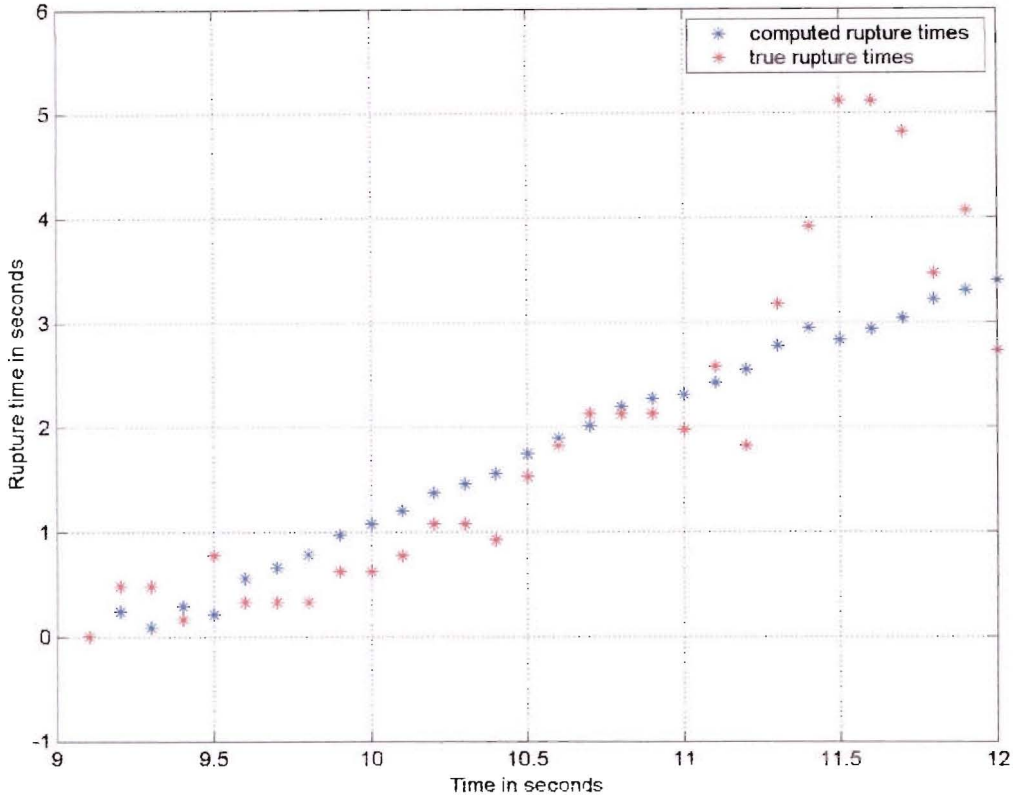

Figure 2B- 7: Computed rupture times against true rupture times (scenario with no asperity). The computed rupture times refer to the projected point sources; the true rupture times refer to the actual rupture times of the point sources generated by EMPSYN.

From Figure 2B- 7, the average rupture time error is 0.5342 seconds; the maximum error being 2.29 seconds at the 11.5 second window (2.83 second computed rupture time); the minimum error being 0 second at the 9.1 second window. The 10.6 and 10.8 second windows are very good with a small error of 0.07 seconds. Table 2B- 3 summarizes the rupture parameters obtained for the scenario without an asperity.

Central time (s)	Time width (s)	Lat	Lon	Depth (km)	Travel time (s)	X (km) position on fault (km)	Y(km) position on fault (km)	Inferred Rupture time (s)	True rupture time (s)	Rupture time error (s)
9.1	0.1	-42.90	171.48	9.93	4.98	0.00	0.00	0.00	0.00	0
9.2	0.3	-42.91	171.50	10.74	4.85	0.78	-1.14	0.23	0.47	0.2374
9.3	0.2	-42.91	171.47	9.62	5.10	-1.31	0.44	0.08	0.47	0.39
9.4	0.2	-42.91	171.48	10.01	5.00	-0.47	-0.11	0.28	0.16	0.12
9.5	0.1	-42.91	171.46	9.54	5.17	-2.24	0.55	0.21	0.77	0.56
9.6	0.2	-42.91	171.48	10.53	4.93	-0.41	-0.85	0.55	0.32	0.23
9.7	0.2	-42.91	171.48	10.53	4.93	-0.41	-0.85	0.65	0.32	0.33
9.8	0.2	-42.91	171.49	10.60	4.90	0.00	-0.95	0.78	0.32	0.46
9.9	0.1	-42.91	171.50	11.03	4.81	0.98	-1.56	0.97	0.62	0.35
10	0.3	-42.91	171.50	11.03	4.81	0.98	-1.56	1.07	0.62	0.45
10.1	0.2	-42.91	171.50	11.51	4.78	0.59	-2.23	1.20	0.77	0.43
10.2	0.1	-42.92	171.51	12.12	4.71	0.82	-3.10	1.37	1.07	0.3
10.3	0.3	-42.92	171.50	12.19	4.72	0.33	-3.19	1.46	1.07	0.39
10.4	0.2	-42.91	171.51	11.59	4.73	1.45	-2.34	1.55	0.92	0.63
10.5	0.2	-42.92	171.51	13.13	4.64	0.59	-4.53	1.74	1.52	0.22
10.6	0.2	-42.93	171.52	13.77	4.59	0.60	-5.43	1.89	1.82	0.07
10.7	0.2	-42.93	171.52	14.43	4.57	0.33	-6.36	2.01	2.12	0.11
10.8	0.1	-42.91	171.55	13.58	4.49	3.73	-5.16	2.19	2.12	0.07
10.9	0.3	-42.93	171.53	14.26	4.51	1.73	-6.13	2.27	2.12	0.15
11	0.1	-42.93	171.52	14.11	4.58	0.33	-5.91	2.30	1.97	0.33
11.1	0.1	-42.94	171.52	15.39	4.56	0.00	-7.72	2.42	2.57	0.15
11.2	0.1	-42.92	171.53	13.42	4.54	2.36	-4.93	2.54	1.82	0.72
11.3	0.1	-42.94	171.56	16.40	4.41	2.62	-9.14	2.77	3.17	0.4
11.4	0.2	-42.93	171.58	17.54	4.34	4.74	-10.76	2.94	3.92	0.98
11.5	0.2	-42.98	171.57	20.77	4.55	0.81	-15.32	2.83	5.12	2.29
11.6	0.3	-42.98	171.57	20.77	4.55	0.81	-15.32	2.93	5.12	2.19
11.7	0.3	-42.98	171.56	20.14	4.54	0.25	-14.45	3.04	4.82	1.78
11.8	0.2	-42.95	171.55	17.25	4.46	1.06	-10.36	3.22	3.47	0.25
11.9	0.2	-42.96	171.55	18.54	4.47	0.82	-12.18	3.31	4.07	0.76
12	0.1	-42.94	171.53	15.65	4.48	1.07	-8.09	3.40	2.72	0.68

Table 2B- 3: Rupture point details (scenario without asperity)

The analysis of synthetic data for a known rupture scenario has shown that dense array analysis is efficient. Dense array analysis has proven to be capable of determining accurately the rupture velocities and directions. This analysis shows that as time increases, and the signal become more complex, dense array efficiency decreases especially as the arrival of S waves. Moreover, the seismogram alignment and the velocity model must be determined carefully to allow an accurate resolution of rupture parameters.

2 Scenario with asperity

Dense array analysis is now applied to a unilateral fault rupture scenario with an added asperity. The objective is to study the efficiency of the technique in detecting the presence of the asperity. The asperity is a Hartzell model which begins to rupture as the rupture front propagates through it. The asperity location has been chosen to leave enough time for the rupture front to propagate on its own before reaching the asperity, as well as to be close enough to the hypocenter to record the asperity before the arrivals of the S wave. More details on the asperity model in EMPSYN can be found in Chapter 2 A. The fault/asperity configuration is summarized in Figure 2B- 8.

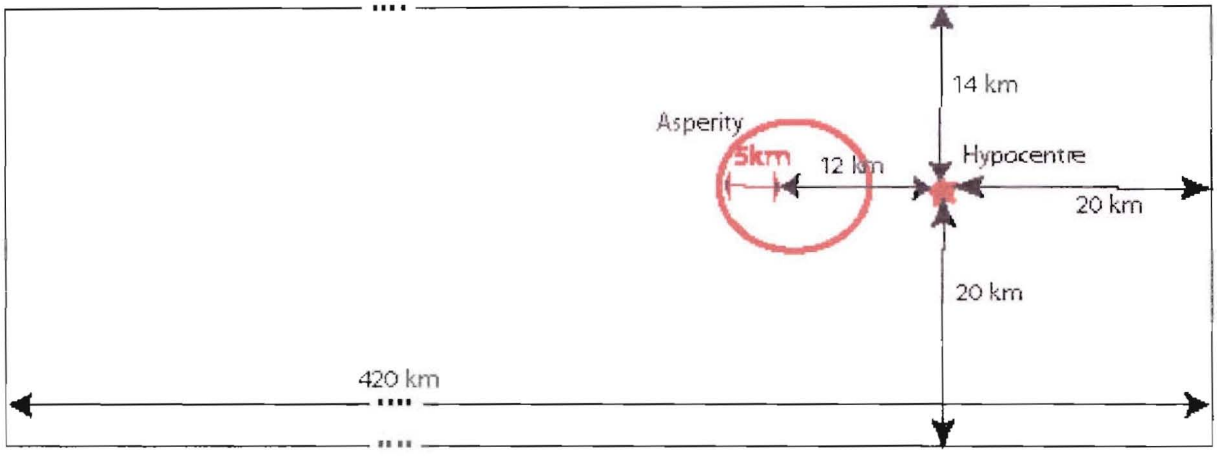

Figure 2B- 8: Fault and asperity geometry

2.1. Results

The synthetics

Figure 2B- 9 shows the raw synthetic accelerograms obtained at three stations of the Pylon Gully array (Central, A2000 and C1000 stations). The major characteristic is the presence of high amplitude low frequency noise at the head and tail of the recordings for some stations. These low frequency signals are not caused by the asperity as they occur even before the rupture front starts, as well as, after the rupture front passed the asperity. Also, the long period noise does not appear on the synthetics generated for the same scenario without the asperity. Therefore this particular noise must be due to a computational artifact.

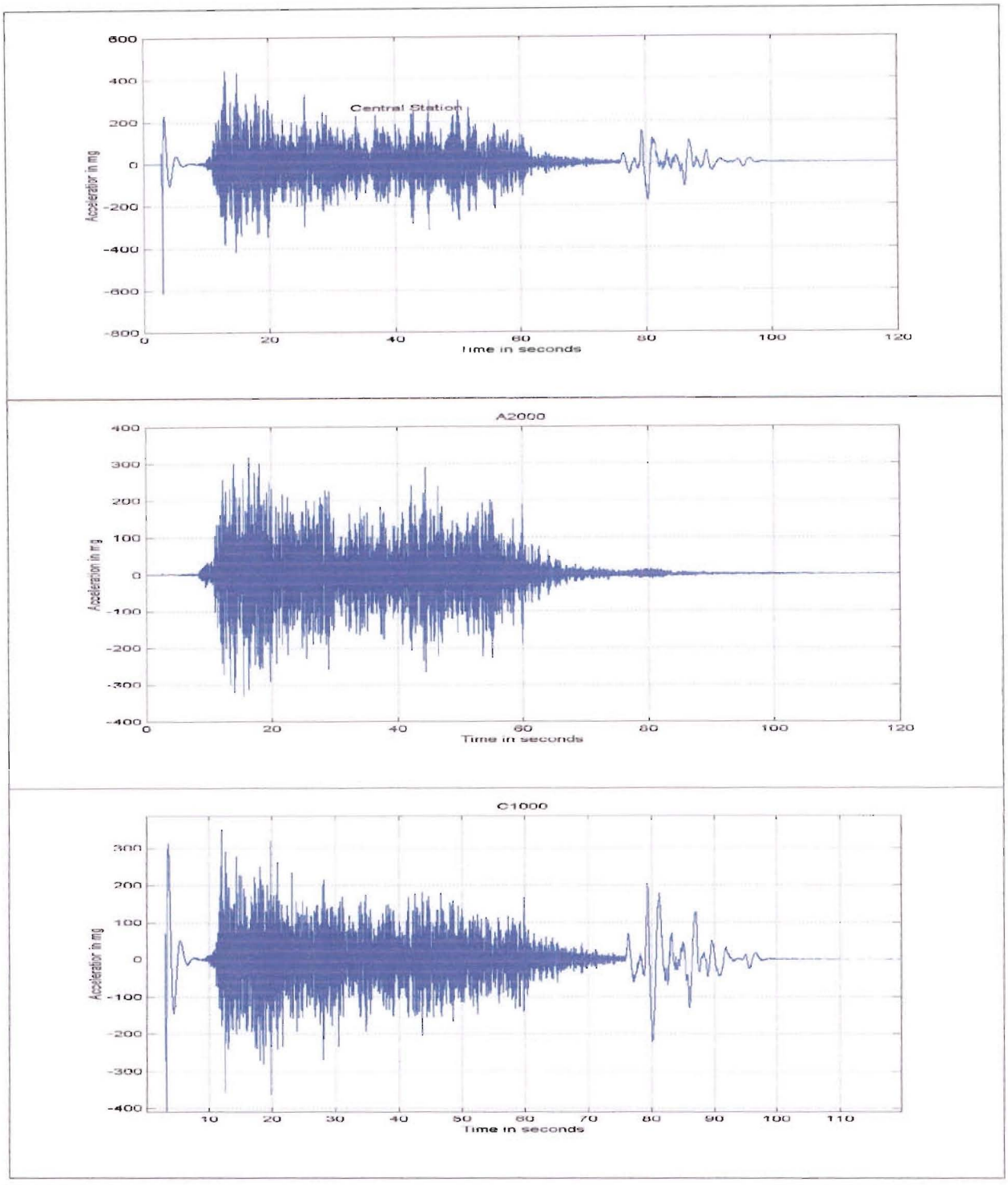

Figure 2B- 9: Raw accelerograms synthesized at the central station of the Pylon Gully array, Station C1000 and the central station show the presence of a long period noise (scenario with an asperity)

This low frequency noise appears clearly in the Fourier acceleration spectrum of the central station in Figure 2B- 10. Where the Fourier spectrum of the scenario without the asperity presents a flat response for low frequencies, the Fourier spectrum here shows a peak at 1 Hertz.

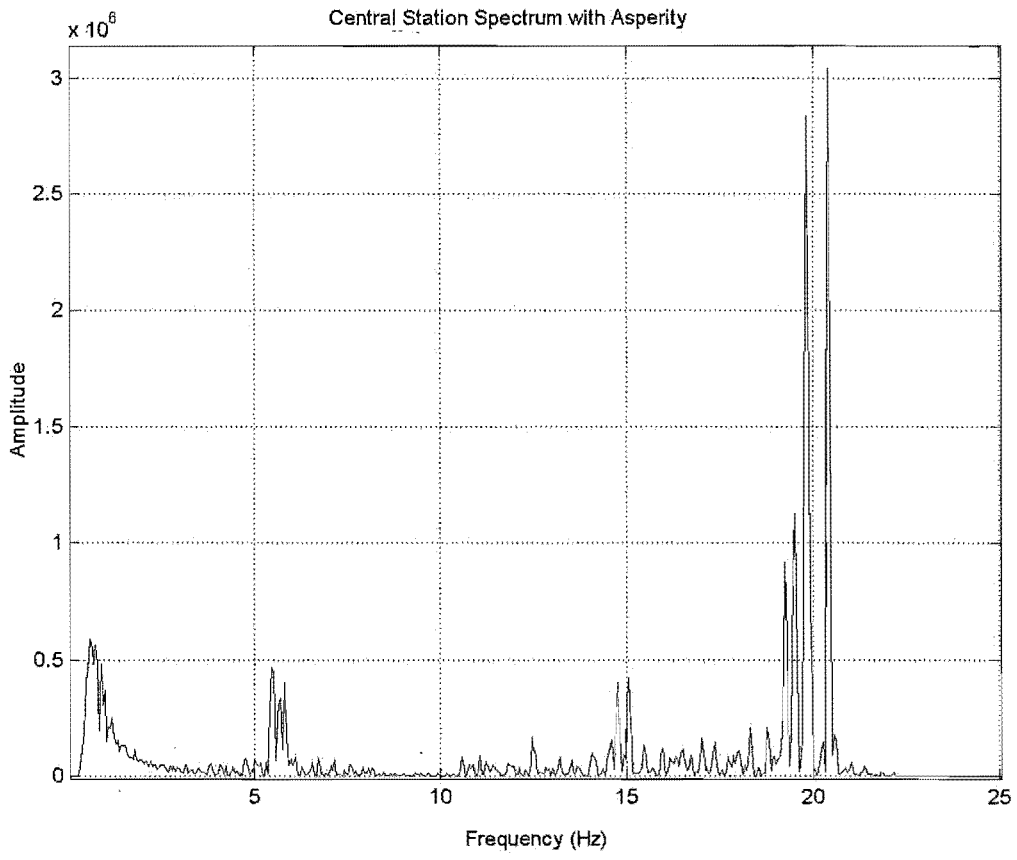

Figure 2B- 10: Fourier acceleration spectrum (scenario with asperity)

The synthetic accelerograms are filtered applying a Butterworth filter from 1 hertz to 15 Hertz. The upper frequency of 15 hertz was chosen to filter out noise that appear after 15 Hertz for the same reasons as in the first scenario. Figure 2B- 11 shows the synthesized accelerogram at the Pylon Gully central station after filtering. The maximum amplitude is about 150 mg. The spurious peak at the beginning of the seismogram is still present but attenuated. To remove the peak completely, the signal should be filtered at 5 Hertz. This however may filter out some real signals. Also, such a strong filtering is not necessary given the long period noise is not present in the part of the signal to be studied. Therefore the filter is kept at 1 Hertz.

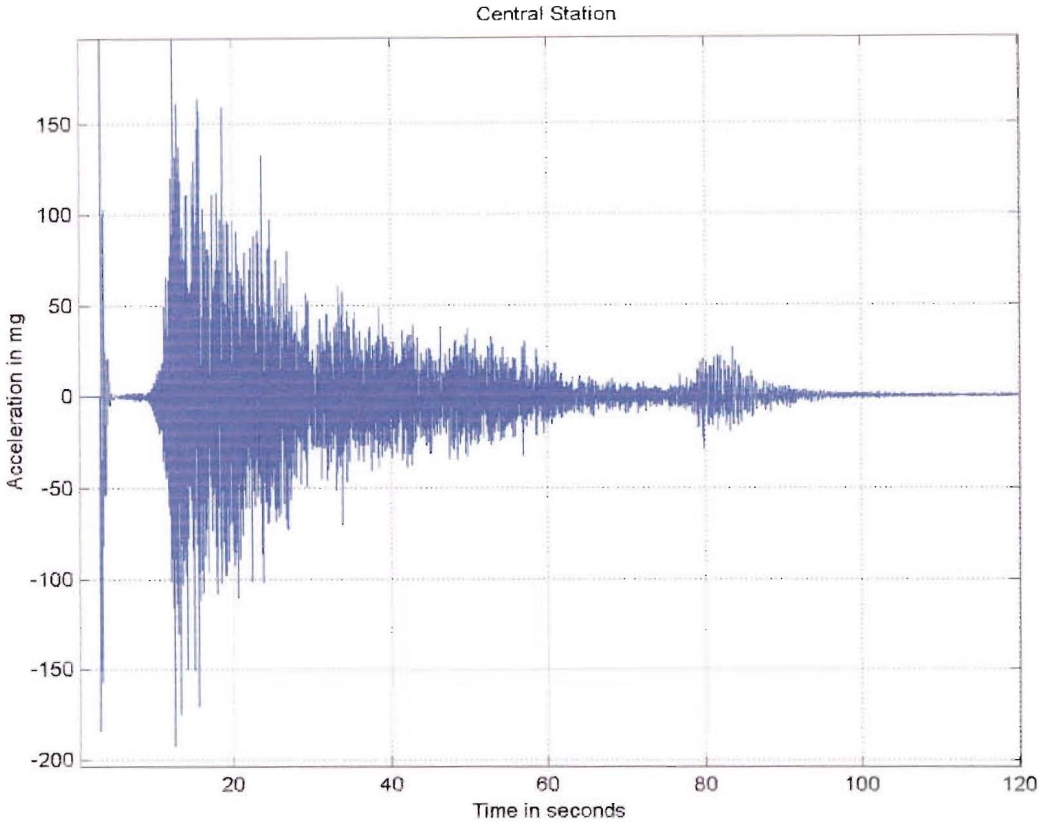

Figure 2B- 11: Accelerogram synthesized at the central station of the Pylon Gully array after filtering (Scenario with asperity)

Having filtered the seismograms, the next step is the alignment of the accelerograms. As for the first scenario, the recordings are re-sampled by a factor of 10, thus allowing a greater precision for the seismogram alignment. The first P wave arrival is also chosen at 9.08 seconds (Figure 2B- 12).

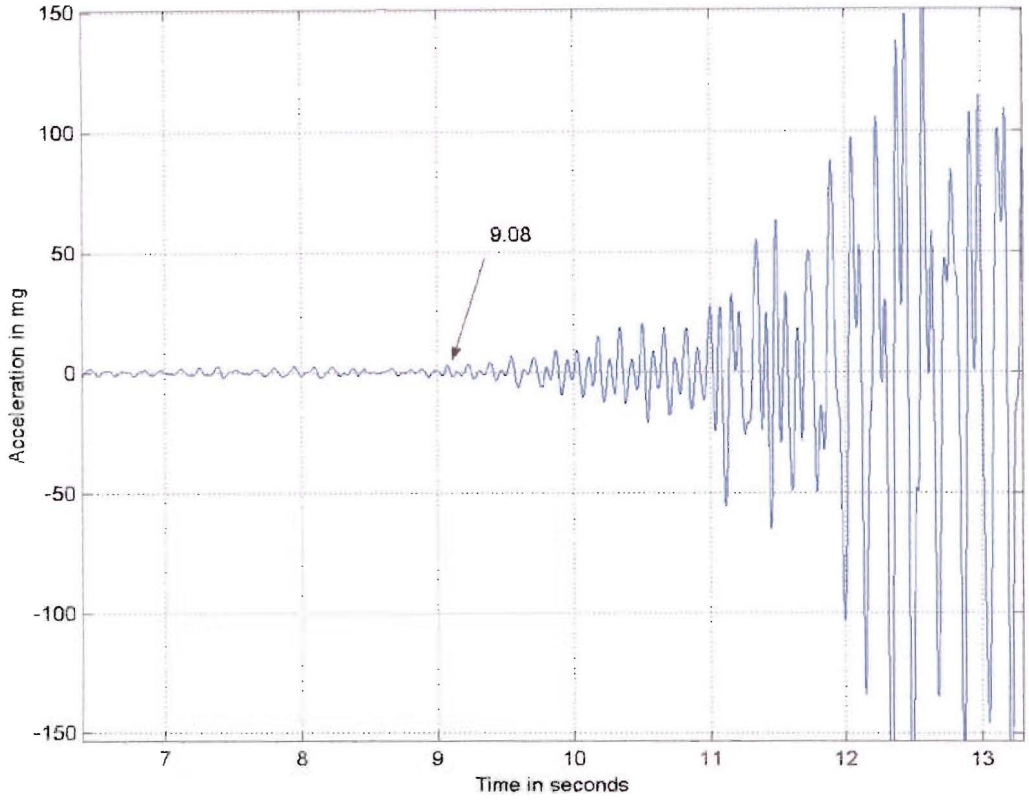

Figure 2B- 12: Phase chosen to perform the alignment for the vertical data

Shift times determined from aligning the seismograms are presented in Table 2B- 4. They range from 0 to 0.525 seconds. These values are higher than the ones obtained for the previous scenario. Given that the geology model, the Green's functions and the hypocentral locations are identical for both rupture scenarios, the difference in time picking can only be explained by the subjective choice of determining the first arrivals.

Station	Shift times
A0	0
A100	0.012
A200	0.028
A300	0.034
A600	0.065
A1000	0.235
A2000	0.525
B100	0.028
B300	0.034
C200	-0.006
C500	-0.032
C1000	-0.096

Table 2B- 4: Shift times for the alignment of the vertical seismograms

The slowness shift components obtained from the shift times using the least square method are:

- slowness shift along the X axis: 0.1587 s/km
- slowness shift along the Y axis: -0.1042 s/km
- Azimuth: 56.7 degrees

These results are closer to the expected values from the input model than the ones obtained for the scenario without the asperity. This is consistent with the conclusion that shift times for the previous scenario were underestimated.

The optimal time window width is computed using the spectral matrix amplitude method described in the previous section. Times are given here with respect to the origin of the seismograms. Time window widths are computed every 0.1 seconds from 9.1 seconds to 12 seconds. The analysis is restricted to 12 seconds as for the first scenario. Limiting the analysis to the first 3 seconds of the accelerograms does not affect the study of the asperity. Indeed, given that the asperity is located 12 km away from the hypocenter, and that it is circular of 5 km radius, the first asperity point source to rupture is located 7 km away. Therefore, considering a constant rupture velocity of 3 km/s, the first asperity point ruptures about 2.3 seconds later than origin time. A sign of the asperity should be noticed at approximately 11.4 second or 2.3 seconds after the first P arrival. The resulting time windows and their respective widths are summarized in Table 2B- 6.

The slowness spectra

As for the previous scenario, slowness spectra are stacked for frequencies from 1 to 15 Hertz every 0.1 Hertz. Slowness spectra computed at 9.1, 11 and 12 seconds are shown in Figure 2B- 13. All the spectra computed at every time window are provided in Appendix A. The spectrum at 9.1 seconds represents the expected pattern of a central contour peak. The 11 and 12 second peak spectra have the respective fault projection coordinates: (3.24, -7.49)km, (2.62, -9.14)km.

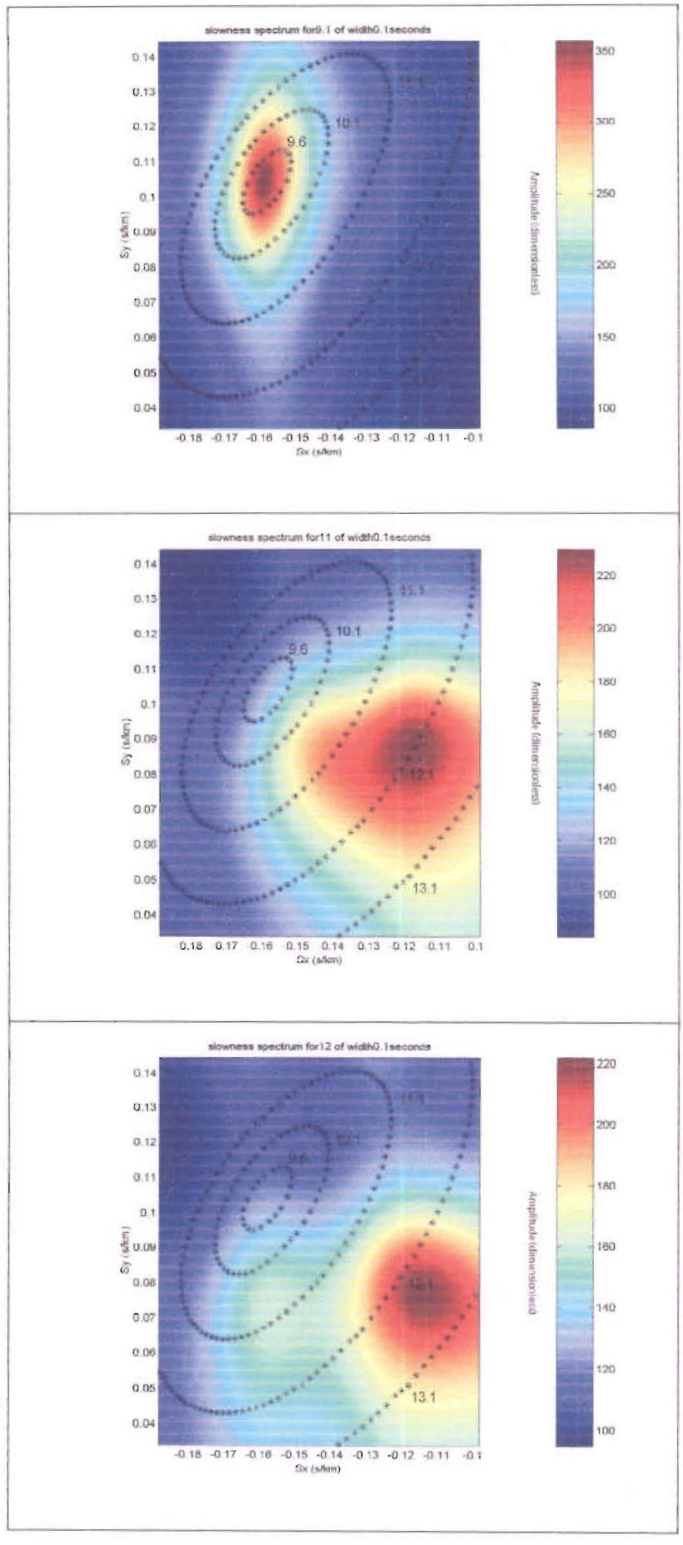

Figure 2B- 13: Slowness spectra computed at windows 9.1, 11 and 12 seconds (scenario with asperity)

2.2. Analysis and interpretation

By removing the travel time, one finds that the source at 12 seconds actually ruptures at 3.48 seconds, and the source at 11 seconds at 2.47 seconds. These results are consistent with the

source at 12 seconds being deeper than the one at 11 seconds. Given that they are located 2.12 km away from each others, the rupture velocity between these sources is approximately 2.09 km/s. This result is identical as the one obtained for the scenario without the asperity. Rupture locations and velocities computed at 9.1, 11 and 12 seconds are summarized in Table 2B- 5.

	Distance (km)	**Time difference (seconds)**	**Rupture Velocity (km/s)**
9.1 to 11 seconds	8.16	2.47	3.30
9.1 to 12 seconds	9.50	3.48	2.72
11 to 12 seconds	2.12	1.01	2.09

Table 2B- 5: Rupture parameters at 9.1, 11 and 12 seconds (scenario with asperity)

When looking at the three specific point sources mentioned above, there is no sign of an asperity. The rupture follows the same trend as for the scenario without the asperity. Should an asperity signature on the spectra occur, one would expect it between 11 and 12 seconds as explained previously. The following fault diagram in Figure 2B- 14 summarizes the point source rupture times and locations computed from 9.1 to 12 seconds every 0.1 seconds. Point sources impending on the array between 11 and 12 seconds are in bold. They are also labeled by their recording times instead of the usual rupture times to facilitate the study.

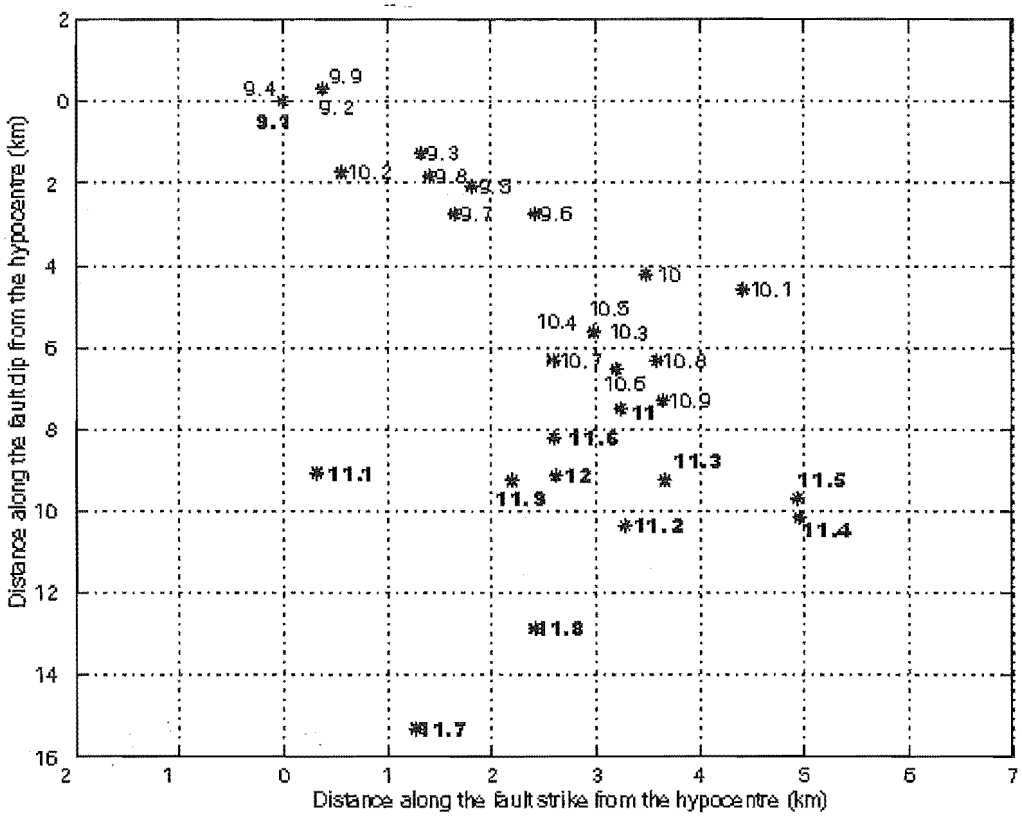

Figure 2B- 14: Fault diagram (Scenario with asperity): point sources are labeled with their respective recording time; point sources in bold correspond to recording time comprised between 11 and 12 seconds.

Point sources recorded between 11 and 12 seconds are expected to show the presence of the asperity (Figure 2B- 14). They are expected to be located further west on the fault than previous points: 7 km away from the hypocenter. On the contrary however these points are found to follow the downwards rupture trend without being influenced by the asperity. One can then ask if the asperity could be noticed through the analysis of computed rupture times against expected rupture times? This analysis is presented in Figure 2B- 15.

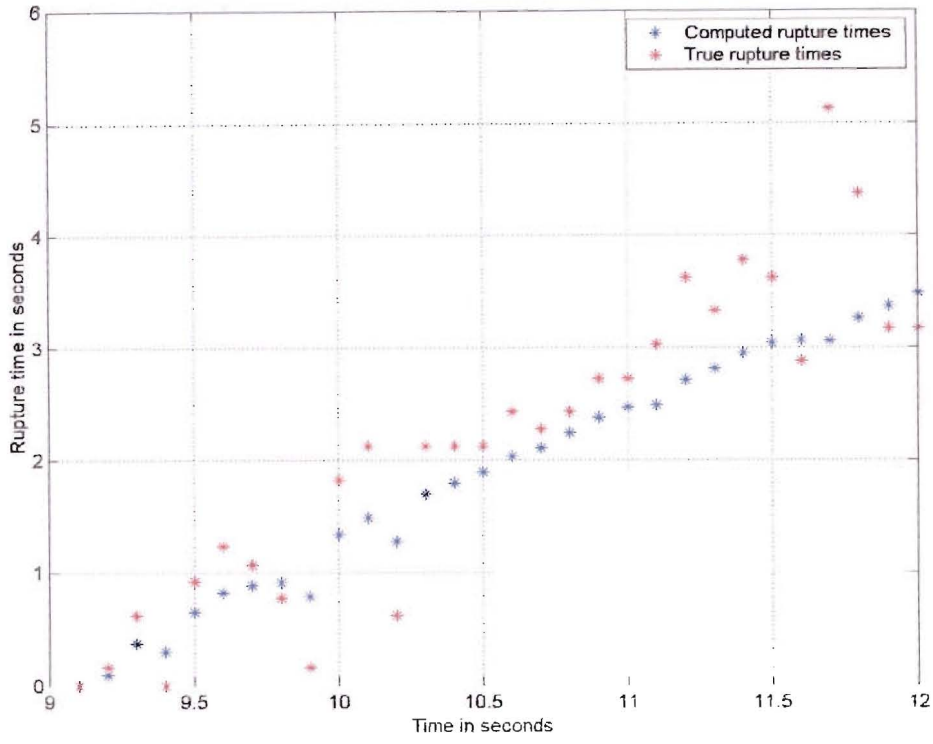

Figure 2B- 15: Computed rupture times against true rupture time for the scenario with asperity. The computed rupture times refer to the projected point sources; the true rupture times refer to the actual rupture times of the point sources generated EMPSYN.

When comparing Figure 2B- 15 to Figure 2B- 7 representing computed rupture times against expected rupture times for a scenario without asperity two distinctive features appear. The first one is that the computed rupture times for the scenario with the asperity also shows a dispersion from 11.2 seconds on. This dispersion is explained by the degradation and complexity of the signal as time passes. The second feature is a dispersion in the results from 9.9 to 10.3 seconds for the scenario with the asperity, that does not occur for the scenario without the asperity. Considering that the only difference in the scenarios is the inclusion of an asperity, this dispersion at approximately 10 seconds could be a degradation of the analysis due to a secondary signal coming in. However, given that waves from the asperity should arrive only 2.3 seconds after the first arrival, this hypothesis implies that the picking of the first arrival has not been done carefully and that the first arrival happened earlier than 9.08 seconds. Considering that the picking is rigorous and consistent for both scenarios, the hypothesis of a dispersion of the signal approximately 10 second being caused by the asperity is not realistic. The dispersion may therefore be explained simply through errors in the computation due to noise in the signals and bad window width computations. In conclusion, dense array analysis has not been able to detect the presence of the asperity using synthetics

generated using EMPSYN for this particular rupture scenario. This failure may be explained by the poor quality of the Green's functions used in this study. Therefore, it would be worth putting out some broadband seismographs at potential sites for future studies. The rupture parameters obtained from the analysis are listed in Table 2B- 6.

Central time (s)	Time width (s)	Lat	Lon	Depth (km)	Travel time (s)	X (km) position on fault (km)	Y(km) position on fault (km)	Inferred Rupture time (s)	True rupture time (s)	Rupture time error (s)
9.1	0.1	-42.90	171.48	9.93	4.98	0.00	0.00	0.00	0.00	0.00
9.2	0.1	-42.90	171.49	9.72	4.99	0.38	0.30	0.09	0.16	-0.07
9.3	0.3	-42.90	171.50	10.84	4.81	1.33	-1.28	0.37	0.62	-0.25
9.4	0.1	-42.90	171.48	9.93	4.98	0.00	0.00	0.30	0.00	0.30
9.5	0.3	-42.90	171.51	11.40	4.73	1.82	-2.07	0.65	0.92	-0.27
9.6	0.1	-42.91	171.52	11.88	4.67	2.42	-2.75	0.82	1.23	-0.41
9.7	0.4	-42.91	171.51	11.88	4.69	1.65	-2.75	0.89	1.07	-0.18
9.8	0.3	-42.91	171.51	11.22	4.77	1.41	-1.83	0.92	0.77	0.15
9.9	0.1	-42.90	171.49	9.72	4.99	0.38	0.30	0.79	0.16	0.63
10	0.2	-42.91	171.54	12.91	4.54	3.49	-4.21	1.34	1.82	-0.48
10.1	0.1	-42.90	171.55	13.17	4.50	4.42	-4.59	1.48	2.12	-0.64
10.2	0.1	-42.91	171.50	11.17	4.81	0.57	-1.75	1.27	0.62	0.65
10.3	0.2	-42.92	171.54	13.91	4.49	2.98	-5.63	1.69	2.12	-0.43
10.4	0.4	-42.92	171.54	13.91	4.49	2.98	-5.63	1.79	2.12	-0.33
10.5	0.2	-42.92	171.54	13.91	4.49	2.98	-5.63	1.89	2.12	-0.23
10.6	0.2	-42.92	171.55	14.54	4.45	3.20	-6.52	2.03	2.42	-0.39
10.7	0.1	-42.92	171.54	14.39	4.48	2.59	-6.30	2.11	2.27	-0.16
10.8	0.2	-42.92	171.55	14.40	4.45	3.59	-6.32	2.24	2.42	-0.18
10.9	0.1	-42.92	171.56	15.10	4.41	3.65	-7.31	2.37	2.72	-0.35
11	0.1	-42.93	171.55	15.23	4.42	3.24	-7.49	2.47	2.72	-0.25
11.1	0.2	-42.95	171.53	16.34	4.50	0.32	-9.06	2.48	3.02	-0.54
11.2	0.3	-42.94	171.57	17.25	4.38	3.28	-10.35	2.71	3.62	-0.91
11.3	0.1	-42.93	171.57	16.48	4.37	3.67	-9.26	2.81	3.32	-0.51
11.4	0.2	-42.93	171.58	17.12	4.34	4.95	-10.17	2.94	3.77	-0.83
11.5	0.1	-42.93	171.58	16.77	4.34	4.93	-9.68	3.04	3.62	-0.58
11.6	0.1	-42.93	171.55	15.74	4.42	2.60	-8.21	3.06	2.87	0.19
11.7	0.1	-42.98	171.57	20.74	4.53	1.28	-15.29	3.06	5.12	-2.06
11.8	0.2	-42.96	171.57	19.04	4.42	2.41	-12.88	3.26	4.37	-1.11
11.9	0.1	-42.94	171.55	16.48	4.42	2.19	-9.26	3.36	3.17	0.19
12	0.1	-42.94	171.56	16.40	4.41	2.62	-9.14	3.48	3.17	0.31

Table 2B- 6: Rupture point details for the scenario with no asperity

D Conclusion

The application of dense array analysis to synthetic strong motion data has proven that the technique is efficient in studying gross fault rupture parameters. The analysis provides rupture velocities and directions consistent with input values. It is an important outcome to validate dense array analysis performed on real data sets. Being able to compare computed parameters with their known input values has emphasized the importance of the velocity model in the projection of the slowness spectra, the importance of timing accuracy and high data sampling of the recording, as well as, the importance of the array location from the hypocenter.

By choosing a location 25 km away from the hypocenter, fault sources are finely resolved, though the analysis of the P waves is limited to the first 3 seconds of the recordings. Therefore, a future dense array location in the region of interest should be located further away from the Alpine Fault than Pylon Gully. A distance 40 km away from the hypocenter would be an ideal starting point for a site search.

The significance of timing has a consequence on the choice of instruments to compose the array. Instruments with a high sampling rate are essential. This study has not been able to analyze the horizontal data set due to the lack of consistent seismogram alignments. Therefore, dense array instruments should provide excellent 3-component recordings.

Unexpectedly, dense array analysis of the rupture scenario with an asperity revealed no sign of an asperity. This comes as a surprise considering the promising results dense array analysis had provided previously in other respects. An explanation could be high noise and complexity in the recordings, or the signal of the asperity being weaker than the main rupture front signal. Future studies using a range of synthetic programs with various asperity models would be interesting to fully test the method.

Chapter 3 - Direct measurements of a Fault rupture using the SMART-1 dense array

A Presentation of the SMART-1 array and Event 5

The SMART-1 array (Bolt et al., 1982) was a near ideal dense array of strong-motion instruments located in Taiwan. The location, configuration and performance of this array are detailed in the following paragraphs. This is followed by the introduction of one of the major earthquakes recorded at SMART-1: Event 5. Event 5 is reprocessed applying dense array analysis and parameters relevant to this study are presented. Given that this event has been widely studied under various array analyses, conclusions of these previous array studies are summarized.

1 The Smart-1 array

1.1. Location and configuration

The SMART-1 array was located in the Northeast corner of Taiwan, near the city of Lotung (see Figure 3A- 1). The array which operated from 1980 to 1991 was designed under the cooperation of the University of California in Berkeley and the Institute of Earth Sciences in Taipei.

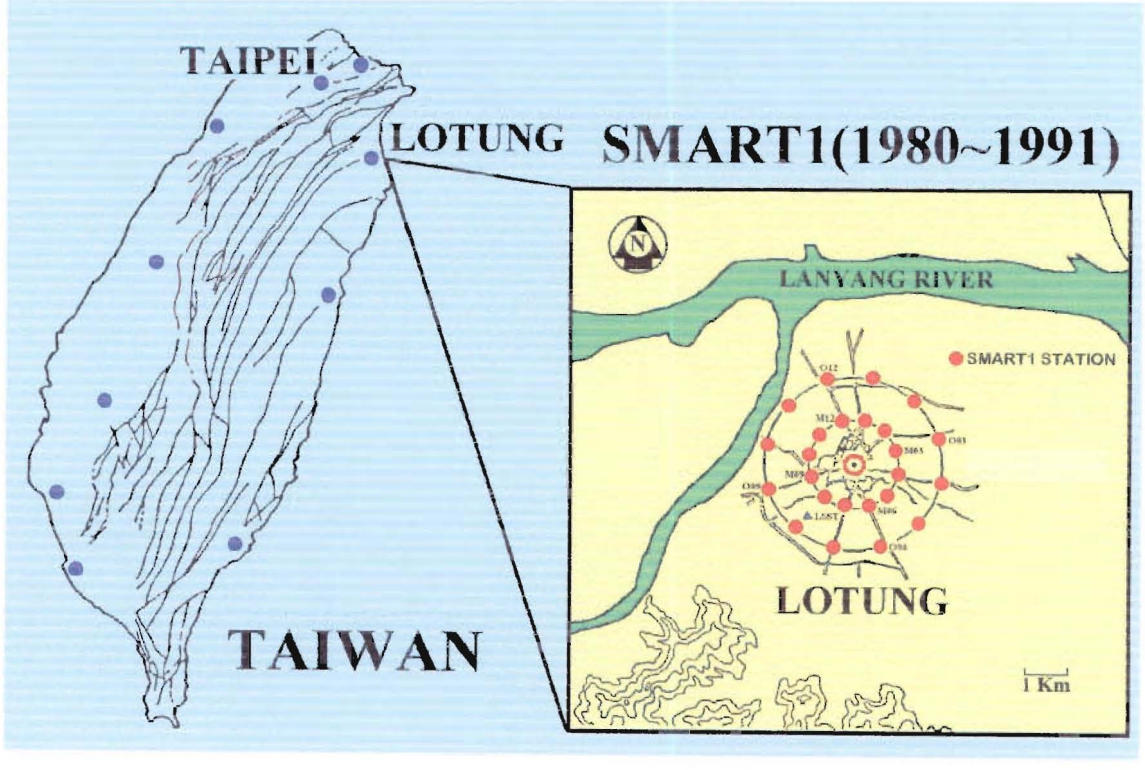

Figure 3A- 1: Location of the SMART-1 array in Taiwan

SMART-1 was composed of 36 stations set up into 3 concentric circles of radii 200m, 1000 m and 2000m around a central station. Each ring contains 12 equi-spaced instruments shown in Figures 3A-1 and 3A-2.

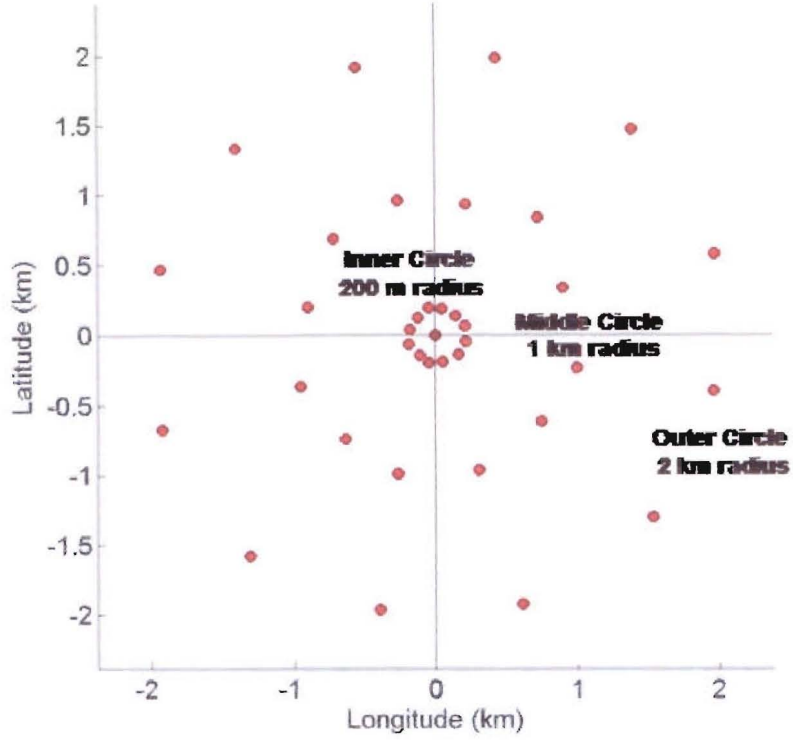

Figure 3A- 2: Configuration of the SMART-1 array

1.2. Purpose

During its ten years of service SMART-1 recorded over 60 earthquakes. Its purpose was to record the near-field ground motion of very large earthquakes for the engineering and seismological study of strong motion events.

1.3. Performance

The SMART-1 array recorded a large range of earthquakes with epicentral distances varying from 3 to 200 km, and depths up to 100 km. Although site effects were significant (refer Chapter 1-C), it has provided high quality digital recordings that have been intensely studied. For example Event 5, recorded in January 1981 has been widely studied applying array analysis methods (Abrahamson 1985, Darragh 1987, Goldstein 1988, Goldstein et al. 1991).

To estimate the array characteristics of SMART-1, a 2-d spatial frequency transfer function specific to the array configuration is computed. The 2-d transfer function shown in Figure 3A-3 assumes for Event 5 that the array is composed of the 27 operational stations. A transfer function shows the efficiency of the array in terms of the range of wavelengths that can be described by the array. The highest wavenumber that can be studied depends on the minimum separation between two captors. In this case, the smallest distance is 200 m. The requirement for two samples per wavelength gives a minimum wavelength λ of 400 m resulting in a maximum wavenumber of $\frac{2\pi}{\lambda} = 15.7 km^{-1}$.

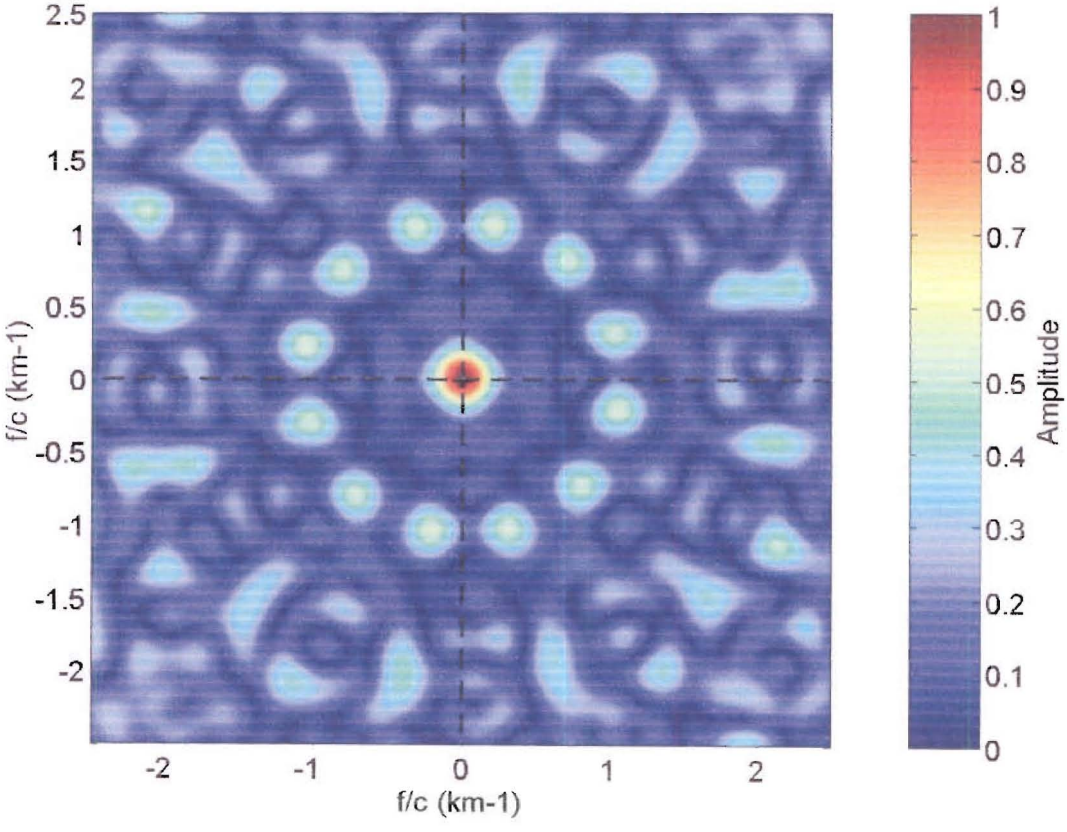

Figure 3A- 3: Transfer function of the Smart-1 array (27 stations)

The transfer function does not show any secondary peak in the range of the wavenumbers of interest. Also the central lobe is very narrow (only a grid-unit wide). This indicates that SMART-1 has a high signal resolution. The optimal configuration of SMART-1 and its ideal location in a highly seismic area makes it an ideal source of high quality data for dense array analysis.

2 Event 5

2.1. Why re-study Event 5?

Event 5, a magnitude 5.9 earthquake, occurred on January 29th, 1981. The epicentre was located 24 25.75N 121 53.78E approximately 30 km southeast of Lotung (Figure 3A- 4). Further information on Event 5 can be found on:

http://www.earth.sinica.edu.tw/~smdmc/smart1/event/event5.htm

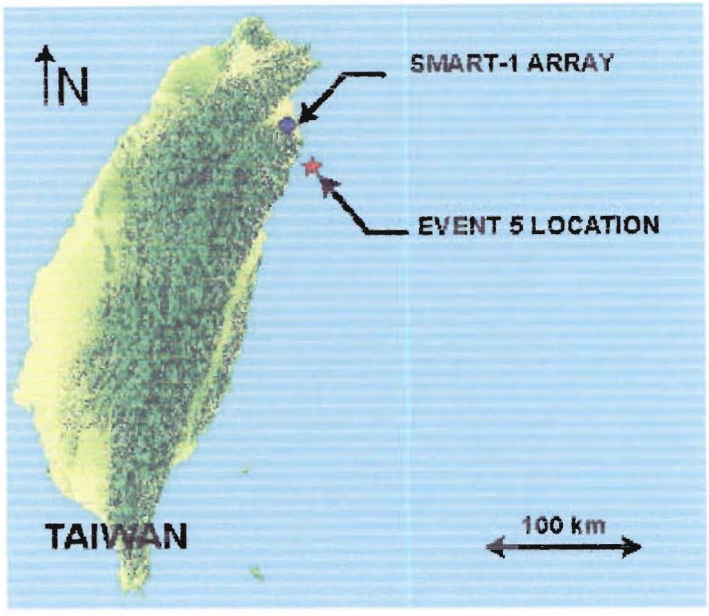

Figure 3A- 4: Event 5 epicentre location

Reasons that make Event 5 suitable to study with array analysis include:

- Event 5 was a high magnitude event.
- The event triggered almost all the stations at SMART-1.
- The range of azimuth for the source is large enough to be detected with array analysis.

Event 5 has been widely studied with different conclusions suggested for the mechanism of the fault rupture. The objective of this new study is to assess the application of dense array analysis and compare the results to those obtained from precious studies.

2.2. Rupture parameters

Following studies by Academia Sinica in Taiwan, the focal mechanism characteristics are as follows (http://www.earth.sinica.edu.tw/~smdmc/smart1/event/event5.htm):

- Strike: 91 deg.
- Dip: 38 deg.
- Slip: -3 deg.

The values for fault strike and dip shown are consistent with those published in previous studies (Abrahamson 1985, Darragh 1987, Goldstein 1988, Goldstein et al. 1991), such as 109 degree strike and 60 degree dip (Goldstein et al., 1991). However, previous studies suggest that the Event 5 slip angle is 64 degrees which differs to the value specified by Academia Sinica. Given that array analysis follows only the propagation of the tip of a rupture front, the rupture direction does not correspond to the slip. Therefore array analysis can not determine slip angles and support or disprove any of the proposed values.

Previous studies also estimate varying event focal depths, as follow:

- 11.1km, Institute of Earth Sciences in Taiwan.
- 15 km, Harvard Moment Tensor Catalogue.
- 38 km, International Seismological Centre (Goldstein et al., 1991).

This array analysis will determine its own depth value and compare it to the results of previous studies conducted. The event epicentral location and fault trace are presented in Figure 3A- 5.

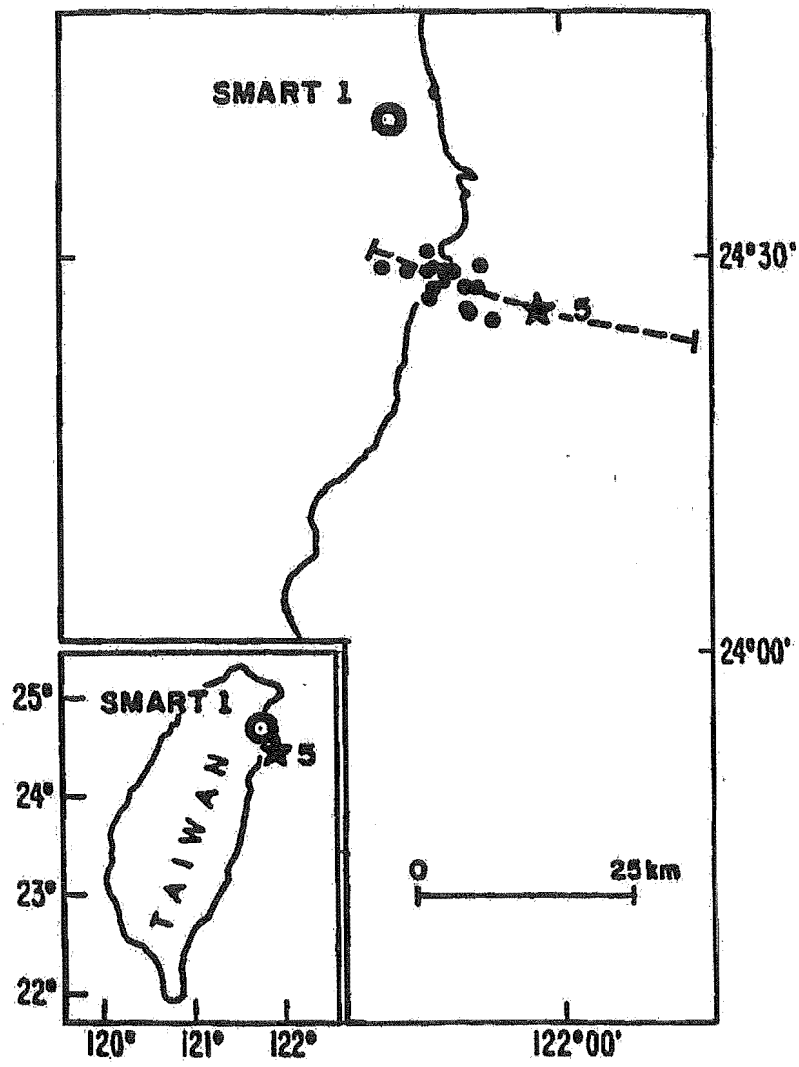

Figure 3A- 5: Event 5 epicentral location and fault trace (from Goldstein, 1988). Spots indicate aftershocks.

2.3. Previous studies

Various studies of Event 5 have lead to different conclusions on the rupture parameters, and interpretations of the direction of rupture. Abrahamson (1985), studying the wave polarization inferred a clockwise rotation of the peaks in the frequency-wavenumber spectra that was consistent with the East-West trend of the rupture propagation inferred from the aftershock study. This analysis is confirmed by studies from Goldstein (1988) and Goldstein et al. (1991). On the other hand, a study by Darragh (1987) indicated a counter clockwise direction of rupture.

The length of the rupture area inferred from Goldstein's array analysis is approximately 100 km (Goldstein, 1988). This fault size is not in agreement with the magnitude-length

relationship (Lay and Wallace, 1995) which suggests a length of approximately 10 to 30 km. The other studies do not provide any value, given that they are primarily interested in finding the azimuth of the sources. This new application of dense array analysis hopes to bring new insights into understanding the Event 5 rupture process.

B Processing and slowness/fault spectra results

The magnitude 5.9 Event 5 data recorded at the SMART-1 array are processed and analysed applying the dense array analysis described in chapter 1. Results are interpreted and compared, where possible, with the conclusions from previous studies. Analyses consist of preparing the data by filtering and aligning the seismograms, defining the optimal time windows of analysis, computing the slowness spectra and projecting them onto a fault diagram to visualize and quantify the rupture propagation.

1 Vertical component analysis

1.1. Preparation of the data

The data are prepared by filtering and aligning the seismograms. Vertical components are filtered from 0.5 to 20 Hz applying a Butterworth filter. Following the conclusion from Chapter 2 that results are very sensitive to the alignment process, data have been re-sampled by a factor of 10 from their original 50 Hz. The phase chosen to align the seismograms is a distinctive downwards pulse at 3.96 seconds on the central station recording. Examples of the marked phase on the central station record and records at stations O06, M08, and M12 are shown on Figure 3B- 1. The first arrival phase is indicated by an arrow. Recordings are displayed in chronological order of arrival of the first phase, from bottom to top.

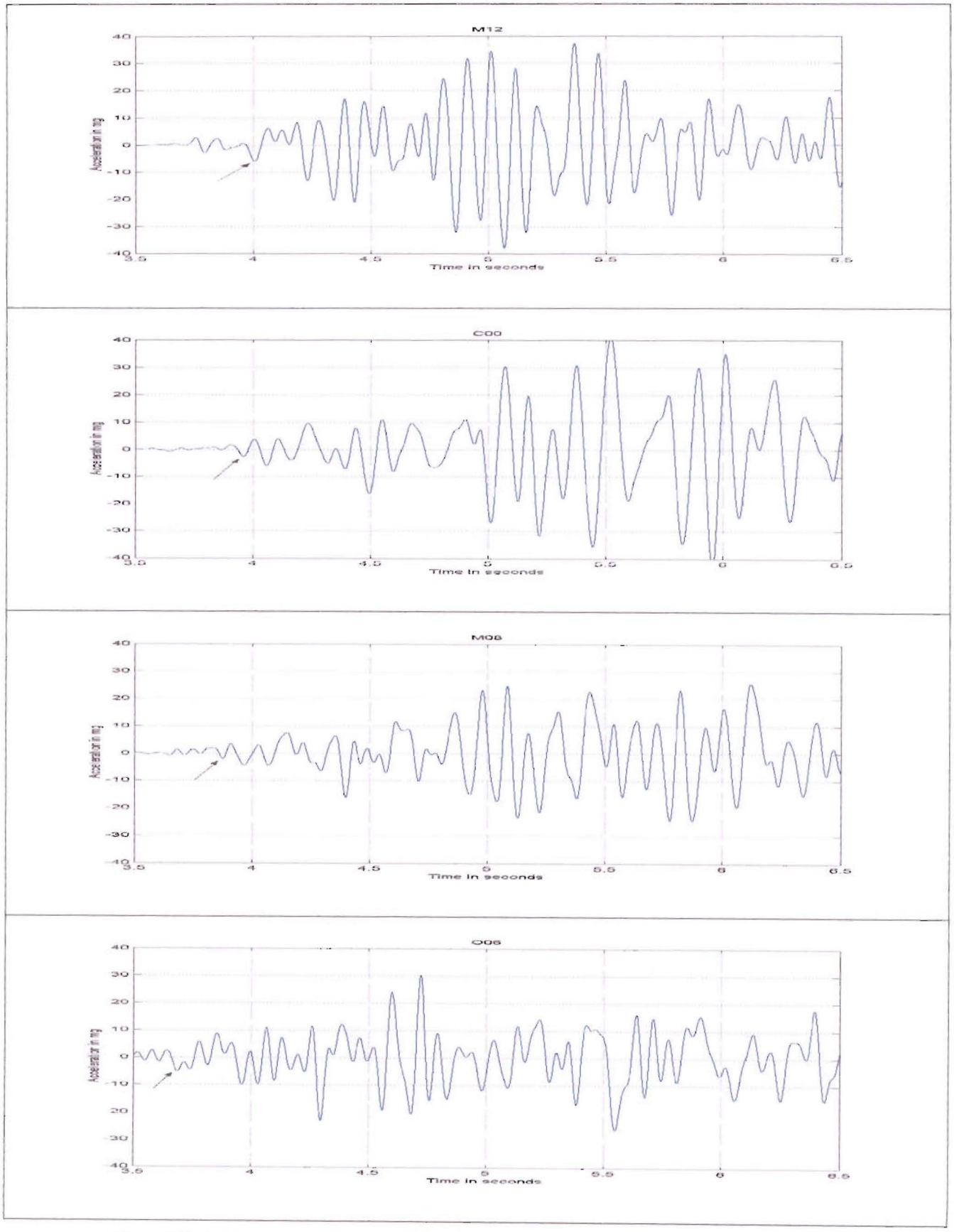

Figure 3B- 1: Vertical components of some seismograms recorded at the SMART-1 array.

Given that the SMART-1 stations are located on various substrata, variation between seismograms is significant, thus makes detecting the first phase arrival difficult. Also, when looking at the three components of Event 5 recorded at station M06 (Figure 3B- 2), the vertical component shows characteristics of a horizontal recording. These characteristics include little energy for the P arrivals and prominent S arrivals. Therefore, like Goldstein (1988), I chose not to use the vertical component data of station M06 in the analysis.

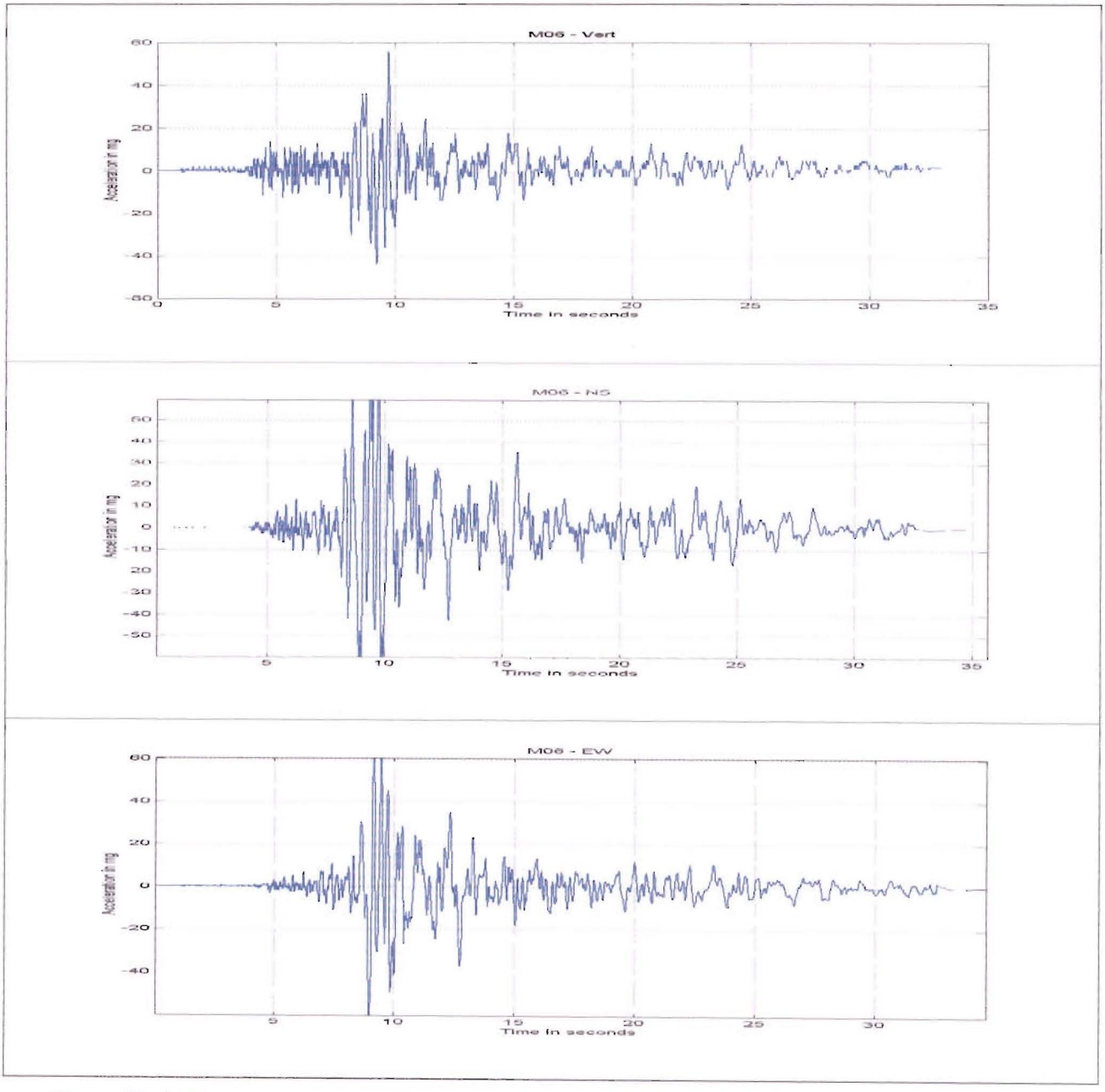

Figure 3B- 2: From top to bottom: Vert., NS and EW components recorded at station M06. The vertical component presents the characteristics of a horizontal recording.

Nonetheless, the time shifts calculated are consistent with those obtained by Goldstein (1988) on the same set of data. These shifts are listed in Table 3B- 1.

Station index	Code Name	Goldstein (1988)	This study (2004)
1	C00	0	0
2	I03	-0.002	0.008
3	I06	-0.043	-0.04
4	I09	-0.003	-0.003
5	I12	0.023	0.014
6	M01	0.06	0.06
7	M02	0.038	0.023
8	M03	-0.031	-0.039
9	M04	-0.12	-0.115
10	M05	-0.157	-0.142
	M06		
11	M07	-0.143	-0.14
12	M08	-0.091	-0.084
13	M09	-0.085	-0.092
14	M10	0.041	0.028
15	M11	0.075	0.062
16	M12	-0.158	-0.167
17	O01	0.167	0.162
18	O02	0.064	0.045
19	O03	-0.154	-0.096
20	O04	-0.205	-0.246
21	O05	-0.352	-0.355
22	O06	-0.357	-0.35
23	O07	-0.31	-0.305
24	O09	0	-0.015
25	O10	0.147	0.18
26	O12	0.195	0.182

Table 3B- 1: Shift times in seconds for Event 5 vertical data

1.2. Slowness shift and azimuth

The azimuth of the first incoming wave and its slowness vector are computed by fitting a planar wave front to the shift times above. To optimize the fitting, only the outer stations are taken into account in the computations. The azimuth and apparent slowness components of the first incoming plane wave are:

SX = -0.0596 s/km

SY = 0.1319 s/km

Azimuth = 155.7 degrees

These results are very satisfying considering that the known azimuth of the source is approximately 150 degrees.

1.3. Slowness maps

Each point source from the fault plane in the SMART-1 case study is given a horizontal slowness value. These have been obtained using the TauP Toolkit (Crotwell et al., 1999). The velocity profile necessary for the slowness map computations is the one used by Goldstein et al (1991) who combined the studies of Wen et al (1983), Roecker et al. (1987) and Hagen et al. (1988). This profile is presented in Table 3B- 2.

Layer	**Thickness (km)**	**Depth (km)**	**Average P velocity (km/s)**
1	0.012	.012	.6
2	0.045	.057	1.55
3	0.35	.407	1.9
4	0.593	1	2.5
5	4	5	4.5
6	15	20	6.5
7	20	40	7
8	10	50	7.5

Table 3B- 2: Velocity profile used in the SMART-1 case study

The X component of slowness corresponding to the East-West direction is shown in Figure 3B- 3. The Y component corresponding to the North-South direction is shown in Figure 3B-4. The slowness maps are satisfying given they both present a good range of slowness values. As expected, the X and Y components are orthogonal. Assuming the location of the fault plane is south of the array, the Y components of slowness are always negative. West of the fault plane, the slowness vectors have high absolute Y values and low X values. East of the fault plane, the slowness vectors have low absolute Y values and increasing X values. These results are contrary to those obtained in the synthetic case study in Chapter 2. This is due to the opposite array-fault configuration of the two case studies. Also, given that slowness vectors are the projections of the ray parameters, deeper source locations present lower slowness values for both X and Y components.

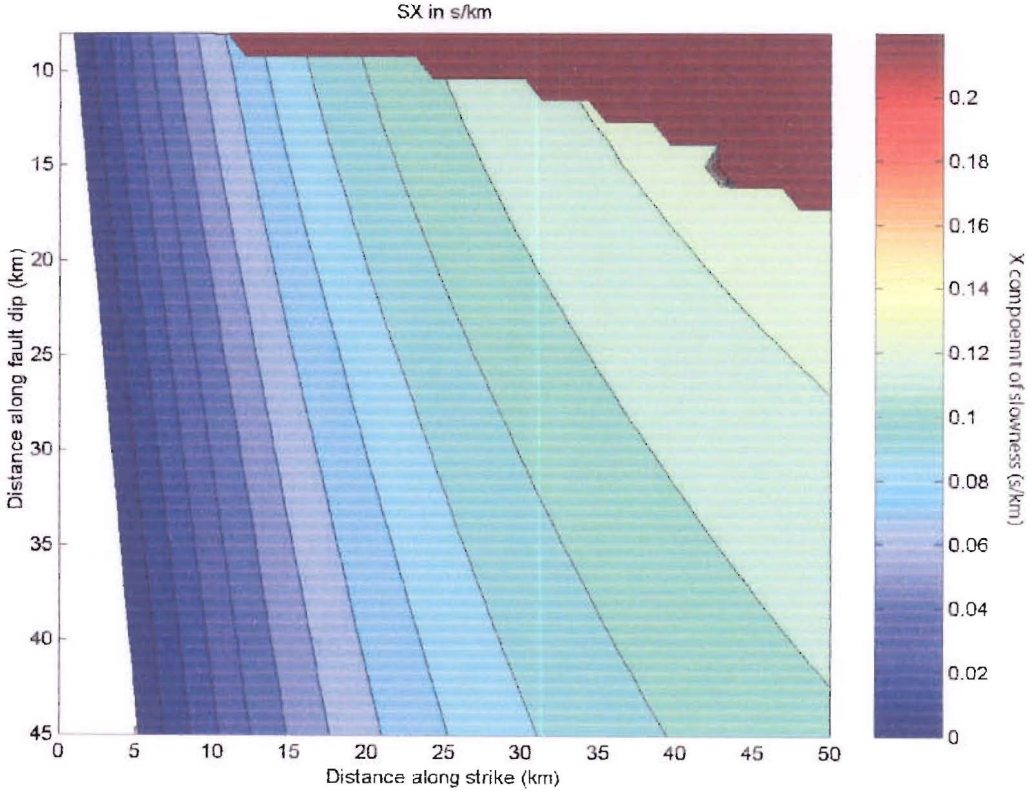

Figure 3B- 3: Fault map of slowness East-West component. The dark region east of the fault plane and above 15 km is due to a lack of point sources at shallow depths.

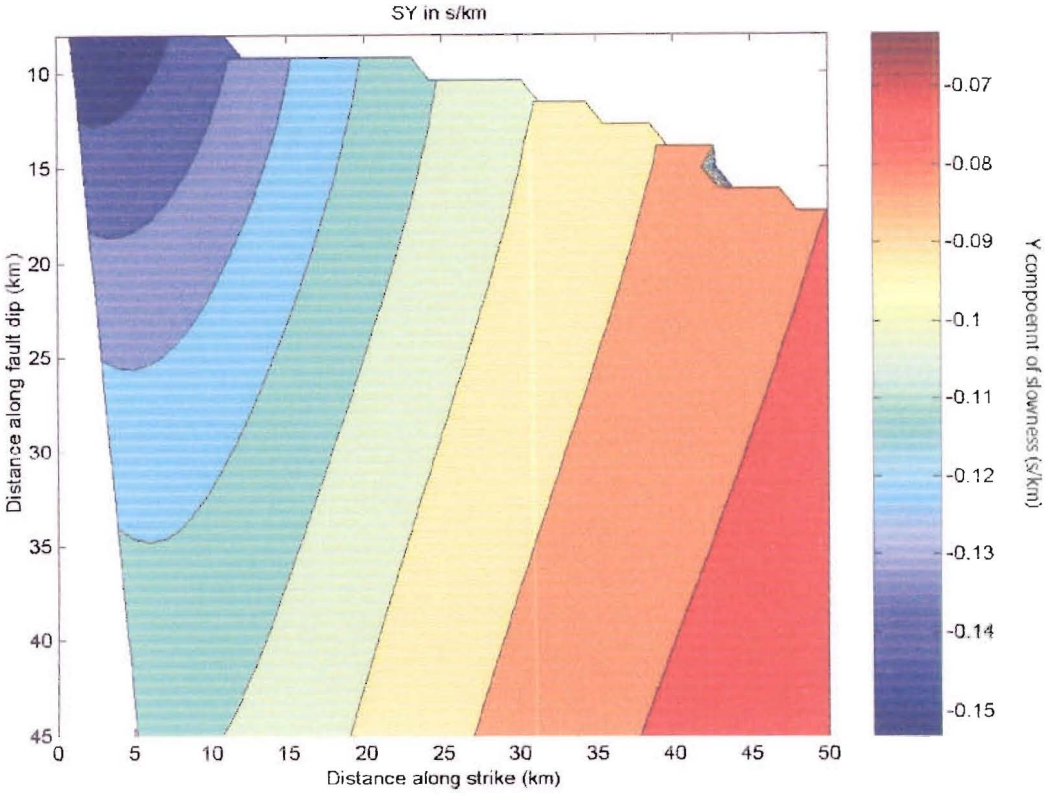

Figure 3B- 4: Fault map of the slowness North-South component. The blank region east of the fault plane and above 15 km is due to a lack of point sources at shallow depths.

1.4. Time window analysis

In this case study the method of QEE (Quantity of Explainable Energy) can be applied to determine the optimal time windows of analysis. In the synthetic data case study, the fault rupture is characterized by constant patches of energy. Therefore the QEE method was not relevant and it was best to assume that the regularly spaced windows each contained a source signal. A real fault rupture however is expected to generate random bursts of energy which arrive irregularly at the array. Therefore the QEE method is more appropriate to determine the time windows that will capture these irregular signals. The QEE is estimated for a range of time windows starting from 3.9 seconds, regularly spaced every 0.1 second, with window widths varying from 0.2 seconds to 0.6 seconds. Given that the range of QEE values is large, in order to capture all the relevant information, multiple graphs are required. The results from 3.9 to 4.6 seconds are shown on Figure 3B- 5, with the remaining computed graphs are to be found in the Appendix B.

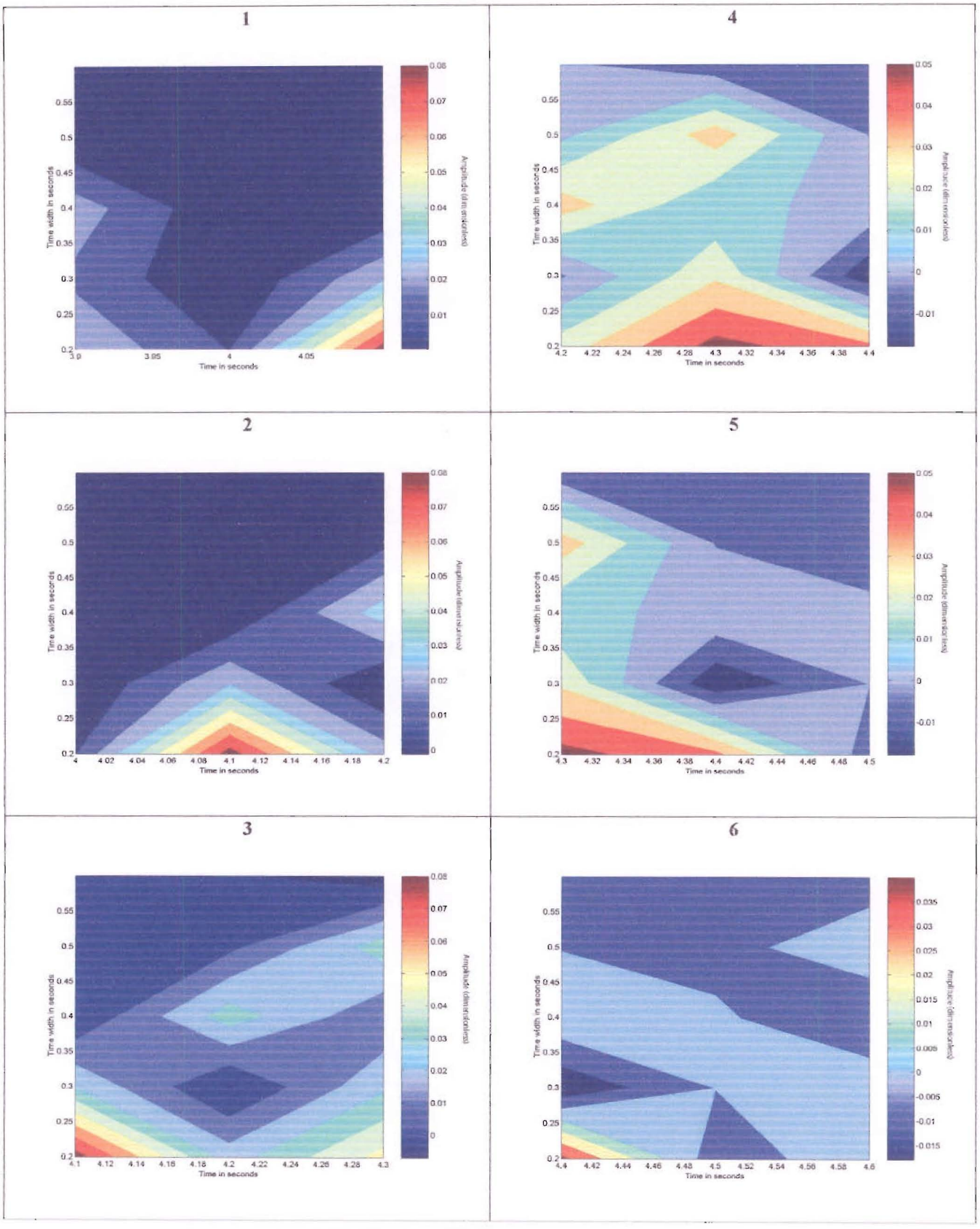

Figure 3B- 5: Results of the QEE analysis for time windows from 3.9 to 4.6 seconds

From 3.9 up to 4.6 seconds, peaks of QEE appear at 4.1 and 4.3 seconds for window widths of 0.2 seconds. Secondary peaks appear at 4.2 and 4.3 seconds for window widths of 0.4 and 0.5 seconds respectively (Figure 3B- 5.4). These should not be taken into consideration given that they are captured at the narrow window widths. Time window widths resulting from the QEE analysis range from 0.2 to 0.4 seconds with a predominance of 0.2 second long windows.

1.5. Slowness spectra

Slowness spectra are computed for every time window defined by the QEE analysis. These are presented in Figure 3B- 6. All the spectra computed at every time window are provided in Appendix C. The single sharp peak indicates that the resolution of the source is good.

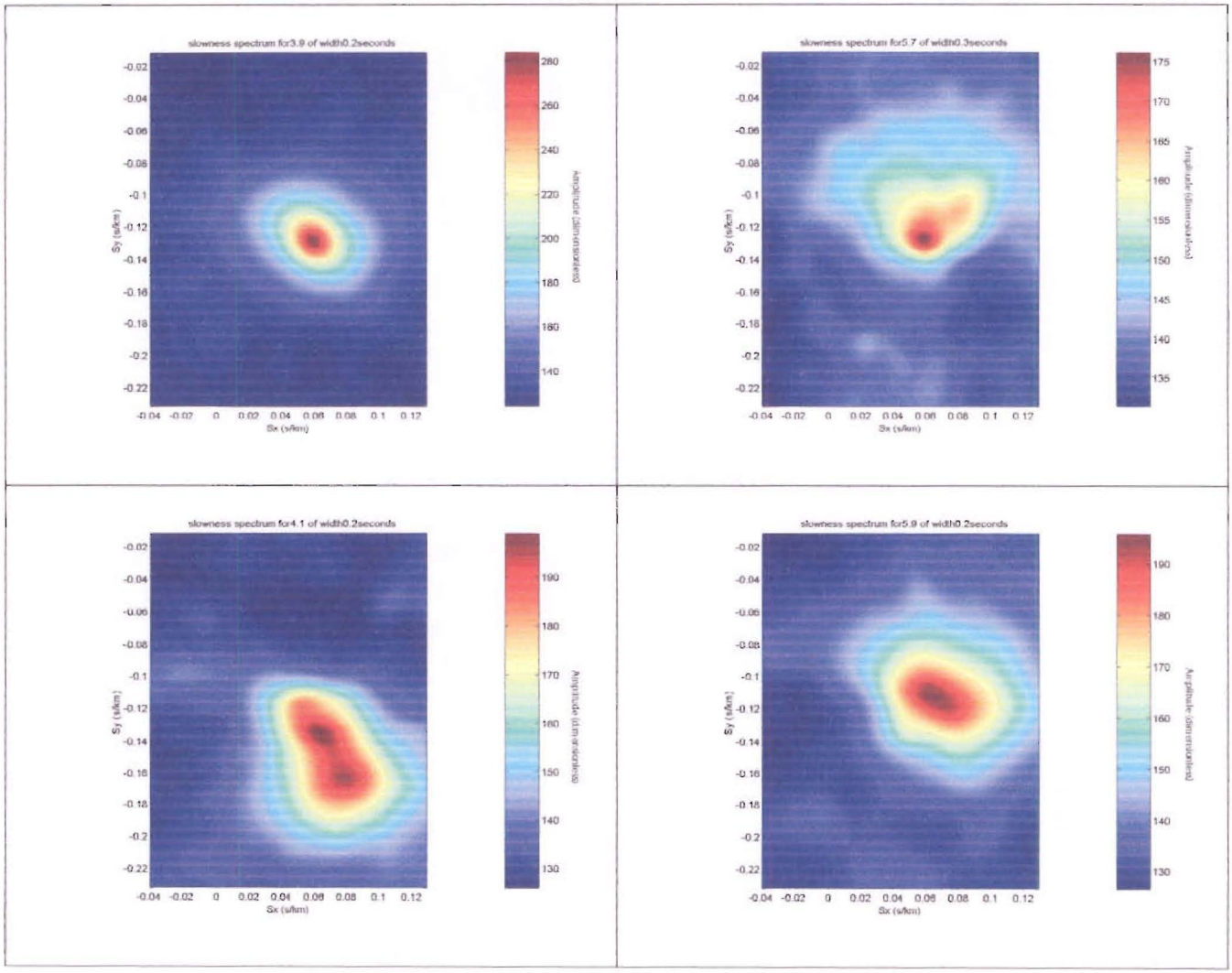

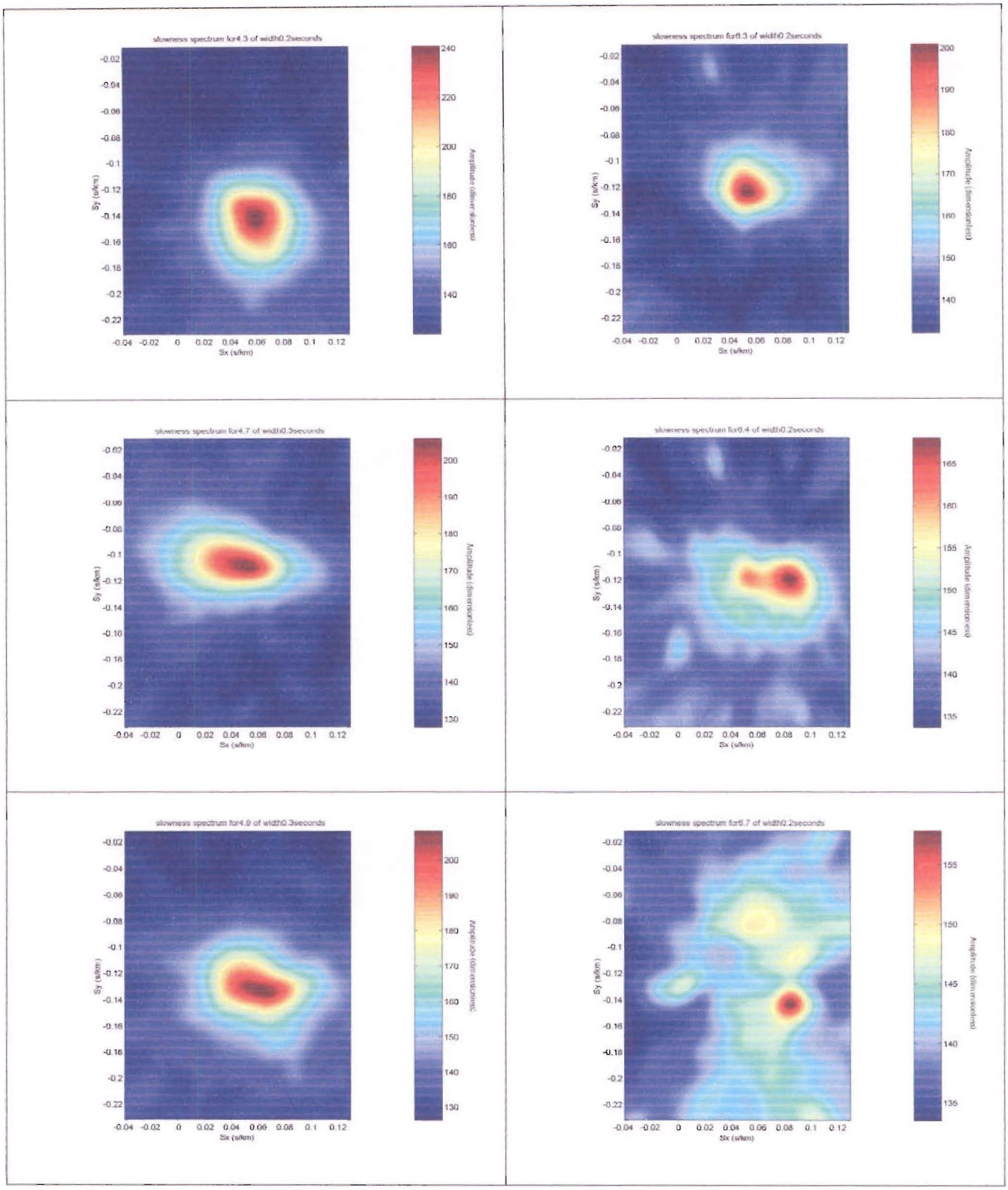

Figure 3B- 6: Slowness spectra obtained for the vertical data for successive time windows. Spectra on the left are computed from 3.9 to 4.9 seconds. Spectra on the right are computed for 5.9 to 6.4 second windows for which the signal is degrading.

1.6. Rupture fault map

The slowness spectra peaks are projected onto the fault plane applying the slowness maps described previously. Travel times are computed for each of the point sources and removed from the central time to obtain the true rupture time. Sources and their respective rupture times are plotted in Figure 3B- 7. Selected points indicated by the arrows are used to compute rupture velocities. These points were strictly chosen because their respective slowness spectrum is sharp, they correspond to early time on the seismograms, and they appear to follow a continuous rupture direction.

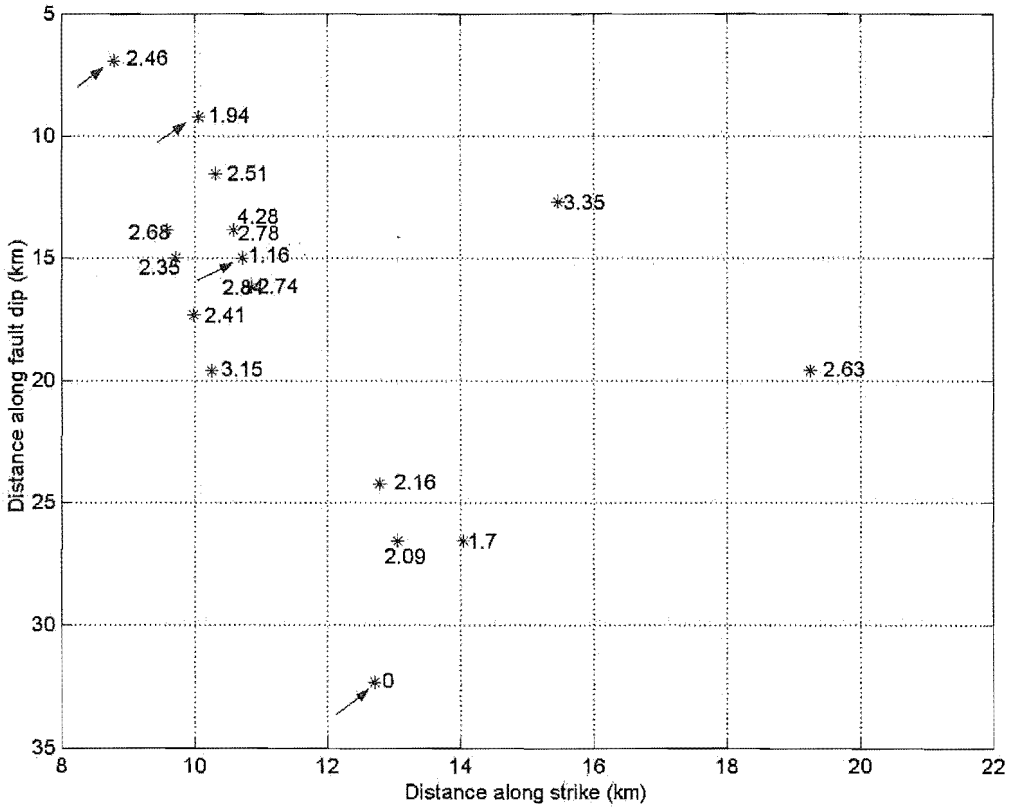

Figure 3B- 7: Fault map of the first 18 rupture points for the vertical data

The "zero rupture time point" or hypocenter is located between 30 and 35 km deep and 12 to 14 km along the fault. The rupture direction trend is upward from East to West. The few points that do not follow the trend, such as at 3.35 seconds arrive rather late on the seismograms and should not be given as much consideration. The source rupture times and fault locations are detailed in Table 3B- 3.

Cent. Time	Rupt. Time	Source Location X and Z	Δdist (km)	Δ time(s)	Velocity (km/s)
3.9	**1.16**	**(10.73,15.01)**	**1.16 to 1.94: 5.80**	**0.78**	**7.43**
4.1	**1.94**	**(10.06,9.24)**	**1.94 to 2.46: 2.63**	**0.52**	**5.05**
4.3	**2.46**	**(8.80,6.93)**			
4.7	**0.00**	**(12.72,32.33)**	**0 to 1.16: 17.43**	**1.16**	**15.02**
4.9	2.51	(10.33,11.55)			
5	2.35	(9.73,15.01)			
5.2	2.68	(9.59,13.86)			
5.3	2.41	(9.99,17.32)			
5.4	2.78	(10.59,13.86)			
5.6	2.74	(10.86,16.17)			
5.7	2.84	(10.86,16.17)			
5.9	1.70	(14.05,26.56)			
6	2.16	(12.79,24.25)			
6.2	2.09	(13.05,26.56)			
6.3	3.15	(10.26,19.63)			
6.4	3.35	(15.46,12.70)			
6.7	2.63	(19.26,19.63)			
6.9	4.28	(10.59,13.86)			

Table 3B- 3: Fault source parameters for the vertical components. Values in bold are related to sources indicated by the arrow on the fault rupture map. 'Cent. Time' is the time measured on the seismograms; 'Rupt. Time' is the rupture time; Source location is in km, along strike and depth respectively as shown in Figure 3B- 7.

From Table 3B- 3, the rupture velocities range from 15.02 km/s for the earliest points to 5.05 seconds for the later points. These values are higher than expected (approximately 3 km/s). Nonetheless, an initial conclusion is that the rupture starts with a high velocity and then slows down as it propagates. Such high rupture velocity has also been observed by Xia et al. (2004) with "laboratory earthquakes'.

2 Horizontal component analysis

2.1. Preparation of the data

As for the vertical component analysis, the horizontal data are filtered and aligned prior to performing array analysis.

Seismogram alignment results

As shown in Figure 3B- 8 and Figure 3B- 9 the S wave alignment is completed at 8.81 seconds for the EW components and at 8.96 seconds for the NS components respectively.

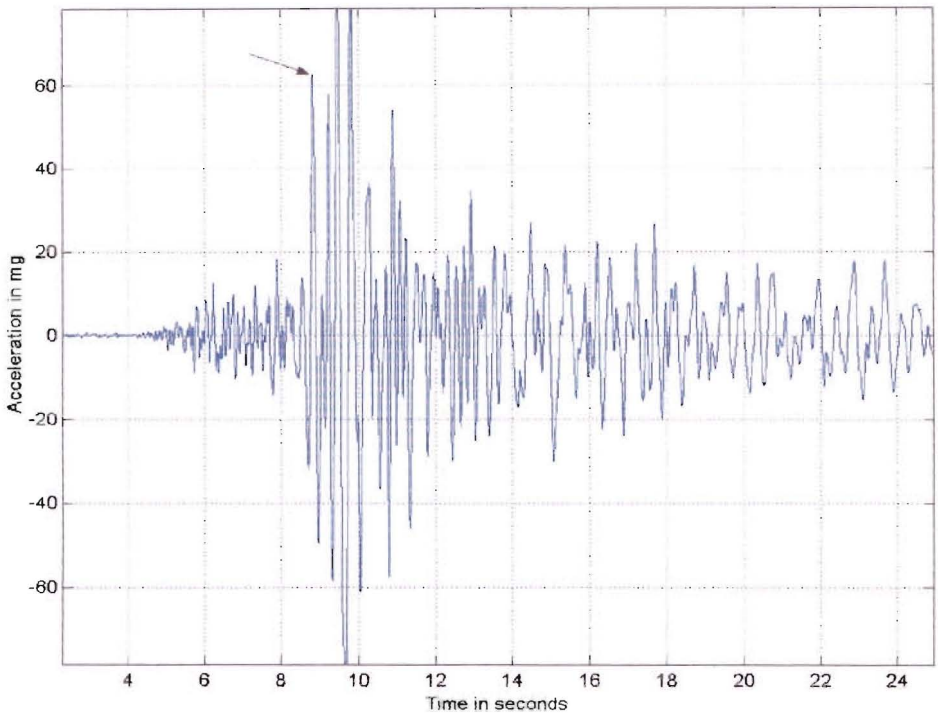

Figure 3B- 8: Central station EW component alignment phase

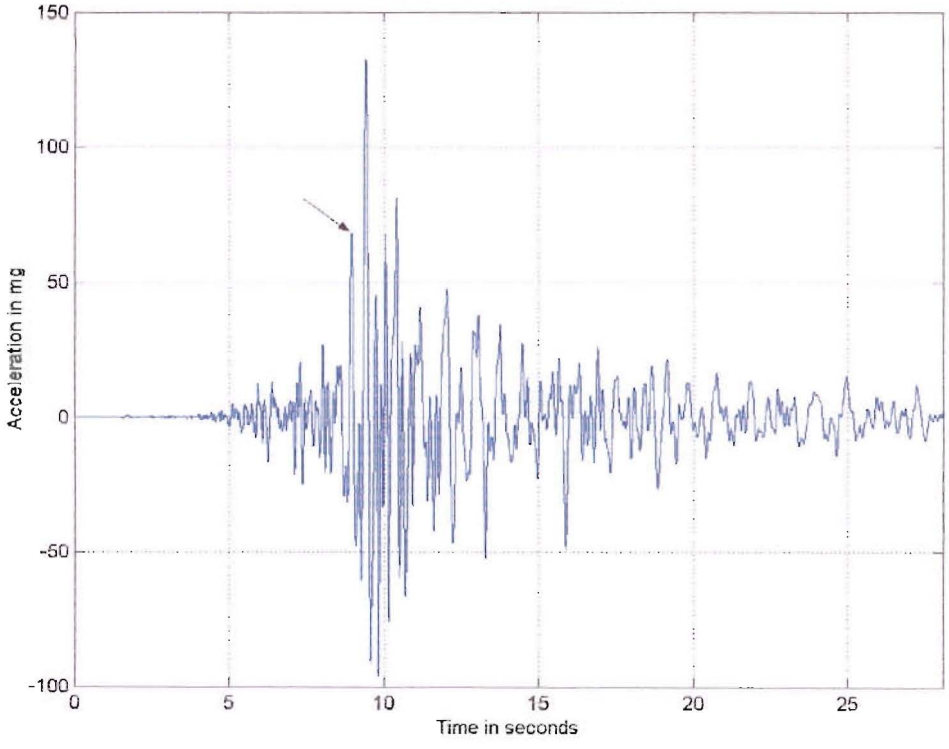

Figure 3B- 9: Central station NS component alignment phase

Shift times from the alignment of the seismograms to the first S-arrivals are shown in Table 3B- 4. Even though the time shifts are quite similar for the EW and NS components, one would expect them to be identical. This difference could be due to the data recorder itself or the pre-processing applied to the raw data.

Station index	Code Name	N-S Components (sec)	E-W Components (sec)
1	C00	0	0
2	I03	0.023	0.01
3	I06	0.046	0.06
4	I09	0	0
5	I12	-0.008	-0.008
6	M01	-0.12	-0.112
7	M02	-0.026	0.07
8	M03	0.08	0.04
9	M04	0.248	0.226
10	M05	0.36	0.36
11	M06	0.365	0.25
12	M07	0.285	0.28
13	M08	0.13	0.11
14	M09	0.11	0.09
15	M10	-0.05	-0.04
16	M11	-0.11	-
17	M12	0.106	0.132
18	O01	-0.3	-0.31
19	O02	-0.196	-0.15
20	O03	0.057	0.038
21	O04	0.425	0.4
22	O05	0.8	0.775
23	O06	0.81	0.8
24	O07	0.68	0.64
25	O09	0.095	0.13
26	O10	-0.17	-0.16
27	O12	-0.41	-0.38

Table 3B- 4: Time shift computed for the NS and EW components

Slowness shifts and azimuths

The azimuth and apparent slowness components of the first incoming S-wave are presented in Table 3B- 5.

Component	SX (s/km)	SY(s/km)	Azimuth (degrees)
EW	-0.094	0.2491	159.3
NS	-0.1185	0.2571	155.25

Table 3B- 5: Azimuth and apparent slowness components of the first incoming S-wave

These results are satisfying considering that the known azimuth of the source is approximately 150 degrees. Nonetheless, the results for the NS components are slightly better than those for the EW components. Theoretically the results should be identical for the three components. Given that time differences exist between all three components and not only between horizontal and vertical, they are most likely to be due errors from manually picking the arrival times.

Slowness maps

The velocity model used to generate the fault slowness maps for the S-waves is derived from the model described previously. As for the slowness maps obtained for the P-wave analysis, the EW slowness components are lower west of the fault map and increase for increasing distances along fault strike. They also decrease for deeper sources as shown in Figure 3B- 10.

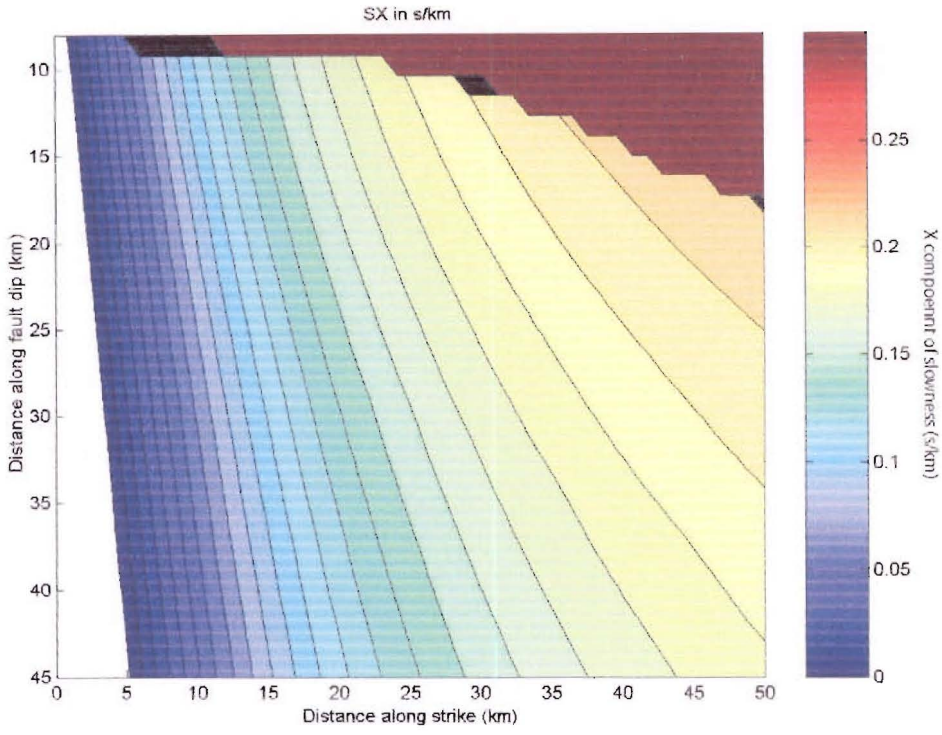

Figure 3B- 10: Fault map of the S-slowness East-West component

NS slowness components are negative. The absolute value is decreasing for deeper sources as shown in Figure 3B- 11.

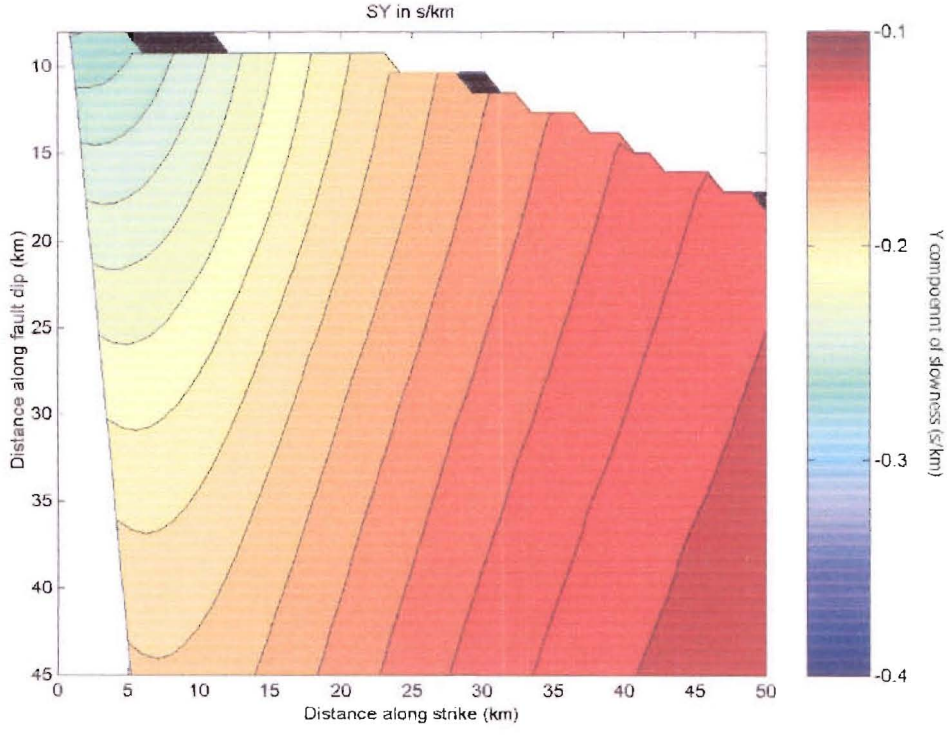

Figure 3B- 11: Fault map of the S-slowness North-South component

2.2. Time window analysis

The QEE method is applied to determine the optimal time windows. The analysis is run starting at 8.8 second for the EW component and 8.96 second for the NS component. The time windows are spaced regularly every 0.1 second. The analysis is terminated for time windows for which the slowness spectra start to degrade. Results are the following:

- 11 time windows from 8.8 to 10.7 seconds are calculated for the EW component analysis.
- 8 windows from 8.96 to 11.1 seconds are calculated for the NS component analysis.

QEE graphs for the horizontal component analysis can be found in the Appendix D.

2.3. Slowness spectra and fault rupture maps

East-West components

The slowness spectra computed for the 11 time windows described previously are provided in the Appendix E. Figure 3B- 12 shows spectra obtained for the first time windows (left column) and the final ones before the spectra start to degrade (right column). Overall the spectra are satisfying, given that they present a single central peak that is well resolved.

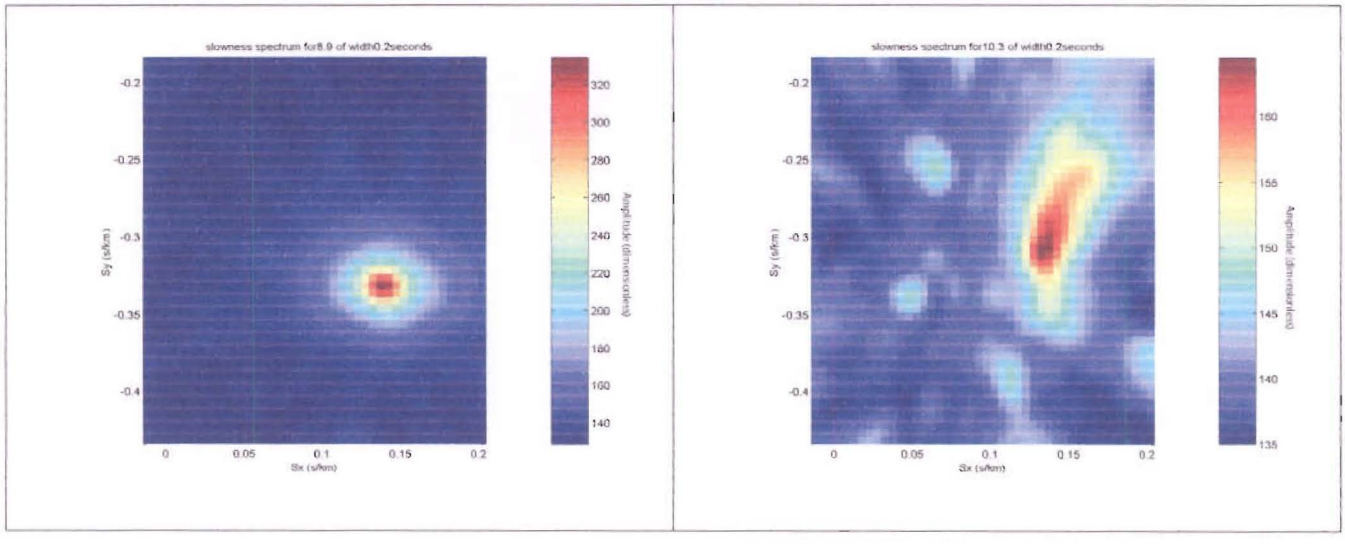

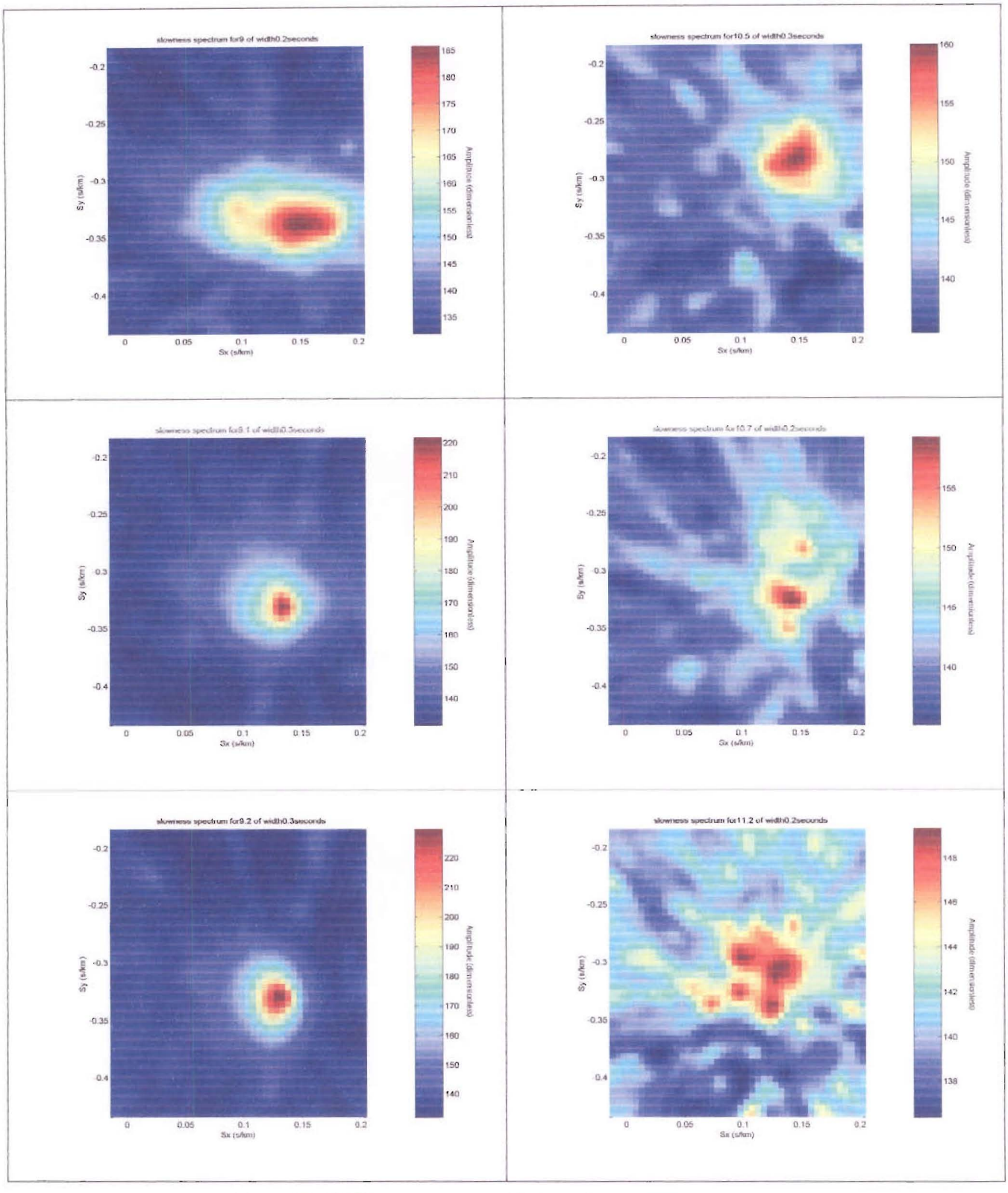

Figure 3B- 12: Slowness spectra obtained for the EW components

Peaks of the slowness spectra are projected onto the fault plane using the slowness maps described earlier. The travel times corresponding to each location on the fault are computed and removed from the central times of the computation windows. These are the true rupture times. Projected peaks and their respective rupture times are plotted in Figure 3B- 13. The

fault map presents an upward East to West rupture trend. For the EW component the hypocentre is located 18 km deep and 20 km east along the fault plane. The following rupture points are more superficial: between 5 and 13 km deep along the fault plane and west of the fault plane: between 8 and 12 km.

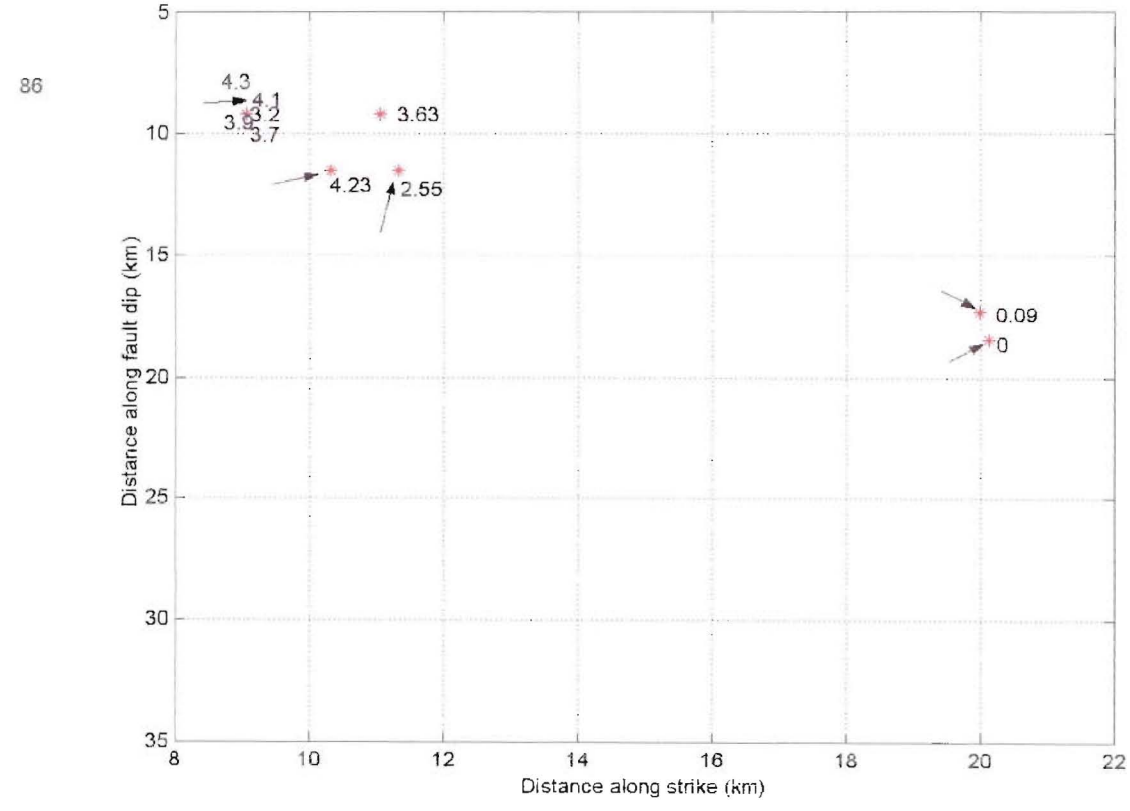

Figure 3B- 13: Fault rupture map obtained for the EW components

The points on Figure 3B- 13 indicated by the arrows are used to compute rupture velocities. The source rupture times and fault locations are detailed in Table 3B- 6.

Cent. Time	Rupt. Time	Source Location X and Z	Δdist (km)	Δ time(s)	Velocity (km/s)
8.8	3.10	(9.06,9.24)			
8.90	**3.20**	**(9.06,9.24)**	**0 to 3.20: 14.40**	**3.2**	**4.5**
9.00	**2.55**	**(11.33,11.55)**	**0 to 2.55: 11.20**	**2.55**	**4.39**
9.10	**0.09**	**(19.99,17.32)**	**0 to 0.09: 1.16**	**0.09**	**12.88**
9.20	**0.00**	**(20.13,18.48)**	**0 to 3.70: 14.40**	**3.7**	**3.89**
9.40	**3.70**	**(9.06,9.24)**	**2.55 to 3.7: 3.23**	**1.15**	**2.8**
9.60	3.90	(9.06,9.24)			
9.80	4.10	(9.06,9.24)			
10.00	**4.30**	**(9.06,9.24)**	**0 to 4.30: 14.40**	**4.3**	**3.34**
10.50	4.23	(10.33,11.55)			

Table 3B- 6: Fault sources parameters. Values in bold are related to sources indicated by the arrows on the fault rupture map.

As for the vertical component analysis, rupture velocities cover a wide range: from 2.8 to 12.88 km/s. As found previously, the velocity is initially very high for the early points before decreasing to values closer to those expected. The difference between this rupture map and that obtained from the vertical components is discussed in Chapter 3C.

North-South components

The slowness spectra computed for the 8 time windows are shown in Figure 3B- 14. As for the EW components, the spectra are satisfying given that they all present a sharp single central peak.

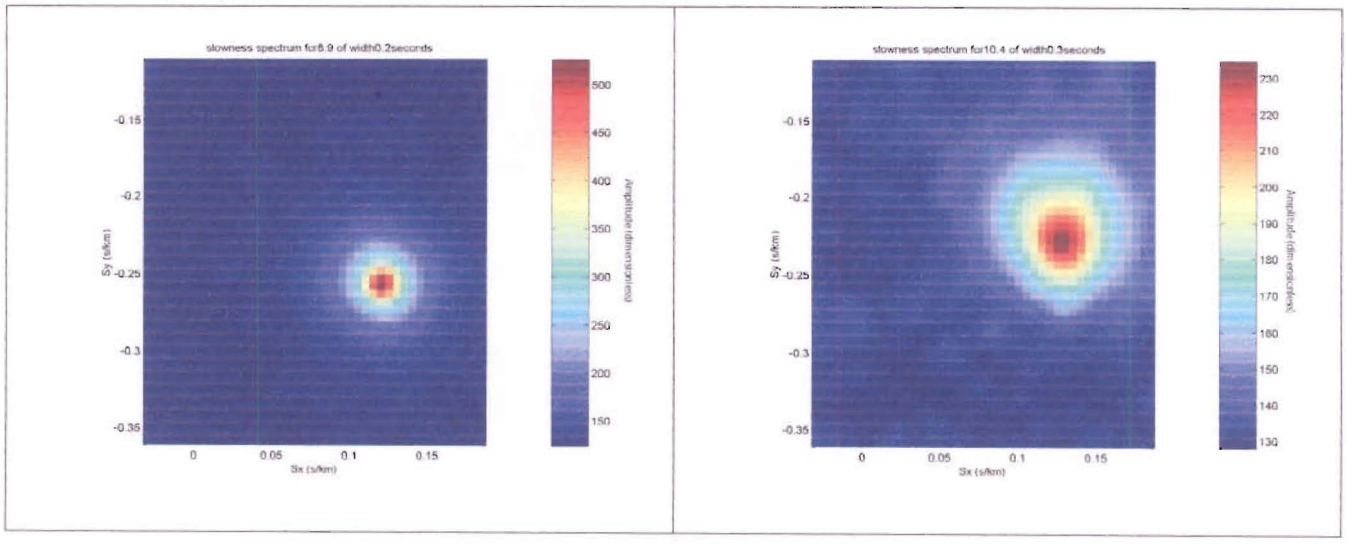

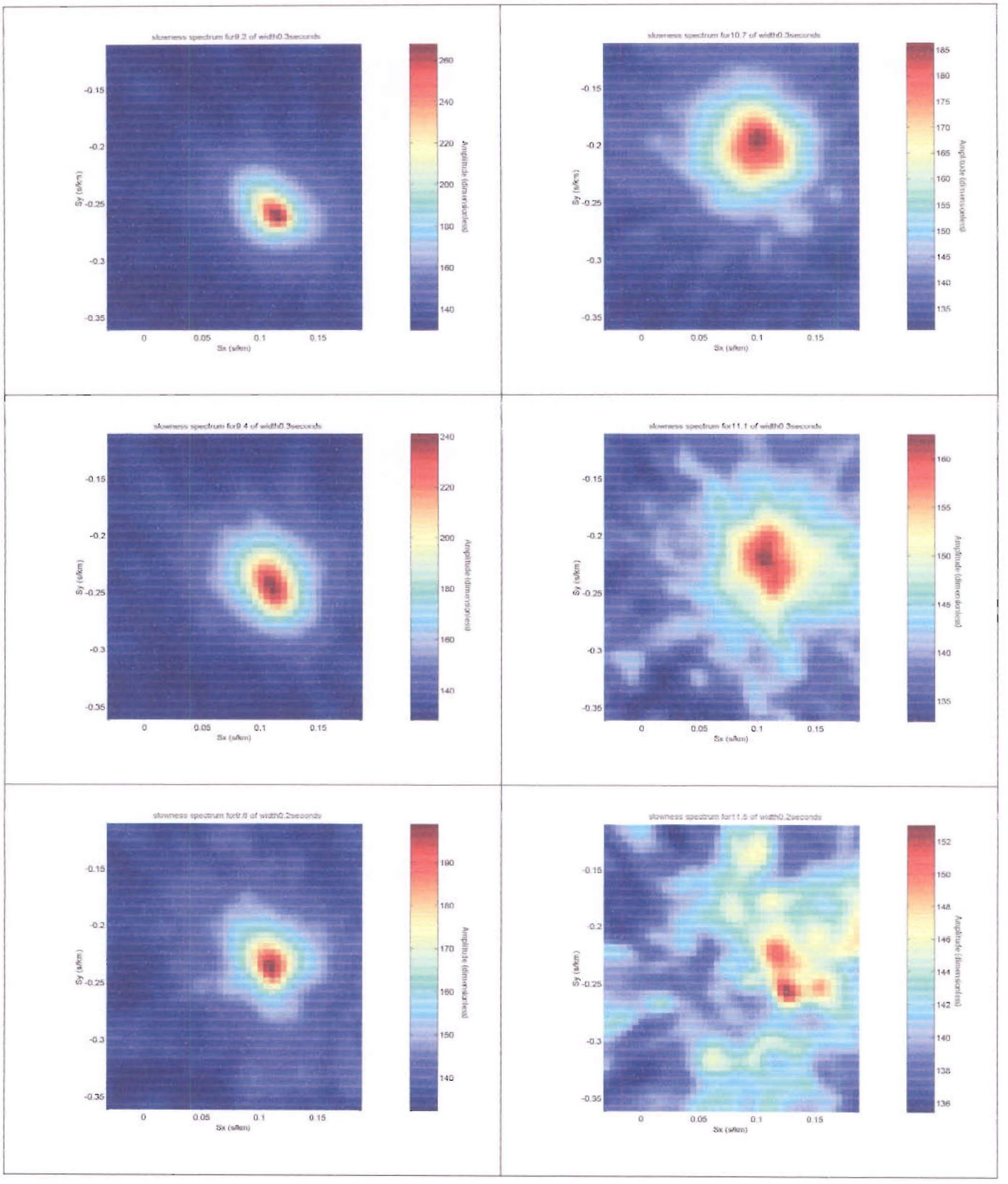

Figure 3B- 14: Slowness spectra for the NS component

The spectrum peaks are projected onto the fault plane to obtain the rupture fault map, as shown in Figure 3B- 15.

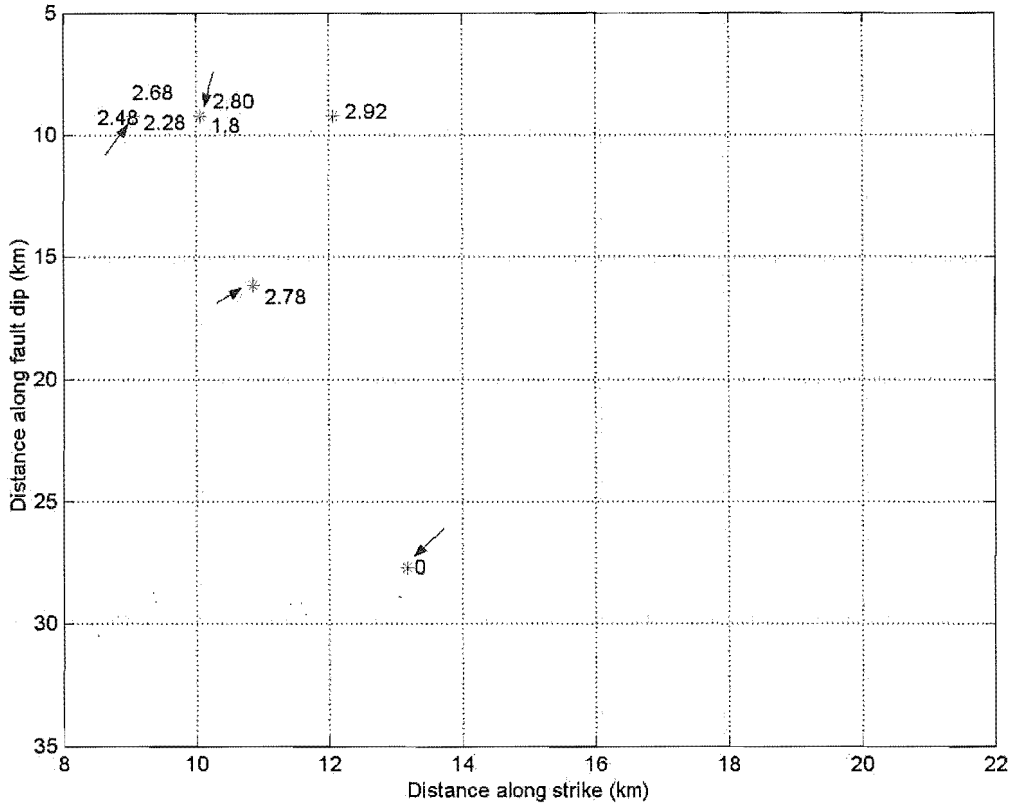

Figure 3B- 15: Fault map of the source points obtained for the NS components

The map presents the same upward East to West rupture trend as for the EW and vertical component analyses. The hypocenter is located between 25 and 30 km deep and 12 to 14 km along the fault. The later points between 5 and 10 km are more superficial. The source rupture times and fault locations indicated by the arrows are detailed in Table 3B- 7.

Cent. Time	Rupt. Time	Source Location X and Z	Δdist (km)	Δ time(s)	Velocity (km/s)
8.90	**1.80**	**(10.06,9.24)**	**0 to 1.80: 18.73**	**1.80**	**10.40**
9.20	2.28	(9.06,9.24)			
9.40	**2.48**	**(9.06,9.24)**	**2.48 to 2.80: 1**	**0.32**	**3.13**
9.60	2.68	(9.06,9.24)			
9.90	**2.80**	**(10.06,9.24)**	**0 to 2.80: 18.71**	**2.80**	**6.68**
10.40	2.92	(12.06,9.24)			
10.70	**0.00**	**(13.19,27.71)**	**0 to 2.48: 18.92**	**2.48**	**7.62**
11.10	**2.78**	**(10.86,16.17)**	**0 to 2:78: 11.77**	**2.78**	**4.23**

Table 3B- 7: Fault sources parameters for the NS components. Values in bold are related to sources indicated by the arrows on the fault rupture map.

As for the two previous components, the rupture velocity is initially very high 10.40 km/s, before slowing down to a more expected velocity 3.13 km/s.

3 Conclusion

Except for the common horizontal component slowness maps, analyses of the three components of the Event 5 SMART1 data were made independently. Nonetheless, common points concerning the rupture direction, the rupture velocity, the sources location and the fault area are evident. These points are detailed further in Chapter 3-C.

C Conclusion on array measurement of Event 5

This section compares results obtained from the study of the three components of Event 5 data to those from previous studies. Results from the three components Vertical, EW and NS are expressed in the form of a fault map of point sources and their respective rupture times. The fault map is shown in Figure 3C- 1. Sources in red are obtained from the EW component analysis, sources in green are obtained from the NS analysis, and sources in blue from the vertical component analysis.

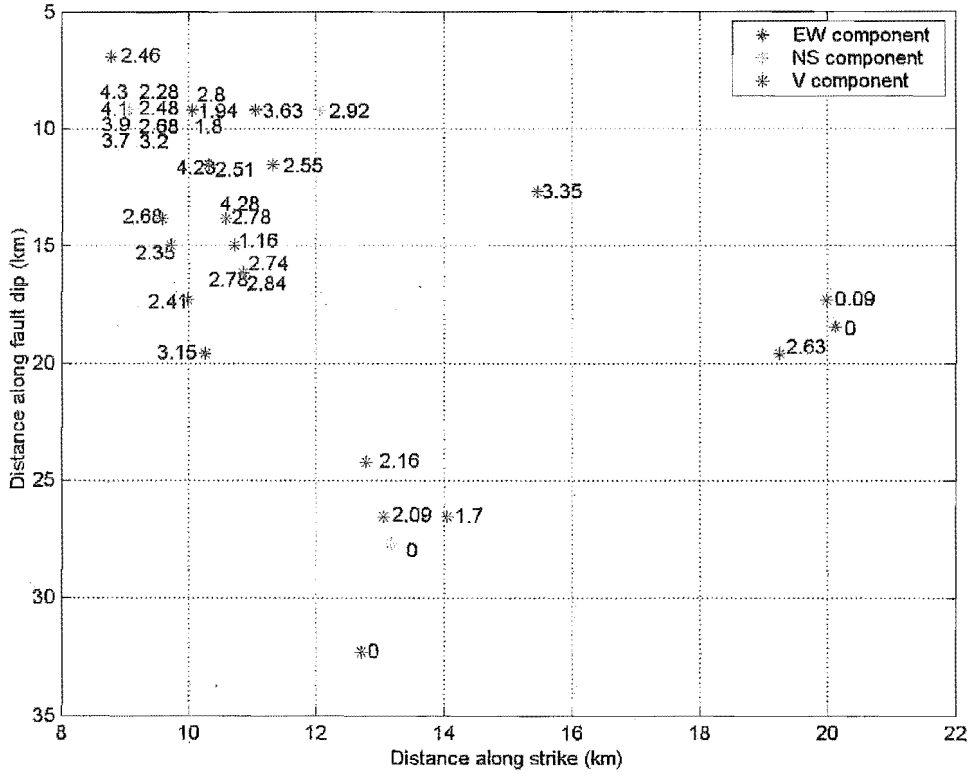

Figure 3C- 1: Fault map of the three component source locations. Each source is affected a rupture time.

1 Rupture trend

The overall rupture trend of the sources is upward from East to West. The hypocenter locations are, for each component analysis, very distinct from the rest of the sources being at least 10 km away. This result is in agreement with the majority of previous studies from Abrahamson (1985), Goldstein (1988) and Goldstein et al. (1991) that have concluded a clockwise rotation of the slowness peaks.

2 Hypocenter location

Hypocenter locations for the vertical component and the NS component studies are very close. They are both approximately 13 km along the fault strike. The NS component hypocentre is 28 km deep along the fault plane and the vertical component hypocentre is 32 km deep along the fault plane. By taking into account the 60 degree dip of the fault plane, these depths along the fault plane correspond respectively approximately to real depths of 24 and 27.5 km. The hypocentral location for the EW component study, on the other hand, is further away: 20 km along the fault strike and only 18 km deep along the fault plane. The real depth is 15.5 km. However, this position is confirmed by the location of the source point at 0.09 seconds immediately following the "zero rupture time" hypocentre. Given that the deeper and more superficial hypocentral locations are both supported by two results each, and that horizontal and vertical analysis were found independently, no conclusion can be drawn on the actual location of the hypocenter. Also these results do not allow one to fully support any of the proposed event depths referred to in Chapter 3-A. The proposed depth of 38 km suggested by Goldstein et al. (1991) could be partly supported by the NS and vertical component analyses. On the other hand, the proposed depth of 15 km suggested by the Harvard Moment tensor Catalogue could be supported by the first two points of the EW component analysis. This analysis will therefore propose to take a depth for the hypocentral location of Event 5 of between 15.5 and 27.5 km.

3 Rupture area

The rupture area in this study is defined as the area covered by the projected fault sources. However, considering that array analysis may only be able to "see" sources coming towards the array, it is possible that some sources propagating away from the array could be missed. Thus the true rupture area may be as large as twice the computed area from array analysis. When looking first at all the sources covering the fault surface, the rupture area is approximately 12 km wide by 30 km deep. Given that fault rupture areas are generally wider than they are deep, it is reasonable to multiply this surface width by two. The proposed rupture area is therefore approximately 24 km by 30 km. This result is in agreement with the magnitude-length relationship (Lay and Wallace, 1995) for a magnitude 6 earthquake that suggests a fault length of 10 to 30 km. This result is also more reasonable than the 100 km long fault obtained but contested by Goldstein (1988).

4 Rupture velocities

Rupture velocities obtained from the three component analysis are consistent. The extreme initial value of velocity ranges from 10.40 km/s for the NS component analysis to 15.02 km/s for the vertical component analysis. They also all show a rapid decrease in velocity following the initial rupture. The velocity drops to half its initial value 15.02 km/s to 7.43 km/s for the vertical component analysis; and it drops by a third for the horizontal component analyses: from 12.88 to 4.39 km/s for the EW component and a third from 10.40 to 3.13 for the NS component. Although the initial velocity values are very large, these results support an emerging theory that an earthquake initiates at a super-shear rupture velocity and eventually slows to a "cruising" velocity closer to the shear-wave velocities. These results cannot be compared to previous studies as this analysis is the first one to give direct rupture velocity measurement at the fault scale.

Conclusion

Dense array analysis when applied to strong motion earthquake signals allows the evolution of a fault rupture to be imaged directly. The MUSIC method, used in this study to carry out dense array analysis, was chosen for its ability to resolve seismic signals with low signal-to-noise ratios. The algorithm has been carefully programmed, and implemented with sub-routines to improve the resolution of the covariance matrix which contains the source information.

An innovative way to determine optimal time windows that contain a single signal is introduced in this study. Neither the scalogram nor the spectrogram can be used efficiently for array analysis. Both techniques are visually attractive and efficient for single station analysis, but they require a significant amount of time to define common time windows for multiple station arrays. Therefore an alternative technique is used in this study. The chosen method of time analysis is the "QEE" (Schissele, 2002), "Quantitée d'Energie Expliquée" (Quantity of explainable energy). The advantage of this method is that one can search for the optimal time window using all the recordings at once. The method is based on rebuilding the signals using parameters extracted from the MUSIC frequency wavenumber analysis. The QEE method has been applied satisfactorily to determine optimal time windows for the SMART-1 case study.

The design of a dense array network combines the requirements for an optimal array configuration and the search for an optimal array location. An optimal location is one that takes into account both field constraints, as well as fault size and location. A conclusion drawn by this study about the optimal array configuration is that any proposed array geometry that is imposed by the topography can be improved by increasing the number of instruments, as well as by varying the instrument spacing and array aperture. Nevertheless, in the end, the optimal location and configuration are the ones that fit within the field constraints.

Important lessons have been learnt in applying dense array analysis to both synthetic and real datasets. Firstly a compromise needs to be found between locating the array close enough to the fault in order to get good signal resolution, and locating the array far enough away to record P waves clear from the S wave arrivals for as long as possible. In the application to the synthetic data, by choosing a location 25 km away from the hypocenter fault sources are finely resolved, but the analysis of the P waves is limited to the first 3 seconds of the recordings. Secondly one should always plan for more stations than the number required to

run the array optimally. Although the SMART-1 array was composed of 37 stations, only 27 provided data good enough to be used in this study. Consequently one should always plan for more instruments than the optimal number. In conclusion on site investigation, a thorough study of all potential sites, on the field and using synthetics is essential before deciding on a permanent array site.

The application of dense array analysis to synthetic strong motion data has proven that the technique is efficient in studying fault rupture parameters. The analysis provides rupture velocities and directions consistent with input values. This is an important outcome in validating dense array analysis performed on real data sets. Being able to compare computed parameters with their known input values has emphasized the importance of the velocity model in the projection of the slowness spectra, the importance of timing accuracy and high data sampling of the recording, as well as the importance of the array location from the hypocenter. The significance of timing has a consequence on the choice of instruments to compose the array. Instruments with a high sampling rate are essential. For example, in chapter 3 when the sampling rate was increased from 50 Hz to 500Hz, a much improved seismogram alignment was possible. This study has not been able to analyze the horizontal data set due to the lack of consistent seismogram alignments. Therefore, dense array instruments should provide excellent 3-component recordings. Unexpectedly, dense array analysis of the rupture scenario with an asperity revealed no sign of the asperity. This comes as a surprise considering the promising results dense array analysis had provided previously in other respects. An explanation for this could be high noise and complexity in the recordings, or the signal of the asperity being weaker than the main rupture front signal. Future studies using a range of synthetic programs with various asperity models would be required to fully test the method.

Analyses of the three components of the Event 5 SMART1 data show that the overall rupture trend of the sources is upward from East to West. These results are in agreement with the majority of previous studies. Analysis of the hypocentral depth suggests three depths of 15.5 km, 24 and 27.5 km. These results are supported by the Harvard Moment tensor Catalogue and by Goldstein et al. (1991). This study concludes that the event depth is most likely between 15.5 and 27.5 km. The proposed rupture area is therefore approximately 24 km by 30 km. This result is in agreement with the expected fault length of 10 to 30 km for a magnitude 6 earthquake. Rupture velocities obtained from the three component analysis are

consistent. The extreme initial value of velocity ranges from 10.40 km/s for the NS component analysis to 15.02 km/s for the vertical component analysis. All show a rapid decrease in velocity following the initial rupture. The velocity drops to half its initial value for the vertical component analysis; and a quarter and third respectively for the EW and NS component analyses. Although the initial velocity values are very large, these results support an emerging theory (Xia et al., 2004) that an earthquake initiates at a super-shear rupture velocity and eventually slows to a "cruising" velocity closer to the shear-wave velocities. These results cannot be compared to previous studies as this analysis is the first one to give direct rupture velocity measurements at the fault scale.

Overall, dense array analysis has proven to be very satisfactory and worthy of further study. The method has been validated by synthetic analysis. Direct measurements of rupture parameters from the SMART-1 array provided consistent results for the fault rupture area, rupture direction and rupture velocity. Values of velocities support a variable fault rupture mechanism, with the source initiating at a super-shear velocity and then propagating at velocities closer to shear wave velocities.

Future work on various rupture models are necessary in order to validate and discuss the efficiency of the method in imaging variable rupture velocities, asperities, and rupture geometries. Further studies to establish a final optimal location for an Alpine Fault array are needed. Potential search areas suggested by this study would be ones further away from the fault than Pylon Gully. Given that instruments are becoming increasingly affordable, and that the performance of the array improves with additional stations, this study advises that a potential site should be able to accommodate more than the 12 instruments as originally planned.

Dense array analysis allows one to measure directly fault rupture parameters without any assumption on the fault rupture model. It is a powerful tool in seismology and should be employed further in future fault rupture studies. Future applications of direct rupture measurements would help constraining fault rupture models for inversion and supporting micro-scale laboratory tests.

References

Abrahamson, N. A., B. A. Bolt 1985. The spatial variation of the phasing of seismic strong ground motion. *BSSA*, Vol. 75, No. 5, 1247 – 1264.

Aki, K., and P.G. Richards 1980. Quantitative seismology Theory and Methods, *W.H. Freeman and Company, San Francisco.*

Anderson, H. J., D. Eberhart-Phillips, T. McEvilly, R. Uhrhammer, F. T. Wu 1997. Southern Alps Passive Seismic Experiment. *New Zealand, Institute of Geological & Nuclear Sciences, Dunedin, New Zealand (NZL).* Institute of Geological & Nuclear Sciences Science Report, Report: 97/21, 20 pp., 1997.

Ansell R., and J. Taber 1996. Caught in the crunch: earthquakes and volcanoes in New Zealand. *HarperCollins Publishers*, New Zealand.

Bolt, B. A., C. H. Loh, J. Penzien, Y. B. Tsai and Y. T. Yeh 1982. Preliminary report on the SMART-1 strong motion array in Taiwan. *EERC Report No UCB/EERC-82/13, 1982a.*

Bouchon, M. 1981. A simple method to calculate Green's functions for elastic layered media. *BSSA*, 71, 959-971.

Chouet B., P. Dawson, G. De Luca, M. Martini, G. Milana, G. Saccorotti and R. Scarpa 1998. Array analyses of seismic wavefields radiated by eruptive activity at Stromboli volcano, Italy. *CNR-Gruppo nazionale per la vulcanologia*, Italy.

H.P. Crotwell, T. J. Owens, and j. Ritsema, 1999. The TauP Toolkit: Flexible travel time and ray path utilities, Seismological research letters, 70, 2, 154-160.

Darragh, R. B. 1987. Analysis of near-source waves: separation of wave types using strong motion array recordings, *Ph.D. Dissertation,* University of California, Berkeley.

Eberhart-Phillips, D. 1995. Examination of seismicity in the central Alpine Fault Region, South Island, New Zealand. *New Zealand Journal of Geology and Geophyics* 38: 571–578.

Geli, L., P. Y. Bard, B. Jullien 1988. The effect of topography on earthquake ground motion; a review and new results. *BSSA*, vol.78, no.1, 42-63.

Goldstein, P. 1988. Array measurements of earthquake rupture, *Ph.D. thesis*, University of California, Santa Barbara.

Goldstein, P. and R. J. Archuleta 1991a. Deterministic frequency-wavenumber methods and direct measurements of rupture propagation during earthquakes using a dense array: data analysis. Journal *of Geophysical Research, B, Solid Earth and Planets* 96(4): 6187-6198.

Goldstein, P. and R. J. Archuleta 1991b. Deterministic frequency-wavenumber methods and direct measurements of rupture propagation during earthquakes using a dense array: theory and methods. *Journal of Geophysical Research, B, Solid Earth and Planets* 96(4): 6173-6185.

Hagen, R. A., F. K. Duennebier, and V. Hsu 1988. A seismic refraction study of the crustal structure in the active seismic zone east of Taiwan. *J. Geophys. Res.*, 93, 4785-4796.

Hutchings, L. J. 1987. Modelling strong earthquake ground motion with empirical Green's function, *Ph.D. thesis,* Department of Geological Sciences, State University of New York, Binghamton.

Hutchings, L. and F. Wu 1990. Empirical Green's functions from small earthquakes and waveform study of locally recorded aftershocks of the San Fernando earthquake, *J. Geophys. Res.* 95, 1187-1214.

Hutchings, L. 2002. Program NetMoment, a Simultaneous Inversion for Moment, Source Corner Frequency, and Site Specific t*. *Lawrence Livermore National Laboratory, UCRL-ID 135693.*

Lay T. and T. C. Wallace 1995. Modern Global Seismology. *Academic Press, San Diego, CA, USA.*

Long D. T., S. C. Cox, S. Bannister, M. C. Gerstenberger and D. Okaya 2003. Upper crustal structure beneath the eastern Southern Alps and the Mackenzie Basin, New Zealand, derived from seismic reflection data. *New Zealand Journal of Geology and Geophysics*, 2003, vol. 46, 21:39.

Olivieri, M. and G. Ekström 1999. Rupture Depths and Source Processes of the 1997-1998 Earthquake Sequence in Central Italy. *BSSA* 89(1): 305 – 310.

Roecker, S. W., Y. H. Yeh, and Y. B. Tsai 1987. Three dimensional P and S wave velocity structures beneath Taiwan: Deep structures beneath an arc-continent collision. *J. Geophys. Res.*, 92, 10, 547-10, 570.

Schissele, E. 2002. Analyse et caractérisation des phases sismiques régionales enregistrées par des antennes de capteurs, *Ph.D. Thesis,* Universite de Nice-Sophia-Antipolis.

Schmidt, R.O. 1981. A signal subspace approach to multiple emitter location and spectral estimation. *Ph.D. Dissertation* , Stanford University, Stanford, California.

Schmidt , R.O. 1986. Multiple emitter location and signal parameter estimation, *IEEE Trans. on Antennas and Propagations*, 34, 276-280.

Sekiguchi, H. and T. Iwata 2002. Rupture Process of the 1999 Kocaeli, Turkey, Earthquake Estimated from Strong-Motion Waveforms. *BSSA,* 92(1): 300 – 311.

Wells D. and K. Coppersmith 1994. New Empirical Relationships among Magnitude, Rupture Length, Rupture Width, Rupture Area, and Surface Displacement. *BSSA* 84: 974 – 1002.

Wen, K. L., and Y. T. Yeh 1984. Seismic velocity structure beneath the SMART 1 array, *bulletin of the institute of earth sciences, academia sinica,* 4 , 51-72.

Xia K., Rosakis A. J., Kanamori H. 2004. Laboratory earthquakes: The sub-rayleigh-to-supershear rupture transition. *Science*, vol. 303, no. 5665, 1859-1861.

Yetton, M. D. 2000. The probability and consequences of the next Alpine fault earthquake, South Island, New Zealand, *Ph.D. thesis, Department of Geological Sciences,* University of Canterbury, New Zealand.

Zeng C. and Chau-Huei 2001. Fault Rupture Process of the 20 September 1999 Chi-Chi, Taiwan Earthquake. *BSSA,* 91(5): 1088 – 1098.

Zobin, V. and V. Levina 2001. The Rupture Process of the Mw 7.8 Cape Kronotsky, Kamchatka Earthquake of 5 December 1997 and Its Relationship to Foreshocks and Aftershocks. *BSSA,* 91(6): 1619 - 1628.